Image quality optimization and radiation dose minimization in bone X-ray radiography

TP Keetile

Orcid.org 0000-0003-0756-0951

Mini-dissertation submitted in partial fulfilment of the requirements for the degree *Master of Science in Applied Radiation Science* at North-West University

Supervisor: Prof VM Tshivhase
Co-supervisor: Mr Robert Bellarmin Nshimirimana

Examination: July 2019

Student number: 24587117

Declaration

I herein declare that this mini-dissertation “Image quality optimization and radiation dose minimization in bone X-ray radiography” is the demonstration of my own original research work and it has never been submitted for any degree at any university before. I further declare that contributions from other sources are evidently acknowledged by the indicated references.

Name & Surname : Tsholofelo Patrick Keetile

Signature: …… ……

Date : …17 July 2019……

Acknowledgements

Firstly, I would like to thank God the almighty for providing me with strength and patience, without his kindness the completion of this work would not have been possible.

I would like to express my overflowing gratitude to the following people, my co-supervisor, Mr. Robert Bellarmin Nshimirimana from department of Radiation Science at Necsa (South African Nuclear Energy Corporation) for his selfless support and outstanding mentorship through guidance and assistance throughout this research study. My supervisor, Prof Victor Makondelele Tshivhase and Mr Thulani Dlamini from the Center of Applied Radiation Science and Technology (CARST) at North West University (NWU) Mafikeng Campus, their insightful suggestions and valuable guidance are highly appreciated. I would also like to acknowledge the assistance from Mr Lunga Bam and Mr Jakobus Hoffman at Necsa. The moral support from my colleagues at CARST is also highly appreciated.

My appreciation also goes to my mother, Cecilia Keetile, my mother's cousin, Gontle Metswi, my grandmother, Boihang Keetile, my cousin, Dipogiso Serapelwane and my two siblings, Dineo and Letlhogonolo Keetile for their undivided moral support, patience and motivation throughout this research study. Lastly, I would also like to extend my hand of appreciation to, NWU Mafikeng Campus and Ithemba labs for financial support, CARST for providing me with the platform to explore and develop an interest for radiation sciences. The department of Radiation Science at Necsa for providing me with the conducive learning platform and necessary materials to conduct this research study.

Abstract

In this study, the goal was to optimize image quality and minimize radiation dose in bone X-ray radiography procedure. Investigations were conducted to determine optimum quality images of the dedicated phantoms and samples at minimized radiation dose. In this regard, the main problem of this study was to find X-ray scanning parameters (voltage, current, exposure time, focal-sample distance (FSD) and X-ray filters) that give the high quality images with minimal radiation dose. The first investigation involved the establishment of the relationship of each X-ray scanning parameter with image quality indicators and the measure radiation dose independently. This relationship was established by varying each parameter during the acquisition of images and radiation dose measurements. Micro-focus X-ray machine and identifier ultra were used for acquisition of images and radiation dose monitoring respectively. ImageJ software was used to evaluate the data sets from the acquired images of the rat samples and phantoms. These data sets were further used to calculate different image quality indicators for investigation of each X-ray parameter. A multi-objective optimization problem was realised, in a sense that a conflict between different image quality indicators and radiation dose existed. In the second investigation of this study, the weight sum technique was applied in the analysis of the variation of X-ray scanning parameters in relation to image quality indicators and radiation dose. The purpose of this technique was to convert multi-objective optimization problem between image quality indicators and radiation dose into a single-objective optimization problem of the main objectives, namely image quality objective and radiation dose objective. For each X-ray scanning parameter, the final presentation of the results was included in the figures, in which the plot of the two main objectives versus the variation of each parameter and the plot of the objectives against each other were presented. The best compromise between the two objectives was searched and found in these figures. The most optimal image quality and minimized radiation dose occurred with 0.1 mm of copper (Cu) X-ray filter with X-ray tube voltage of 100 kV, X-ray current of 100μA, X-ray exposure time of 1 sec and FSD of 65 cm.

Table of Contents

List of Figures

List of Tables

List of Abbreviations and Symbols

2D	Two dimension
ALARA	As low as reasonably achievable
AP	Anterior-posterior
CBCT	Cone beam computed tomography
CR	Computed radiography
DNA	Deoxyribose nucleic acid
DRL	Diagnostic reference levels
FOV	Field of view
FSD	Focal-sample distance
ICRP	International Commission of Radiological Protection
J/Kg	Joules per kilogram
LAT	Lateral anterior posterior
MOOP	Multi-objective optimization problem
Necsa	South African Nuclear Energy Corporation
PA	Posterior-Anterior
RSNA	Radiological Society of North America
SOOR	Single-objective optimization problem
Sv	Sievert

Chapter 1: Introduction

1.1. Background

The X-ray radiation is defined as electromagnetic radiation capable of passing through the object and reveals the interior structure of that object in the form of an image. This type of radiation was discovered by the German scientist Wilhelm Rontgen (Carl & Gudrun Alm, 1996). Rontgen was studying the pathway of electric current passing through an evacuated glass tube in 1895 at the university of Wurzburg when he made this phenomenal discovery, he validated his discovery by taking the X-ray image of his wife's hand which evidently displayed the bones of her hand (Chougule, 2005; Carl & Gudrun Alm, 1996). Nowadays, X-ray radiation is extensively used in medical and industrial applications primarily due to its ability to penetrate dense materials such as bones and reveal their actual anatomy as discovered by Rontgen in 1895 (Chougule, 2005).

The X-ray radiation is transmitted through the patient during medical diagnosis. X-ray radiography is one of the common imaging techniques that employ X-ray radiation to reveal the internal structures of the objects (RSNA, 2010). X-ray radiography in medical application allows the provision of diagnostic information that assist in the treatment of patient's medical condition (Umadevi & Geethalakshmi, 2011). The abnormalities or diseases such as tooth decay, lung cancer, cervical cancer, kidney stones, blood clots and cardiac diseases are usually diagnosed through common X-ray examinations such as dental X-ray examination, pelvis X-ray examination, chest X-ray examination and abdominal X-ray examination (RSNA, 2010).

The importance of acquiring high quality images in medical imaging is a necessity to enable ultimate accurate diagnosis; however acquisition of high quality images in medical imaging is associated with high radiation exposures (Bacher, 2006). The X-ray radiation is mainly characterized as ionizing radiation due to its ability to ionize atoms; ionizing radiation is generally known to be hazardous in nature to the human body (Desouky, et al., 2015). The high radiation dose because of high radiation exposures is commonly associated with induction of negative biological effects inside the body (Bushberg, et al., 2002). The X-ray photons passing through the human body undergoes absorption inside the cell tissues (Bushberg, et al., 2002).

Subsequently, the ionization of biological molecules takes place; the alteration of molecules inside the body occurs and accordingly makes damages to the cells (Ullman, 1977).

The concept of optimization in X-ray radiography examinations is the process of finding the best compromise between the quality of the radiograph and radiation dose for the particular X-ray examination (Nyathi, 2012). The objective of optimization in X-ray radiography is to enhance the desired benefits of this imaging technique without compromising the well-being of the patients (Nyathi, 2012). The strategies of optimization are often implemented in X-ray radiography as a tool to ensure that negligible radiation exposures are maintained during examinations (Uffmann & Schaefer-Prokop, 2009). The reduction of radiation exposures to patients in X-ray examinations is a difficult process because the purpose of examination itself is often the deciding factor between the amounts of radiation exposure required to produce a certain level of image quality (Uffmann & Schaefer-Prokop, 2009). Optimization is necessary for reduction of radiation doses and to ensure that sufficient information is attained at an ideal quality of the image in a certain X-ray examinations for a specified medical or industrial purpose (Uffmann & Schaefer-Prokop, 2009).

1.2. Problem statement and motivation

Naturally, human beings consist of a certain number of bones at birth although some of these bones are reduced into joints as they develop; consequently a grown human being ends up with a reduced amount of 206 separate bones (Umadevi & Geethalakshmi, 2011). The human bones are structurally suited to provide support, protection of organs, making of blood cells, storage of minerals and assist in maintaining the shape of the body (Umadevi & Geethalakshmi, 2011). Therefore, to ensure a balanced life it is important for bones to be in proper state at all times (RSNA, 2010). Unfortunately, arthritis, bone fractures, osteoporosis, bone cancer and many other bone defects are some of the implications that are of hindrance in the proper functioning of bones (RSNA, 2010).

The X-ray radiography is one of the techniques employed to detect the defects and fractures in bones (Hendee & Ritenour, 2002; Dendy & Heaton, 1999). However the use of X-ray

radiography in the diagnosis and treatment of bone defects has a potential health risk to the patient (Dendy & Heaton, 1999). Ideally, it is meaningless to use X-ray radiography to obtain the image of a certain defective bone if the surrounding soft tissues will receive high levels of radiation dose (Hendee & Ritenour, 2002). The edge of obtaining benefits over harm through regulated radiation source should be prioritized (ICRP, 2007). The radiation doses to patients should be as low as reasonably achievable (ALARA) during radiography scan, while the sufficient image quality is acquired to enable precise diagnosis (ICRP 93, 2001). Other benefits of X-ray radiography technique in medical diagnosis is the undivided provision of non-destructive acquisition of any bone image in the body such as hand, wrist, arm, elbow, shoulder and other structural bones (Hendee & Ritenour, 2002).

According to the system of radiation protection postulated by International Commission on Radiological Protection (ICRP) in 2007, optimization is amongst the principles of radiation protection and it states that exposure of radiation to people and their radiation dose levels should be kept as low as reasonably achievable (ALARA). In a nutshell it is very relevant and feasible to maintain and conclude that optimization is a very delicate aspect in X-ray radiography examinations (ICRP, 2007). Generally, the benefits of X-ray radiography in the medical application should outweigh the health hazards associated with radiation exposures (ICRP, 2007). It remains the concern of the experimentalists within the scientific community to strategize on how to minimize the radiation exposure during the optimization of the quality of X-ray radiographic imaging (Dendy & Heaton, 1999). To achieve optimization of image quality, optimum balance between X-ray tube voltage, X-ray tube current, exposure time, source detector distance and added filtration must be thoroughly understood in correlation with harmful effects inflicted into the patient's body during the X-ray examination (Dendy & Heaton, 1999).

To that end, this study sought to explore the optimization of the quality of the image obtained from a bone X-ray radiography procedure with minimized radiation dose deposition in the surrounding soft tissue. The effect of X-ray scanning parameters was established and thereafter optimization was explored. The concerns of safety and quality of acquisition of X-ray radiography were addressed in this study; the establishment of the X-ray scanning parameters

that yield the best quality image at minimized radiation dose were achieved and presented in this regard. In addition, these X-ray scanning parameters will assist the operators to acquire the high quality images without impinging on the well-being of the patient. The study also advances the insightful knowledge of the use of phantoms and real samples to explore means of optimizing the X-ray radiographs and the associated radiation dose.

1.3. Research aim and objectives

1.3.1. Aim

The aim of this study was to investigate the means of optimizing the quality of the image obtained from a bone radiography procedure with minimized radiation dose deposition in the surrounding soft tissue.

1.3.2. Objectives

The objectives of this study were to:

- determine the effect of varying the X-ray tube parameters (voltage, current and exposure time) on bone radiography and radiation exposure with constant focal-sample distance (FSD),
- determine the effect of varying the FSD on bone radiography and radiation exposure with constant X-ray tube voltage, X-ray tube current and exposure time,
- investigate the effect of varying different types of filter thicknesses on bone radiography and radiation exposure with constant X-ray tube voltage, X-ray tube current, exposure time and source detector distance and
- determine the best possible combinations of tube potential, tube current, exposure time, added filtration and FSD that can yield best possible image quality at minimized radiation dose deposition into the surrounding soft tissue.

Chapter 2: Literature review

2.1.Optimization of X-ray radiography

The concept of optimization is elementary to the daily human activities; since the demand to make life easier and better with accessible resources is central to human survival (Parkinson et al., 2013). Optimization techniques are generally employed to advance or modify systems to function more efficiently (Abimbola, 2013). The engineered systems are not always functioning satisfactorily to meet human needs and wants, optimum systems that produce best quality results are aspired instead (Abimbola, 2013). The optimization is the process of determining the capability of a system to produce best quality possible results or benefits for a specified purpose (Parkinson et al., 2013).

The process of quantifying best quality benefits out of X-ray radiography systems is influenced by concerns of safety and protection of patients and the need to acquire high quality images that will enable efficient and accurate diagnosis (Abimbola, 2013), the conflict thereof arises from two objectives, namely image quality and X-ray radiation dose (Bacher, 2006). The maximum of image quality during X-ray radiography is desirable and this normally results in high radiation dose that could impact negatively in the health of the patient (Bacher, 2006). The optimization of image quality through minimization of radiation dose absorption is a multi-objective optimization problem, and these sorts of problems are commonly encountered in the research field of economics, scientific, engineering and other research fields (Abimbola, 2013). Contrary to single-objective optimization problem (SOOPs), the multi-objective optimization problems (MOOPs) consists two or more objective functions that are in conflict with each other (Garret, 2007). These objective functions need to be solved concurrently where a solution that perfectly suit one objective function could be worse off for another objective function (Garret, 2007).

The concern of the optimization of the multi-objective problem is the vector minimization of the objective functions $f(x)$ $(\text{Bacher}, 2006)$. These objectives functions are treated with constraints $G(x)$. The equations (2.1) to (2.3) describe such vector minimization of the objective functions $f(x)$ mathematically (Bacher, 2006),

$$f(x) = [f_1(x), \dots, \dots f_n(x)] \quad (2.1)$$

$$G_i(x) = 0, \;\; i = (1, \dots, m) \quad (2.2)$$

$$x_l \leq x \leq x_u \quad (2.3)$$

where the number of optimized objective functions is denoted by m and n is the dimensional search space. An x vector solution is Pareto optimal if all other vectors consist of a value greater than atleast one of the objective function i or it has the value equal for all objectives (Bacher, 2006). A curve of Pareto points indicates the compromise between objectives (Bacher, 2006).

2.1.1. Multi objective optimization problem

The search of the solution of multi-objective optimization problem (MOOP) entails some techniques to form a scalar objective (Garret, 2007). The weighted sum technique is classified as *priori* method (Farah, 2016). In *priori* method, the decision maker specifies the preferred information about the problem (Garret, 2007), the best solution that suits the requirements of the decision maker is established thereafter (Jakob & Blume, 2014). Other *priori* techniques are the dictionary ordering method, ε-constraint method, analytic hierarchy method, objective programming method etc (Farah, 2016). The weighted sum is one of the methods of assessment that sums the multi-objective optimization problem into a single objective optimization problem that can be solved by optimization algorithms (Jakob & Blume, 2014).

The weighted sum method also involves the summation of all weighted objective functions, which are the weight factors multiplied by objective function (Jakob & Blume, 2014). A weighting factor has to be selected for each objective (Jakob & Blume, 2014). The objective functions are typically normalized because they consist of a variety of scales (Farah, 2016). The normalization of objectives functions is normally realized when minimizing and maximizing the objectives according to equation (2.5) and (2.6) below.

$$f_i^{norm} = \frac{f_{i_{max}} - f_i}{f_{i_{max}} - f_{i_{min}}} \quad (2.5)$$

$$f_i^{norm} = 1 - \frac{f_{i_{max}} - f_i}{f_{i_{max}} - f_{i_{min}}} \quad (2.6)$$

The equation (2.5) and equation (2.6) are the minimization and maximization of objectives (Jakob & Blume, 2014). The equation (2.7) is for the calculation of the weighted sum

$$\text{Maximize} \sum_{i=1}^{k} w_i f_i^{norm} \text{ (a)} \quad (2.7)$$

where vector of design variables is a , $w_i(i = 1, \dots \dots k)$ is a weighting factor for the ith objective function and k is the number of objective functions (Timothy & Jasbir, 2009; Weck & Kim, 2004). The weighted sum is a convex combination of objectives if $\sum_{i=1}^{k} w_i = 1$ and $0 \leq w_i \geq 1$ (Timothy & Jasbir, 2009). Any point of a convex Pareto front are obtained through variation of the suitable weight factors (Timothy & Jasbir, 2009).

During the optimization process the Pareto optimal solutions or the non-dominated solutions are established, this is achieved by shifting the line of the selected weights factor to become tangent to the perimeter of the objective function's feasible region (Jakob & Blume, 2014). In case of a non-convex problem, the traditional weighted sum method cannot find solutions on the Pareto front although they are Pareto optimal solutions or non-dominated optimum solutions; this is the downside of the traditional weighted sum method (Jakob & Blume, 2014). The weighted sum technique is applied to a convex combination of objectives, in which the sum of all weights is constant and negative weights are not allowed (Hirotaka, 2005; Jakob & Blume, 2014). The adaptive weighted sum technique is the advanced form of the traditional weighted sum (Jakob & Blume, 2014).

2.2.The harmful effects of ionizing radiation

The alterations in the structure of the cells inside the body of the patient are likely to occur during the interaction of X-ray photons with the human tissue (Mayles et al., 2007). The changes that occur as a result of radiation absorption at cellular level can inhibit cellular processes; subsequently division of cells might be negatively affected such as irregular excess division of cells which might lead to the induction of malignant tumours (Mayles et al., 2007). The body organs are exposed to some level of radiation exposure during X-ray examinations, depending on the intensity of radiation deposition some cells may experience no damage at all, while other cells might be able to recover from the damage induced and continue to function normally or abnormally (Desouky et al., 2015).

2.2.1.The alterations that occurs inside the tissue cells

The radiation interactions with cells stimulate cellular or biological changes in any of the two actions referred to as direct or indirect action (Desouky et al., 2015). The direct action takes place when X-ray photon directly changes the internal structures of the cells by ionizing or exciting macromolecules inside the cell (Mayles et al., 2007; Desouky et al., 2015). The structural change in the components of the cells may lead to complete cell damage or cell death; injured cells that survive are more likely to induce cancer at a later stage (Mayles et al., 2007).

The indirect action occurs when an X-ray photon interact with water molecules inside the cell (Desouky et al., 2015). The substances known as free radicals and ions are produced as chemical bonds are broken by X-ray photons in water molecules (William & Ritenour, 2002), the number of free radicals produced by ionizing radiation depends on the total radiation dose received (Desouky et al., 2015). An ion is a charged atom or molecule; normally a molecule or an atom becomes negatively charged or positively charged because of gaining or losing electrons (Desouky et al., 2015). The free radicals are molecules or atoms that consist of one unpaired electron in the outer shell (Desouky et al., 2015). The presence of single unpaired electron in the outer shell makes the atoms highly reactive (Dumela, 2010). The production of H_2O^+ ion occurs during the reaction between water molecule (H_2O) and radiation (equation

2.8) (Dumela, 2010), X-ray photon transfer all of its energy to the water molecule (H_2O) during the reaction (Bushberg et al., 2002; Whaites, 2002).

$$H_2O + \text{energy} \rightarrow H_2O^+ + e^- \quad (2.8)$$

The positively charged water molecule (H_2O^+) consists of an unpaired electron in an outer orbital shell (Bushberg et al., 2002). Inside the cell, the H_2O^+ ion radical will dissociate and the electron (e^-) will continue to react with other water molecules to produce hydroxyl radical ($OH\bullet$) and negatively charged water molecule (H_2O^-) (Whaites, 2002), as indicated in equation (2.8) and (2.9). Negatively charged water molecule will further dissociates to form hydrogen ion (H^+) and hydroxyl radical ($OH\bullet$), stated in equation (2.11).

$$\mathbf{H_2O^+ \rightarrow H^+ + OH\bullet} \quad (2.9)$$

$$\mathbf{H_2O + e^- \rightarrow H_2O^-} \quad (2.10)$$

$$\mathbf{H_2O^- \rightarrow H^+ + OH\bullet} \quad (2.11)$$

$$\mathbf{OH\bullet + OH\bullet \rightarrow H_2O_2}\ \text{(hydrogen peroxide)(toxic)} \quad (2.12)$$

Hydroxyl radical ($OH\bullet$) is highly reactive and will react with other free radicals to form hydrogen peroxide (H_2O_2) as indicated in equation (2.12), hydrogen peroxide is a highly poisonous compound to the cell (Bushberg et al., 2002; Dendy & Heaton, 1999; Whaites, 2002). Hydrogen peroxide breaks down the molecular structure of Deoxyribose nucleic acid (DNA) inside the cell and this could result in the inability of the cell to function or the complete cell death (Dendy & Heaton, 1999). Most of cell damages caused by radiation are caused by indirect action mechanism because body cells consist of 70% water molecules (Desouky et al., 2015). The genetic defects such as mutations are likely to occur due to the DNA damage induced by radiation, genetic information is carried within DNA macromolecules inside the

cell and this implies that any damage or alteration to any cell in the body is damage to genetic material (Dendy & Heaton, 1999).

2.2.2.The stochastic and deterministic effects of radiation

The effects of radiation were classified into two categories: deterministic effects and stochastic effects (Dendy & Heaton, 1999). The deterministic effect is a cause and effect relationship between radiation exposure and certain side effects such as sterility, hair loss, cataract, and skin erythema (Andiscoa et al., 2014). The deterministic effects normally occur at high radiation exposures. These effects were based on a number of cell destruction or the whole organ inactivity, the severity of deterministic effects increases with an increasing radiation dose (Desouky et al., 2015; ICRP 93, 2001). The deterministic effects were characterized by a threshold dose, below the threshold dose there is no clinical effect (harm) (Dendy & Heaton, 1999).

The stochastic effects occur by chance and are mostly associated with cancer induction; the severity of this effect also increases with radiation dose (Dendy & Heaton, 1999). Stochastic effects are not characterized by threshold dose, these effects occur randomly irrespective of the extent of radiation dose (Andiscoa et al., 2014). The stochastic effects of radiation exposure do not always occur instantly, some cells recover from damages by changing altogether but continue to regenerate and fulfil their suited function (Andiscoa et al., 2014). The negative biological effect may only become superficial after years of radiation exposure probably more evident on the descendants of the patient (Andiscoa et al., 2014). A typical example of stochastic effect includes heritable genetic effects, malignant tumours and leukaemia (Dendy & Heaton, 1999).

2.2.3.Protection of patients against harmful effects of X-ray radiation

Protection of patients against the harmful effects of radiation during X-ray examinations is the priority in diagnostic radiology (Chougule, 2005). The avoidance of radiation exposures that induces negative biological effects is central to the radiation protection (ICRP, 2007). International commission of radiation protection (ICRP) suggested general principles of radiation protection as; justification, optimization and dose limit (ICRP, 2007). The three

principles of radiation protection were established to ensure protection and safety of human beings against occupational exposures, public exposures and medical exposures (ICRP, 2007).

The justification principle states that the proper usage of regulated X-ray radiation in medical diagnosis is only accepted if it does more good than harm to the patient (ICRP 93, 2001). The goal of optimization principle in X-ray examinations is to adjust the protection measures in such a way that net benefit to the patient is maximized while maintaining radiation doses as low as reasonably achievable (ICRP, 2007; ICRP 93, 2001). There are no specific dose limits for patients undergoing X-ray examinations and optimization principle is set by ICRP as the crucial mechanism to control patient protection against the harmful effects of radiation (Vano et al., 2002). The limitations of radiation dose could be counterproductive to the definite purpose of the medical procedure (Kyung-Hyun, 2016). The necessity of optimization principle is to ensure that during diagnostic procedure sufficient diagnostic information is attained while implementing a strategy that sustains the ALARA principle (Chougule, 2005).

2.2.4.Diagnostic reference levels

It is a good practice to establish diagnostic reference levels both nationally and regionally because equipment and diagnostic examination protocols are different across X-ray imaging facilities in different countries (Vano et al., 2002; ICRP, 2007). The diagnostic reference levels (DRLs) as shown in Table 1 below are used as a tool for optimization of protection of patients during diagnostic medical radiation exposures (Vano et al., 2002). It is the responsibility of relevant health bodies to establish diagnostic reference values in hospitals. The diagnostic reference level (DRL) is a measure of patient radiation dose that will serve as a guide to optimize patient protection in diagnostic examination (Vano et al., 2002). The values in Table 1 do not indicate the borderline between good and poor medical practise, rather they assist in investigations to identify radiologic facilities where unusual levels of radiation doses are encountered (Vano et al., 2002).

Table 1: Diagnostic reference values for X-ray examinations (Vano et al., 2002).

Type of diagnostic examination	**Entrance surface dose (mGy)**
Chest (PA)	0.4
Chest (LAT)	1.5
Thoracic spine (AP)	7
Thoracic spine (LAT)	20
Lumbar spine (AP)	10
Lumbar spine (LAT)	30
Skull (PA)	5
Skull (LAT)	3
Abdomen (AP)	10
Pelvis (AP)	10
Dental (Peripheral)	7
Dental (AP)	5

2.3. Image quality versus radiation dose in X-ray radiography

Image quality is the degree of visual representation of the diagnostic information produced through an imaging system (Sprawls, 1994). The term quality is a composite of several factors that determines the degree of visibility of the objects in a given digital image for a particular purpose (Sprawls, 1994). Digital images were made up of well-ordered array of picture elements known as pixels (Kristopher, 2013). Dimensions of pixel array verifies the size and shape (typically, rectangular shape) of an image. The image breadth and height are the number of columns and rows in the array (Kristopher, 2013).

High quality images are desired during bone X-ray examination to enable accurate and reliable diagnosis, they also assist in the identification of aberrations by establishing a database for physiology and anatomy (RSNA, 2010).

2.3.1. Image quality

The clear visibility of information on the radiographic image is based on the optimum balance of the combination of measureable quantities that quantifies image quality (Kristopher, 2013). The variation of the objective indicators of image quality revolves around the analysis of the pixel arrangement in the digital image. Image quality is primarily quantified by at least four factors, namely contrast, unsharpness, resolution and noise. These factors were discussed below (Sprawls, 1994).

2.3.2. Image quality indicators

2.3.2.1. Contrast

In simple terms, contrast refers to the dissimilarity or difference, in the context of the radiograph this concept refers to the variation of brightness and darkness of the scanned object and its background (Sprawls, 1985). The projected object for a particular image can appear in the form of different shades normally as grey shade, bright or dark shade as quantified by the quantity of the pixels involved (Whaites, 2002). The object that absorbs more X-ray photons is likely to appear bright in the image due to the small number of signal that was captured by the pixels during the formation of the image in the detector (Whaites & Cawson, 2002).

High contrast values allows the clear distinction of different structures projected in the image. Contrast ratio, also known as Root Mean Square (RMS) contrast is the ratio of highest pixel number in the first region of interest to the lowest pixel number in the second region of interest in the image (Denis & Pelli, 2013).The expression for contrast ratio (CR) is indicated in equation (2.13) below.

$$\mathrm{CR} = \left(\frac{\text{Highest pixel number}_{\text{First region of interest}}}{\text{Lowest pixel number}_{\text{Second region of interest}}} \right) \tag{2.13}$$

2.3.2.2. Noise

The identification of objects in a radiograph might still be a tricky subject even if optimum levels of contrast, sharpness and resolution are attained (Uffmann & Schaefer-Prokop, 2009). Noise, which is the random distribution of the signal in the detector, is another factor that quantifies the quality of the image. Noise is a concept that refers to the optical density fluctuations in the values of pixels across an image (Uffmann & Schaefer-Prokop, 2009). High noise levels obscure the information content on the radiograph (Dance, et al., 2012).

The study of Marijike & Yves. (2013) comprehends the signal to noise ratio (SNR) as the indicative factor that compares the extend of desired signal in the image to the level of background noise. This factor is expressed as a quotient of mean pixel value $\bar{X}$ and the standard deviation σ^2 of a certain region in the digital image as indicated in equation (2.14) (Yves & Marijke, 2013). The high values of signal to noise ratio (SNR) are desirable in the image as they indicate that noise is insignicant and does not obscure the visibility of the projected information (Yves & Marijke, 2013).

$$\mathrm{SNR} = \left(\frac{\overline{\mathrm{X}}}{\sigma^2}\right) \tag{2.14}$$

On the other hand, another image indicator, contrast to noise ratio (CNR) quantifies the image quality based on contrast rather than transmitted photon's signal (Hess & Neitzel, 2012). The calculation of contrast to noise ratio value is based on mean and standard deviation of pixel numbers within the two regions of interest in the digital image, namely, the region where the desired information is projected and the region besides it (Hess & Neitzel, 2012). The equation (2.15) below illustrate the expression of contrast to noise ratio, where x_1 and x_2 are the mean pixel values and σ_1 and σ_2 are the standard deviations of the first region of interest and second region of interest respectively (Hess & Neitzel, 2012).

$$\mathrm{CNR} = \frac{\overline{x_1} - \overline{x_2}}{\sqrt{\frac{1}{2}(\sigma_1)^2 + (\sigma_2)^2}} \quad (2.15)$$

2.3.2.3. Unsharpness

The nature of objects or features varies according to their size. Objects inside the human body vary from large organs and bones to small structural features (Akmal & Zhonghua, 2013). The small details of the objects play a very vital role in the formation of the radiographic image (Akmal & Zhonghua, 2013). The different imaging techniques has a limit of how far they can go imaging the tiniest object, therefore the visibility of these details in the final image is affected or restricted (Bushberg et al., 2002). The apparent restriction of the visibility of certain details is achieved by initiation of blurriness or unsharpness by the imaging technique as its ability to process the tiny objects is exhausted to some extent (Akmal & Zhonghua, 2013). The unsharpness of the image reduces spatial resolution (Sprawls, 1994). The different types of image unsharpness exist in three forms as, motion/movement unsharpness, system unsharpness and geometric unsharpness (Sprawls, 1994).

A radiographic image that clearly portrays details differentiation and distinct boundaries was often described as being sharp (Bacher, 2006). High contrast and sharpness are desired to make it possible to distinguish different features as separate entities in the image (Sprawls, 1985). The resolution of the imaging system systematically quantifies the unsharpness of the digital image,this features is adjusted to allow perfect dinstiction of different objects in the image,resolution of the image is thoughrouly described below (Bacher, 2006).

The resolution of the imaging system is the ability to distinguish structures that are close to one another, imaging system resolves the closely related structures to be observed as separate objects in the radiograph (Hendee & Ritenour, 2002). The considerable amount of blurriness

sets in, as objects are resolved, eventually objects blur jointly until they can no longer appear as separate features on the radiograph (Bushberg et al., 2002).

2.3.2.4. Resolution

The capability of an imaging system to separate two closely related objects as different entities is known as resolution (Dance et al., 2012). The resolution is affected by several factors including focal spot size, pixel size, patient motion and the distance between the patient and the detector (Olubamiji, 2011). The quantification of spatial resolution of an imaging system involves several techniques such as computing full width at half maximum (FWHM) of the point spread function (PPF), line spread function (LPF), edge spread function (ESF) and modulation transfer function (MTF) (Dance et al., 2012). Other forms of resolution quantification technique includes the measurement of line pairs per mm (i.e. the determination of the highest bar frequency in line pairs per millimetre(mm) that can be visualized by the system determined in a bar pattern image) (Dance et al., 2012). High resolution is usually encountered at high number of line pairs (Olubamiji, 2011).

The most commonly used method to evaluate resolution is modulation transfer function (Olubamiji, 2011). Modulation transfer function is usually used as a deciding factor for comparing different imaging systems and to evaluate the imaging performance of systems at any spatial frequency (Olubamiji, 2011). Illustration of the transmitted X-ray beam through the sample was normally achieved through frequency and amplitude of sine waves (Hendee & Ritenour, 2002). The size of amplitude and frequency relies on the transmitted X-ray photons of which the transmitted X-ray photons are modulated by the sample. The shape of the sine wave represents information carried in the beam about the internal structure of the sample (Hendee & Ritenour, 2002).

The modulation transfer function is a calculation of the size of the sine wave that will participate in the formation of the image (Hendee & Ritenour, 2002). Modulation transfer function is usually expressed as the quotient of the amplitudes of the spatial frequency at the output and the input of the imaging system (Michael et al., 2004). The modulation transfer

function is a graphical indicator of unsharpness or contrast resolution of an imaging system as depicted in Figure 1 below (Michael et al., 2004).

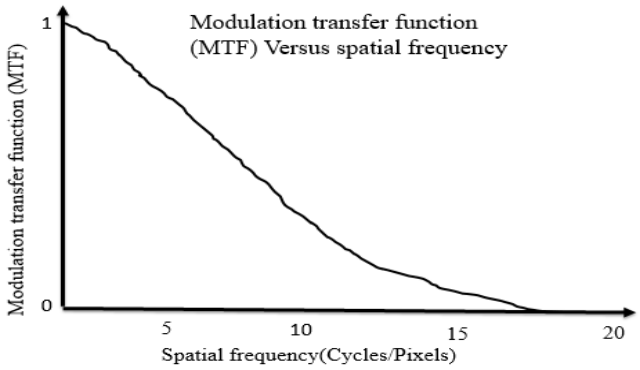

Figure 1: Graphical illustration of modulation transfer function.

The modulation transfer function for an imaging system was quantified from point spread function or line spread function of the imaged sample (Dendy & Heaton, 1999). The value of modulation transfer function normally varies from zero to one, this is indicated in Figure 1 (Dendy & Heaton, 1999). Modulation transfer function is unity for spatial resolution at low spatial frequency, however, the value of modulation transfers function decreases to zero as the frequency increases as shown in Figure 1 (Dendy & Heaton, 1999). No information can be observed on the image at zero modulation transfer function (Mayles et al., 2007).

2.3.3. Radiation dosimetry

The X-ray radiation transfers energy to matter when interacting with it, there variation for energy transferred is quantified by the quality and quantity of the beam (David, et al., 2009). The biological risks that are associated with the energy of the radiation transferred are based on the type of radiation and the type of matter exposed (Dendy & Heaton, 1999). The basic radiation quantities and absorbed dose quantities from Hendee & Ritenour. (2002) were discussed below.

2.3.3.1. X-ray fluence and flux

The X-ray fluence is the quantity of photons (N) passing through the specific area (A) of the medium (Hendee & Ritenour, 2002). The X-ray fluence (∅) is given as:

$$\emptyset = \frac{N}{A} \quad (2.16)$$

The X-ray fluence $(\emptyset)$ unit is cm^{-2} (Hendee & Ritenour, 2002). The rate at which the X-ray fluence is passing through the medium is known as the X-ray flux (ϕ) (Hendee & Ritenour, 2002), this quantity is actually the fluence rate as expressed in equation (2.17) below.

$$\phi = \frac{N}{At} \quad (2.17)$$

Where the unit of X-ray flux (ϕ) is cm^{-2}/s (Hendee & Ritenour, 2002). The energy fluence (φ) is the quantity that defines monoenergetic X-ray beam, if the energy of each X-ray in the beam is known; the fluence $(\emptyset)$ is multiplied by the energy (E) of each photon to get the energy fluence (φ) as indicated in equation (2.18).

$$\varphi = \frac{NE}{A} \quad (2.18)$$

The unit of energy fluence (φ) is $kV.cm^{-2}$ (Hendee & Ritenour, 2002). The product of X-ray flux (ϕ) and energy (E) is known as the energy flux (Ψ), equation (2.19) is the expression for the energy flux (Ψ).

$$\Psi = \frac{NE}{At} \quad (2.19)$$

The unit of energy flux (Ψ) is $kV.cm^{-2}/s$ (Hendee & Ritenour, 2002).

2.3.3.2.Absorbed dose

The amount of energy deposited by ionizing radiation in the specific unit of tissue mass is known as absorbed dose, whereas radiation exposure is basically the quantity of charges produced as results of air ionization by X-ray radiation (Ladia et al., 2016). The unit of absorbed dose D is joule per kilogram (J/kg) as defined in equation (2.20) below.

$$D = \frac{\Delta \epsilon}{\Delta m} \quad (2.20)$$

Where $\Delta\epsilon$ is the mean energy transferred by ionizing radiation to a unit of tissue mass Δm.

The SI unit of J/kg is Gray (Gy), 1 Gy is equivalent to 1 J/kg. However, the traditional unit of absorbed radiation dose is rad, rad is related to Gy as 1 rad equals 0.01 Gy of which 0.01Gy indicate that 0.01 Joules of energy has been deposited into a kilogram of tissue (Andiscoa et al., 2014).

2.3.3.3.Estimation of radiation dose

Indirect method of detecting or estimating radiation dose to patient in an X-ray examination is made possible by measuring the quantities that are linked to radiation such as dose area product (DAP) (Gupta et al., 2013). The most reliable and convenient radiation quantity that is commonly used for the indirect method of measuring patient dose is DAP (Gupta et al., 2013). DAP is the product of radiation dose in air (kerma) within the X-ray beam and the beam area, this quantity offers a fine detection of total X-ray beam energy delivered to a patient during an X-ray examination (Gupta et al., 2013). DAP measuring devices are normally attached to the within the radiography machines to measure the DAP for each X-ray examination (Ruiz et al., 2000).

DAP meter is usually characterized as a large area ionization chamber that is fixed into the collimator of the X-ray source (Gupta et al., 2013). The X-ray beam produced by the X-ray tube intercept the DAP meter as it passes through it (Ruiz et al., 2000). The measurements of this meter are given as the product of kerma (kinetic energy released per unit mass) and the irradiated area in unit $Gy.cm^2$ (Gupta et al., 2013). DAP readings can be measured anywhere in the beam and they do not depend on the distance between the source and the patient because the area of the beam or its divergence increases with the distance from the point source (Gupta et al., 2013).

Furthermore, the DAP readings can be used to estimate the initial dose, which is the radiation beam energy before interaction with the patient occurs and the transmitted dose, which is the radiation beam energy that has transversed through the patient. The DAP values can also be used to calculate entrance surface dose (ESD) (Begum, 2001). ESD is one of the basic radiation dose quantities for measuring the patient dose (Begum, 2001). This radiation dose quantity is also used as the basic quantity of comparing the International Reference Values, which is important for optimization of patient radiation dose (Begum, 2001). The equation (2.21) can be used for calculating ESD.

$$\boldsymbol{ESD = \left(\frac{DAP}{area}\right).f.BSF} \tag{2.21}$$

Tissue irradiated region is noted as area with unit cm^2, the ratio of the mass absorption coefficients of muscle and air is indicated by f and backscatter factor is denoted by BSF in equation (2.21) (Ruiz et al., 2000).

2.3.3.4.Equivalent dose

Unlike equivalent dose and effective dose, absorbed dose tells us the effect of radiation in specific tissues (Andiscoa et al., 2014). The equivalent dose is used to evaluate the side effects of the absorbed dose according to the biological damage incurred and this quantity justifies the efficiency of the type of radiation to cause a biological damage (RSNA, 2018). Different types of radiation vary in terms of the biological damage that they can induce in a certain organ (Ladia et al., 2016). Radiation types with high linear energy transfer (LET) will induce more damage than those with low LET because they will deposit most of their energy at a short path length within the organ or tissue (Andiscoa et al., 2014). Different types of radiation have been allocated the radiation weighting factors, these factors are interrelated with the relative biological effectiveness (RBE) which is related to LET of radiation (RSNA, 2018). Equivalent dose (H_T) normally incorporate radiation weighting factors (w_R) to quantify the effect of a certain type of radiation (Ladia et al., 2016), equation (2.22) is used to calculate this quantity, which is basically the type of radiation(R) and its quantity (radiation dose($D_{T,R}$)) that is absorbed by a certain organ(T).

$$H_T = \sum_R w_R D_{T,R} \quad (2.22)$$

The equivalent dose is expressed in Sievert (Sv) (Ladia et al., 2016). Table 2 shows the radiation weighing factors and their different energies.

Table 2: Radiation weighting factors and their energies for different types of radiation (Harbison & Martin, 2006).

Types of radiation and energy range	Radiation weighting factors
Positrons, electrons, photons and muons: all energies	1
Neutrons: < 10 KeV 10 KeV $-$ 100 KeV > 100 KeV $-$ 2 MeV > 2 MeV $-$ 20 MeV > 20 MeV	5 10 20 10 5
Protons : > 2 MeV	5
Fission fragments, heavy nuclei, alpha particles	20

2.3.3.5.Effective dose

Effective dose, which is another radiation quantity, is used to evaluate the side effects of absorbed dose that might be incurred in the future (Andiscoa et al., 2014). This quantity incorporates the following factors relative to the human organs: the organs' radiation sensitivity and the absorbed dose as well as the intensity of radiation (RSNA, 2018). The sensitivity of different body organs to radiation is different, therefore this phenomenon is taken into consideration when evaluating equivalent dose (Andiscoa et al., 2014). Thus, the effective dose (E) may be explained as the total weighted equivalent doses (H_T) to various body organs, this equivalent doses are weighted by tissue weighted factors (w_T) per an organ (T) (Dlamini, 2014), the tissue weighted factors are indicated in Table 3.

Table 3: Illustration of tissue weighting factors (ICRP, 2007; Harbison & Martin, 2006).

Organ or tissue	Weighting factors
Compact bone and skin	0.01
Stomach, lung, red marrow and colon	0.12
Thyroid	0.01
Gonads	0.20
Liver,oesophogus,bladder and breast	0.05

The equation (2.23) is used to calculate the weighted effective dose,

$$E = \sum_T w_T H_T \qquad (2.23)$$

which may be further expanded to:

$$E = \sum_T w_T \sum_R w_R D_{T,R} \qquad (2.24)$$

this quantity has the same units as equivalent dose, the traditional unit is rem and the SI unit is Sievert (Sv) (Ladia et al., 2016). All types of radiation used in diagnostic medicine are less hazardous; therefore, even though the units of absorbed dose and equivalent dose are different, these two dose quantities are the same numerically (RSNA, 2018). The equivalent dose and effective dose are usually expressed in mSv which is equivalent to mGy , similar to mGy, mSv expresses a joule of energy per kilogram of tissue (RSNA, 2018) .

2.3.4. Image quality and radiation dose optimization

The thorough understanding of the effect of X-ray imaging exposure parameters is vital in a mission of optimizing the quality of the radiograph with minimized radiation exposure. The variation of the combination of X-ray tube current, X-ray tube potential and added filtration that regulates the quality and quantity of the X-ray radiation produced has an ultimate effect on image quality (Hess & Neitzel, 2012).

A considerable amount of literature emerged from the concept of image quality optimization through the minimization of radiation dose absorption in X-ray radiography. The concerns of safety of patients and acquisition of high quality radiographs during X-ray examinations motivated the scientific community to investigate different techniques of optimization of X-ray radiographic imaging. Most of these investigations were based on the exploration of the understanding and establishing the effect of X-ray tube parameters on image quality and radiation dose. The diversity of techniques of quantifying the radiation dose measurement and image quality evaluation for the optimization process were established in this regard. The usage of materials that simulates the absorption properties of the real body human parts was a priority to avoid the exposure of human beings to high levels of X-ray radiation. The radiograph acquisitions were made by a variety of digital systems and recording of radiation dose was practised through different mechanisms using softwares and radiation detectors.

2.3.4.1.The brief contents of some of the published papers concerning the exploration of optimization of radiation dosimetry and image quality in X-ray radiography

The study conducted by Hess et al. (2012) was based on the optimization of image quality and patient dose for paediatric extremities. The objective of this study was to investigate the effect of X-ray tube voltage and filtration on image quality and patient dose, this study entailed the use of a phantom which was made up of 1cm thickness of poly methyl methacrylate (PMMA) and 1mm aluminium (Al), metal to simulate soft tissue and bone tissue absorption properties.

In this study the optimization technique used involved the usage of simulation and experimental results (Hess & Neitzel, 2012). The mean pixel values and the radiation dose absorption were measured with and without the filtration of 0.1mm copper / aluminium in the X-ray tube voltage of 40 kV to 66 kV. The contrast to noise ratio (CNR) was measured from the mean pixel values of acquired radiographs using Image software. The mean absorbed dose (MAD) was measured by both experimental and simulation measurements (Hess & Neitzel, 2012). The simulation measurements of radiation dose were simulated by Birch-Marshal model and Monte Carlo-based simulation. The most convenient combination

of image quality and radiation dose was established at the X-ray tube voltage of 40 kV without additional filtration (Hess & Neitzel, 2012).

Zainon et al. (2014) investigated the analysis and optimization of radiation dosimetry and image quality in X-ray radiographic imaging. This study was aimed at understanding the effect of X-ray tube voltage on image quality and radiation dose.

The radiographic chest phantom was imaged using the Toshiba mobile X-ray machine, the X-ray tube voltage was varied from 56kV-100kV. The radiation dose absorption was detected using the ionization chamber placed under the exposure window to get the measurement of absorbed dose. The effect of X-ray tube voltage (KVp) on radiation dose and image quality was explored by applying different X-ray tube voltage values (kVps). The image quality was thereafter optimized by assessing parameters such as filter types such as copper X-ray filter and aluminium X-ray filter as well as their thicknesses and X-ray tube voltage. The analysis of the radiographs was done using the ImageJ software and contrast to noise ratio (CNR) was the adopted image quality indicator for this study. In this study, the contrast to noise ratio (CNR) was found to be higher (good image quality) with low radiation dose absorbed when using 0.2 mm copper thickness at 100 KVp.

The research study of Martin Palomo et al. (2008) on the quantification of the change in radiation dose using different CBCT (Cone beam computed tomography) settings entailed the use of ten thermoluminescent dosimeters; these dosimeters were inserted into different sections into the phantom for the purpose of measuring radiation dose during the exposure.

The phantom that was used in this study is known as Rando phantom. The Rando phantom is made up of the actual human skeleton embedded inside proprietary urethane formulation (Palomo et al., 2008). This phantom is intended to have the same X-ray absorption properties as human tissue at the certain X-ray exposure (Palomo et al., 2008). One exposure setting consisted of two X-ray tube voltage values, four different X-ray tube current (mA) values and three fields of view (FOV) (Palomo et al., 2008). Each X-ray exposure was repeated thrice to reduce uncertainty and establish accuracy (Palomo et al., 2008). The CBCT (Cone

beam computed tomography) outcomes revealed that the general decrease in radiation dose at around 0.62 times was accomplished through the X-ray tube voltage (KVp) minimization between 120 kV-100 kV (Palomo et al., 2008).

A publication on the study of the methodology of radiation dose measurement and image quality evaluation for the analysis in the optimization process of digital radiography was conducted by Tung et al. (2007), similarly to the study of Martin Palomo et al. (2008) this study involved the use of thermoluminescent dosimeters for X-ray radiation absorption monitoring (Tung et al., 2007). In this study, the phantom was made up of 10mm thickness of poly methyl methacrylate (PMMA) material. The phantom consisted of bored holes of different widths and depths. The dosimeters were attached to the surfaces of the poly methyl methacrylate (PMMA) slabs with sticky tape to record the radiation dose during the exposure.

Radiologists evaluated the acquired images by the calculation of IQF (image quality figure). The MATLAB was also used to assess the same images, this computer program allowed parallax corrections. The outcome obtained was that the computer program shown to be sensitive than the radiologists.

2.4. Phantoms used to optimize X-ray radiography.

The patient is often substituted by the phantom when investigating the optimum radiation profile for high image quality acquisition in X-ray radiography (Palomo et al., 2008). The phantom is typically made up of materials that are equivalent to the actual human tissue and bones (David et al., 2009). Material used to make the phantom should have the same properties as the actual human tissues and bones in terms of the thickness, density and the atomic number, these features allows the phantom to scatter and absorbs the X-ray beam energy exactly the same way as the actual patient body (David et al., 2009).

Materials such as polymethylmethacrylate (common name: acrylic glass) and metals are commonly used to simulate the density of the real tissues and bones (Paulo, 2014). These materials are also used in some cases to construct soft tissue organs such as lung, kidneys, abdomen etc., in most cases these materials are used in the phantom studies of the assessment

of image quality and patient radiation dose (Akmal & Zhonghua, 2013). It is important for a tissue and bone simulating material to match the actual body parts properties because the elemental composition of a material affect the way the material behaves under the energy of incident radiation (Paulo, 2014).

2.4.1. Types of phantoms

2.4.1.1. ATOM phantom and RANDO phantom

ATOM anthropomorphic phantoms are made using Computerised Imaging Reference Systems (CIRS) (CIRS, 2017).These type of phantoms includes adult male and female figure with their height, weight and appropriate radiological features as stated in Table 4 (David et al., 2009). The body parts such as torso, head, thigh bone (femur) and genitalia are included in the standard ATOM phantoms (White, 1978). The custom-tailored phantoms are normally made according to manufactures specifications, features such as material simulating bone and soft tissue organs with relevant diagnostic photon energies are always present in a standard phantom (David et al., 2009).

Table 4: Physiological and radiological difference between ATOM and RANDO phantoms (Paulo, 2014).

Physical and radiological features	**RANDO male**	**RANDO female**	**ATOM Phantom male**	**ATOM phantom female**
Height (cm)	163	175	160	173
Weight (kg)	54	73.5	55	73
Tissue's density (gm^{-3})	0.997	0.9897	1.055	1.055
Atomic number of tissue (Z)	7.6	7.6	7.15	7.15
Bone's density (gm^{-3})	-	-	1.6	1.6
Atomic number of the bones	-	-	11.5	11.5

RANDO phantom include air, human cadaver bones or bone simulating material as well as soft and lung tissue equivalent material (Shrimpton et al., 1981). This phantom incorporates the actual human skeleton or bone-simulating material fixed inside the proprietary urethane formulation as indicated in Figure 2. The proprietary urethane formulation created for typical diagnostic energy range is usually used to simulate soft tissue and lung tissue (Paulo, 2014). The effective atomic number and density of proprietary urethane formulation simulates muscle and lung tissue with the stochastic distribution of lipids layer (Shrimpton et al., 1981).

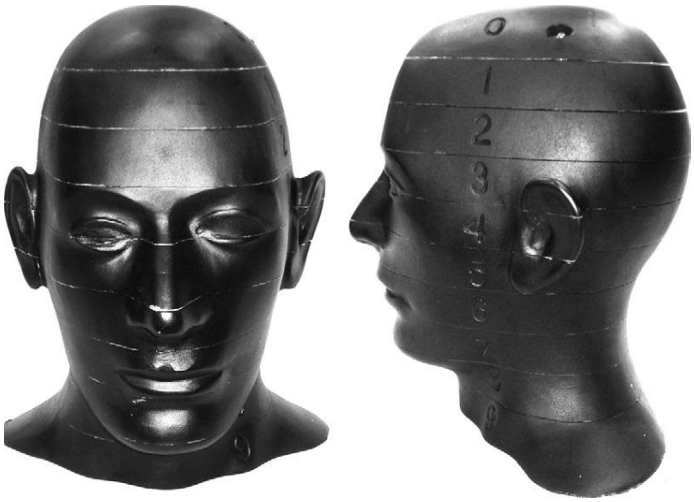

Figure 2: RANDO Phantom made with actual human bones embedded inside tissue simulating material (Palomo et al., 2008).

There are two common types of RANDO phantoms: The RANDO female and the Rando male, both of these phantoms do not have legs and arms (Marshall et al., 1979). The lung simulating tissue of RANDO phantoms were moulded to fit inside the rib cage (Hörnlund & Bernhardsson, 2013). These phantoms were sliced at 2.5cm intervals for the inclusion of radiation detectors (Marshall et al., 1979). Figure 2 shows that the holes were made into the sliced sections for the insertion of thermoluminescence dosimeters (TLDs) for radiation dose measurements (Palomo et al., 2008).

2.5. Radiation dose detection techniques

2.3.5. Direct technique for measuring radiation dose

The direct method of radiation dose measurement were usually achieved by placing detectors at the beam entrance surface on the phantom or the patient's skin (Dumela, 2010). The radiation detectors are attached to the patient's skin or the phantom's surface before the X-ray procedure (Dumela, 2010). The direct technique of measuring radiation dose that an organ is receiving during the X-ray examination was made possible by radiation detectors; a typical example that has been done successfully is the placement of dosimeters in a particular designed suitable phantom (Palomo et al., 2008). The direct method of measuring radiation dose is the most reliable and accurate way of detecting radiation dose delivered to the patient

during the X-ray procedure (Nyathi, 2012). Radiation detectors that are used for direct detection of patient dose are photographic film, thermoluminescence dosimeters and Metal-Oxide Semiconductor Field-Effect Transistor (MOSFET) (Dumela, 2010; Nyathi, 2012).

2.3.5.1. Thermoluminescence dosimetry (TLD)

Thermoluminescence dosimeter is the most reliable radiation detector for measuring radiation dose at the surface of the phantom or the patient's skin (Begum, 2001). Thermoluminescence dosimeters are preferred for radiation dose detection in X-ray examinations because of their advantageous features such their size, they are usually small hence they can be easily wedged on a phantom or a patient without causing any impairment (Bushberg et al., 2002). Thermoluminescence dosimeters exist in a range of materials and different forms such as circular chips, powder, rods and square cubes (Tootell et al., 2014).

Professor Farrington Daniels from the University of Wisconsin-Madison discovered thermoluminescence dosimetry in 1954 (Tootell et al., 2014). Thermoluminescence dosimeters consist of crystals that scintillates when heated after interacting with ionizing radiation interact (Michael et al., 2004). Detection of ionizing radiation exposure by thermoluminescence dosimeters involves measuring the extent of visible light produced by the crystal inside the detector (Tootell et al., 2014). The radiation exposure incident on the detector determines the intensity of light emitted (Hörnlund & Bernhardsson, 2013). Calcium fluoride and lithium fluoride are common types of thermoluminescence dosimeter crystals that glow upon interaction with ionizing radiation (Hörnlund & Bernhardsson, 2013).

The phenomenon of thermoluminescence in crystal lattice is usually described using the two energy bands of the atoms in crystal lattice in Figure 3 (William & Ritenour, 2002). The region between the two energy bands of an atom is referred to as the forbidden gap, electrons are said to be in the metastable state when they are near this region (Bushberg et al., 2002). Figure 3 illustrates that the valence band consist of electrons that are tightly bound in the atom orbitals, this band illustrate the ground state of an atom (William & Ritenour, 2002). The conduction band is the second state of an atom where electrons move freely within the crystal lattice as shown in Figure 3. The electron traps in Figure 3 within the forbidden gap

are created by the presence of the impurities (Mg, Ti, Cu, and P) in the crystal lattice (Bushberg et al., 2002). The electrons in the valence band are moved towards the conduction band when the crystal is exposed to ionizing radiation, this leads to the creation of vacant spaces within the electron orbitals in the valence band (William & Ritenour, 2002), this is demonstrated in Figure 3 below. The excited electrons will move within the crystal lattice until they can move back to refill the vacant spaces in the valence band or if fall into the metastable state (Gupta et al., 2013; Bushberg et al., 2002).

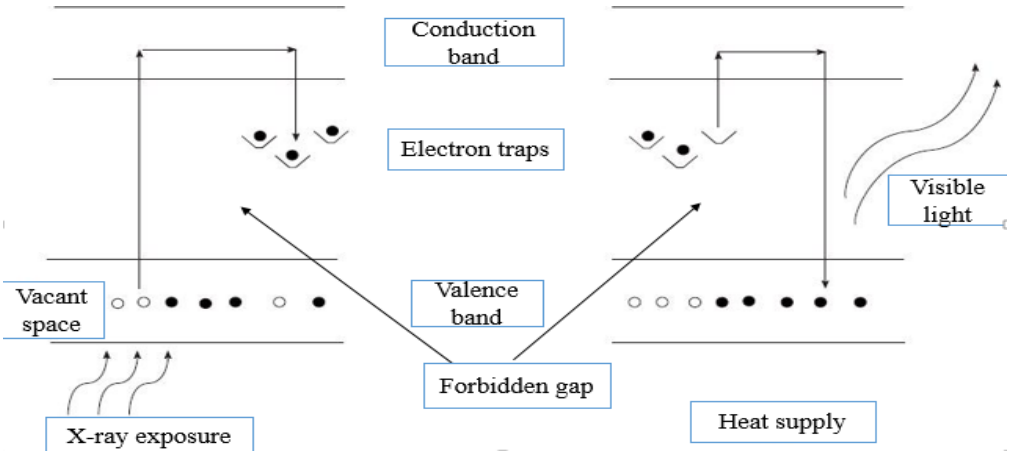

Figure 3: Illustration of the process of thermoluminescence in crystal lattice (Akmal & Zhonghua, 2013).

The electrons in the metastable state require energy to move to the conduction band before they move to their respective orbitals in the valence band (William & Ritenour, 2002). Heat energy is supplied to move electrons towards the conduction band from the metastable state and on their way back to the valence band; they lose energy (Tootell et al., 2014). The energy lost by electrons in this transition is emitted as visible light as shown in Figure 3; this process is commonly known as thermoluminescence (Faiz, 2003). The photomultiplier tube is used to harvest this light and convert it to an electronic signal that can be further processed into an apparent readout reading (Akmal & Zhonghua, 2013).

2.3.6. Indirect technique for measuring radiation dose

Indirect method of detecting or estimating radiation dose to patient in an X-ray examination were made possible by measuring the quantities that are linked to radiation such as fluoroscopy time or dose area product (DAP) (Dendy & Heaton, 1999). The most reliable and convenient radiation quantity that were used for the indirect method of measuring patient dose is dose area product (Dendy & Heaton, 1999). Dose area product is the product of radiation dose in air (kerma) within the X-ray beam and the beam area, this quantity offers a fine detection of total X-ray beam energy delivered to a patient during an X-ray examination (Bacher, 2006). DAP measuring devices can be attached to radiography machines to measure the DAP for each X-ray examination, this technique is the most practical approach for monitoring the radiation dose received by the patients (Dendy & Heaton, 1999).

DAP meter is usually characterized as a large area ionization chamber that is fixed into the collimator of the X-ray source (Gupta et al., 2013). The X-ray beam produced by the X-ray tube intercept the DAP meter as it passes through it (Gupta et al., 2013). The measurements of this meter are given as the product of kerma and the irradiated area in unit $\mathrm{Gy.cm^2}$. DAP readings can be measured anywhere in the beam and they do not depend on the distance between the source and the patient because the area of the beam or its divergence increases with the distance from the point source (Gupta et al., 2013).

The dose area product values can be used to calculate Entrance surface dose (ESD) (Gupta et al., 2013). Entrance Surface Dose is one of the basic radiation dose quantities for measuring the patient dose (Begum, 2001). This radiation dose quantity is also used as the basic quantity of comparing the International Reference Values, which is important for optimization of patient radiation dose (Begum, 2001). The equation (2.25) for calculating entrance surface dose (ESD) is given below.

$$\mathrm{ESD} = \left(\frac{\mathrm{DAP}}{\mathrm{area}}\right).\mathrm{f}.\mathrm{BSF} \tag{2.25}$$

Tissue irradiated region is noted as area with unit cm^2, the ratio of the mass absorption coefficients of muscle and air is indicated as f and backscatter factor is denoted by BSF in equation (2.25) (Ruiz et al., 2000).

2.3.6.1. Gas filled detectors

The gas filled detectors are actually gas (air) ionization chambers that are mounted just after the collimator in the imaging system (Bushberg et al., 2002) .The gas filled detectors exist in three forms namely gas ion chambers, gas flow proportional counters, and Geiger-Muller detectors (McGraw-Hill Concise Encyclopedia of Physics , 2000). These detectors measure the energy of the beam striking the patient and causes insignificant attenuation of the X-ray beam (Bushberg et al., 2002).

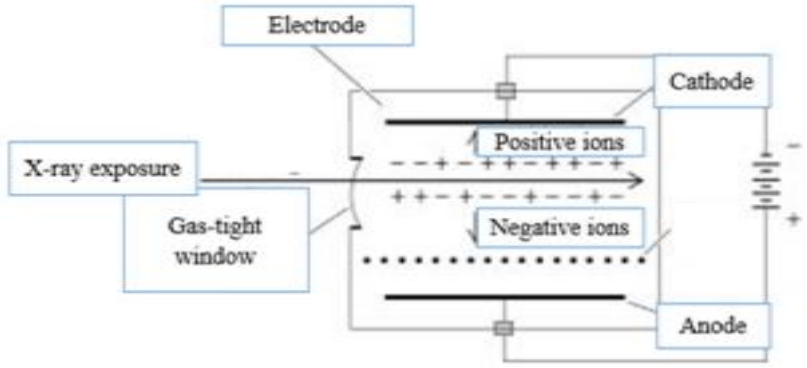

Figure 4: Illustration of the gas filled detector (McGraw-Hill Concise Encyclopedia of Physics , 2000).

The ionizing radiation enters through the gas-tight window and creates ion pairs in the gas medium inside the ionization detector as shown in Figure 4 (Ernest et al., 2014). The ion pairs will be collected by electrodes placed in the opposite sides within the medium (Gupta et al., 2013). Figure 4 shows that the application of the voltage across the electrodes will separate ion pairs. The positive ion will migrate towards the cathode and the negatively charged ion will move towards the anode (Ernest et al., 2014). The voltage between the electrodes increased until all ion pairs are collected at the electrodes (Ernest et al., 2014). The presence of ions in the electrode will induce the flow of electrical current or voltage pulses, this electric

signal was presented on a digital read-out (McGraw-Hill Concise Encyclopedia of Physics , 2000).

2.6. Principle of X-ray imaging

2.6.1.Production of X-rays

The X-ray beam is produced by the X-ray tube. The X-ray tube converts electrical energy into two different forms of energies known as X-ray radiation and heat (Hendee & Ritenour, 2002). The X-ray tube as illustrated on Figure 5 below is characterized by two components known as the anode (positive electrical charge) and the cathode (negative electrical charge) to which the filament is attached (Hendee & Ritenour, 2002). The two critical terminals of the X-ray tube (cathode and anode) are encapsulated inside the vacuum to facilitate the prevention of air molecules to collide with electrons accelerated between the filament and target anode spot (Ervin & Podgorsak, 2005). Figure 5 shows that the filament is a spiral tungsten wire, high current (mA) is applied to the cathode to heat the filament in order to loosen the electrons (Dendy & Heaton, 1999).The anode is the targeted tungsten metal, tungsten is used in an X-ray tube because of the following characteristics (Bacher, 2006).

- Stable emission of electrons at high temperatures
- High atomic number (74) which allows high heat conductivity, high melting point and the efficient production of X-ray photons from orbiting electrons.
- Tungsten metal has desirable mechanical properties and it can be drawn into fine filament for cathode assembly.
- A high heat conductivity
- A low vapour pressure.

The loose electrons on the filament are accelerated across the vacuum from the cathode towards the anode through the applied voltage (kV) across the tube as shown in Figure 5 below (Hendee & Ritenour, 2002). The regions where collisions between electrons and atoms of the anode will take place is known as the focal spot (Hendee & Ritenour, 2002). The energy released upon the collision of incident electrons with the anode metal target atoms in the focal

spot. Small focal spot reduce the image blurring and increase the visibility of the projected details (Dance et al., 2012). The 99% of the incident electron's kinetic energies will be converted into heat and 1% of energy will be in the form of X-rays (Dendy & Heaton, 1999).

The high voltage (kV) of the X-ray tube, which is also known as the accelerating voltage, increases the kinetic energy of the electrons which has the ultimate increase in the number of high energy X-rays produced on the anode metal target (Dendy & Heaton, 1999). The heating state of the anode due to multiple collisions with electrons is known to reduce the efficiency or the life-time of the X-ray tube (Michael et al., 2004). Figure 5 shows that water is allowed to flow in and out of the anode for cooling purpose, this is done to prevent melting; however, heat dissipation through rotating anode disk is employed in some instances instead of water cooling (Hendee & Ritenour, 2002).

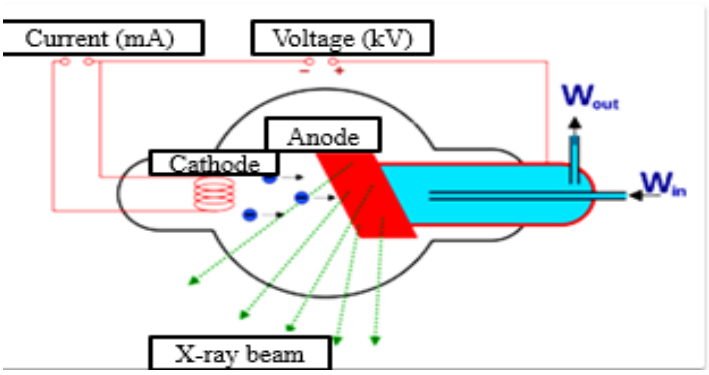

Figure 5: Illustration of X-ray tube (Milch, 2008).

2.6.1.1. Bremsstrahlung and Characteristics X-rays

Bremsstrahlung and Characteristics X-rays are two types of processes that take place because of collision between the electrons and anode metal target (Ervin & Podgorsak, 2005). The X-ray spectrum produced consists of about 80 % of Bremsstrahlung X-rays and 20% of Characteristic X-rays (Tooley, 2002), these processes occur in the following manner:

- Bremsstrahlung X-ray production

The columbic attraction forces occur between the incident electron and positive charge due to the presence of protons in the nucleus (Bacher, 2006). The incident electron in Figure 6

gets into the atom as it gets accelerated with the inner electron shells of the atom; the speed at which the incident electron was travelling is now reduced as this electron is now travelling in a path (Milch, 2008). The kinetic energy difference between the incident electron and the deflected electron is released as Bremsstrahlung X-ray (David et al., 2009) as indicated in Figure 6.

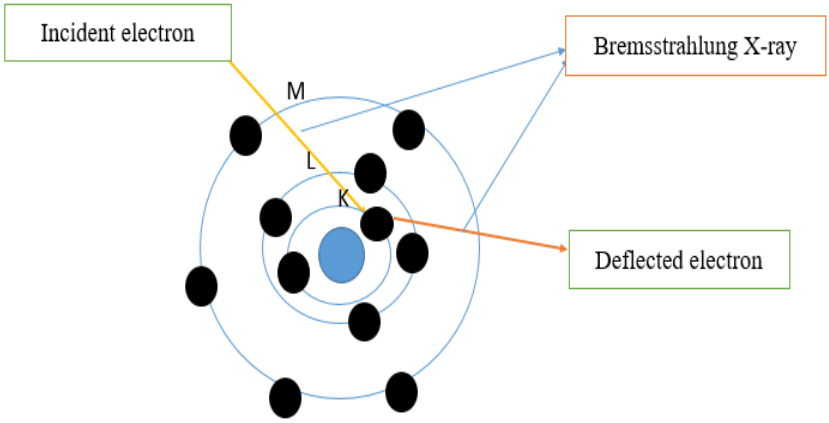

Figure 6: Illustration of bremsstrahlung X-ray production.

- Characteristic X-ray production

In Figure 7, the incident electron collides with inner shell electron inside the atom and both of these electrons are ejected from the atom (Milch, 2008). A vacancy is left in the inner atomic shell (K) and this triggers an outer electron shell (M) to migrate and fill the vacant space (Bacher, 2006). The most dominating photons in characteristic X-rays arise from K-shell vacancies, which were filled by electrons from the L and M shells (Bacher, 2006). Figure 7 below shows that the binding energy difference between the ejected inner shell

electron and the migrating outer shell electron is emitted as characteristic X-ray (David et al., 2009).

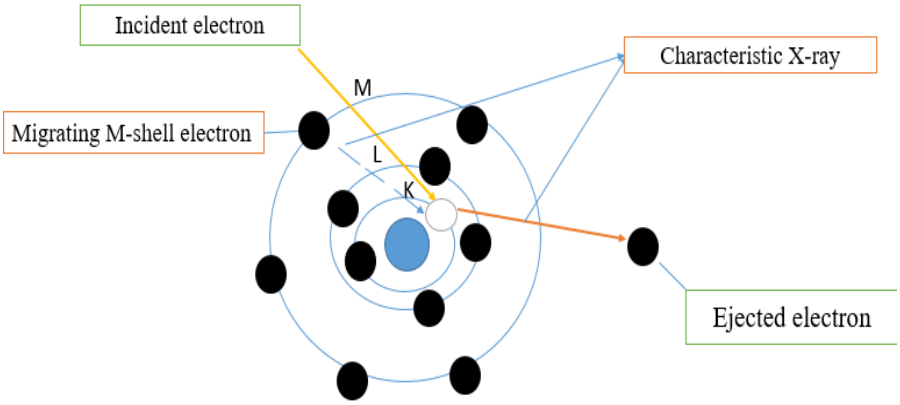

Figure 7: Illustration of characteristic X-ray production.

2.6.1.2. X-ray spectrum

The quality and quantity of the X-ray beam quantifies the penetrating ability of the X-ray beam produced by the X-ray tube (Bushberg et al., 2002). The accelerating X-ray tube voltage determines the kinetic energy of an electron incident on the anode (Gupta et al., 2013). The number of electrons emanated from the cathode is dependent on the heating current (mA) applied on the filament. The electrons accelerated towards the anode quantify the quantity of X-ray photons carried with the beam (Whaites, 2002).

The variation of the intensity of the X-ray beam with energies of photons is known as the X-ray spectrum, which is, illustrated (Hendee & Ritenour, 2002). The spectrum in Figure 8 consists of bremsstrahlung and discrete characteristics X-rays (Whaites, 2002). The X-ray beam produced through bremsstrahlung process has continuous broad line energy spectrum, this is clearly shown in Figure 8 below (Hendee & Ritenour, 2002). The continuous line of bremsstrahlung X-ray photons consist of energies ranging from zero to energies equivalent to kinetic energies of electrons hitting the anode (Mayles et al., 2007). The characteristic X-ray photons are also produced along with bremsstrahlung X-ray photons (Hendee & Ritenour, 2002). The characteristic X-ray photons consist of discrete lines at a fixed energy in the spectrum as indicated in Figure 8 below (The energy of Characteristic x-ray is discrete as indicated at 69 keV) (Hendee & Ritenour, 2002). The fixed energy of the photons is

quantified by the difference between the binding energies of the electron orbitals of the anode (Radiology Key, 2016). The Kilovoltage (KV) of the X-ray tube quantifies the quality of the photons and the maximum energy (KeV) of the spectrum (Dance et al., 2012).

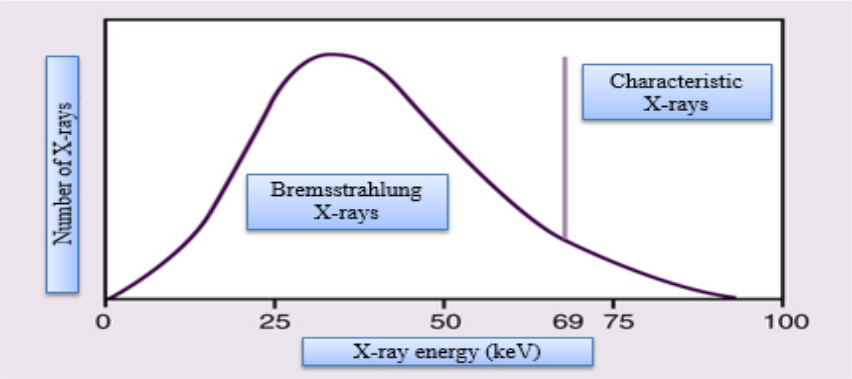

Figure 8: Bremsstrahlung and Characteristic X-ray spectrum (Radiology Key, 2016).

2.6.1.3. Factors affecting the quality and quantity of photons in X-ray spectrum

The X-ray spectrum is controlled by varying the X-ray tube parameters settings mainly the current, exposure timer and Kilovoltage (KVp) (Hendee & Ritenour, 2002). Factors such as X-ray filtration and the distance between the X-ray source and the sample (Newton's Inverse square law of radiation) are known to modify the intensity of the X-ray photons in a spectrum (Ervin & Podgorsak, 2005). These factors are important in X-ray examinations as they play a vital role in image quality and radiation exposure (Hendee & Ritenour, 2002). The discussion of factors that affect X-ray beam quality and quantity is in depth below.

The exposure time (s) of the X-ray tube controls the duration of the exposure of the number of photons generated (Bacher, 2006). The exposure time is directly proportional to the number of X-ray photons in the spectrum; however, adjustment of the exposure time does not have any significant impact on the energy of the X-ray spectrum (Bacher, 2006). The quantity of X-ray photons produced are expressed as the product of time and tube current(mA) (Hendee & Ritenour, 2002).

A. X-ray tube current (mA)

The extent of current produced is controlled by the mA selector connected to the cathode assembly (William & Ritenour, 2002). The increase in the mA setting provides more heating to the filament results in emanation of more electrons that collide with the target metal to produce radiation (Ervin & Podgorsak, 2005). The intensity (I) of the X-ray photons within the beam is directly proportional to the X-ray tube current (mA) (Carl & Gudrun Alm, 1996), an increase in the X-ray beam current results in the quantity of the X-ray beam as indicated in equation (2.26) (Hendee & Ritenour, 2002).

$$I \propto (mA) \tag{2.26}$$

B. Voltage

Voltage (kV) of the X-ray tube is directly proportional to the energy of the electrons travelling from the cathode towards the anode (Bushberg et al., 2002). High kV determines the efficiency of conversion of electron energy into X-ray photons, thus high Kilovoltage quantifies the quantity, quality and the mean energy of photons produced (RSNA, 2010). The intensity of the photons in an X-ray spectrum is related to the Kilovoltage (kV) as indicated by equation (2.27) below (RSNA, 2010).

$$I \propto (kV)^2 \tag{2.27}$$

C. Added filtration

The X-ray spectrum consists of polyenergetic photons (Whaites & Cawson, 2002). Unlike the low energy photons (Hendee & Ritenour, 2002), X-ray photons with sufficient energy are important in radiography examinations because they undergo penetration through anatomic structures and reach the image detector (Ervin & Podgorsak, 2005). The low energy X-ray photons removed in an X-ray beam before any interaction could take place, these photons end up being completely absorbed by objects within the sample and as a result, they do not

participate in image formation in the detector (RSNA, 2010). The complete absorption of X-ray photons inside the body contributes to an increase in radiation dose deposition (Dance et al., 2012).

Metal filters such as aluminium, copper etc. are added in the X-ray beam pathway to remove low energy photons while contributing negligible effect on the higher energy photons (David et al., 2009). The absence of low energy photons in an X-ray spectrum is known to increase the penetrating ability of the X-ray beam (Ladia et al., 2016). The total filtration of a particular X-ray imaging system is the sum of the inherent filtration and added filtration (Hendee & Ritenour, 2002), inherent filtration arises from components of the tube that the X-ray beam counteracts with after being formed from the focal spot on the anode target (William & Ritenour, 2002).

D. Newton's Inverse square law of radiation

The X-ray beam that passes through the sample from the X-ray source is not only attenuated by matter (David et al., 2009). The inverse squared law of radiation states that the radiation intensity passing through the precise area of the object/sample decreases as the square of the distance of that object's area from the X-ray source increases (Whaites & Cawson, 2002). The energy of radiation emitted from a certain point diverges from the source as the distance from the source increases (David et al., 2009). This could have an impact on radiation dose absorption and image quality depending on the positioning of the patient during the X-ray examination (Whaites & Cawson, 2002).

2.6.2. X-ray interaction with tissues and bones

The X-ray photons interacts with electrons of atoms in bones and tissues when they are directed into these structures (David et al., 2009), during the interaction the photon's energy undergoes either absorption, scattering or partial absorption with scatter and the complete penetration (Bushberg et al., 2002; Ervin & Podgorsak, 2005; Michael et al., 2004). Collectively these processes that X-ray photons encounter during interaction with matter are known as attenuation (Olubamiji, 2011).

The equation (2.28) describes the attenuation of X-ray photons as they transverses through the sample (Bushberg, et al., 2002). The attenuated intensity (I) of the X-ray photons detected by the detector is accordingly expressed using the Beer-lamberts' equation (Hendee & Ritenour, 2002), which describes the extent of attenuation that X-ray radiation undergoes when passing through a certain thickness of material, Beer-lambert's equation is indicated as equation (2.28) (David et al., 2009).

$$\mathbf{I = I_0 e^{-\mu x}} \qquad (2.28)$$

where initial intensity, (I_0),is the initial intensity of the X-ray beam, variable (x) is the thickness of the sample and (μ) is the sample's linear attenuation coefficient (David et al., 2009). The linear attenuation coefficient depends on the atomic number(Z), material density(ρ), and the photon energy (E) (Dance et al., 2012).The attenuation coefficients are sometimes given in mass attenuation coefficient, because of dependence of linear attenuation coefficient on material's density (David et al., 2009). Equation (2.29) can be further written as:

$$\mathrm{I = I_0 e^{-\left(\frac{\mu}{\rho}\right)\rho x}} \qquad (2.29)$$

where $\left(\frac{\mu}{\rho}\right)$ is called mass attenuation coefficient with units cm^2/g.

The quantity of X-ray photons transmitted through the patient is determined by certain properties such as thickness of the tissue (David et al., 2009), density or atomic number of the tissue, and the energy of the X-ray beam (Dendy & Heaton, 1999). The atomic number and density of bone tissue is higher than that of fat and muscles (soft tissue) (Michael et al., 2004). Figure 9 illustrate the mass attenuation coefficient as a function of X-ray photon's energy (David et al., 2009), observations made from Figure 9 reveals that it is pragmatic that materials with less density such as fats and muscles attenuate X-ray photons less as compared to anatomical structures with high density such as bones (Dumela, 2010).

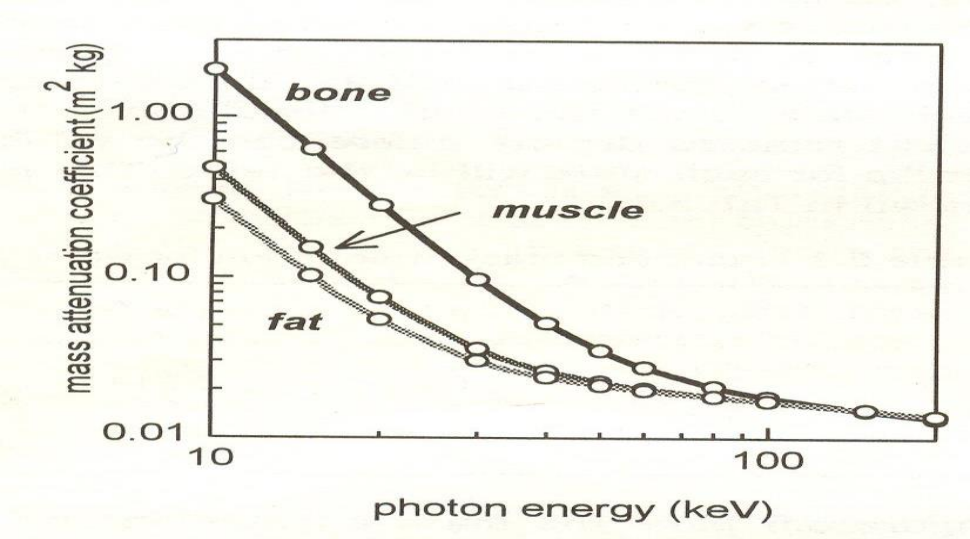

Figure 9: The mass attenuation coefficient of bone, muscle and fat as a function of photon energy (Dumela, 2010).

The low energy X-ray photons are absorbed less in fat than in equal mass attenuation coefficients of soft tissues or bones (David et al., 2009), and the same quality of X-ray photons is absorbed more in bones than in an equal mass of soft tissue as indicated in Figure 9 (Dumela, 2010). However, the complete attenuation or absorption of X-ray photon energy is a composite of different types of processes that are briefly discussed below (David et al., 2009).

a) Photoelectric effect

Photoelectric effect or absorption occurs when the incident X-ray photon transfers its energy to the inner orbital electron of the tissue's atom (Carl & Gudrun Alm, 1996). The inner electron ends up ejected from the atom with low energy Figure 10 (c); subsequently this ejected electron undergoes complete absorption by the adjacent atoms and contribute to image formation (Bushberg et al., 2002; Carl & Gudrun Alm, 1996). This process is likely to be encountered in high atomic number structures such as bones than in tissues; the prevalence of this process is also dominant in X-ray photons with low energy (Bushberg et al., 2002; Carl & Gudrun Alm, 1996).

b) Compton scattering

This process takes place when the incident X-ray photon is deflected from its original pathway as indicated in Figure 10 (c), this occurs during the interaction of a photon with the orbital electron such that the orbital electron accumulates energy from the photon and eventually undergoes emission from the atom as indicated in Figure 10 (c) (Bushberg et al., 2002). The photon loses part of its energy during interaction and continues to travel towards the detector in the new pathway (Garrett et al., 1980; Dendy & Heaton, 1999). This process is independent of the atomic number of the objects because X-ray photons involved consist of sufficient energy to thrive after being scattered (Garrett et al., 1980).

c) Rayleigh scattering

Rayleigh or coherent scattering occurs when the low energy X-ray photons interact with the atom such that no energy deposition takes place as well as electron emission, because the binding energy of the orbital electrons is greater than the energy of the photon (Michael et al., 2004; Bushberg, et al., 2002). However, in Figure 10 (a) the incident photon will be scattered immediately upon collision with the atom and travel in an altered direction (Dendy & Heaton, 1999). Rayleigh scattering is likely to occur when low energy photons interact with high atomic number objects (Dendy & Heaton, 1999).

d) Pair production

This process is significant at X-ray photon energies of about 10MeV even though the process itself occurs at photon energies greater than 1.02MeV (Whaites & Cawson, 2002; Carl & Gudrun Alm, 1996). The electron and positron/positron-electron pair is emitted during the annihilation of an X-ray photon as it interacts with the nucleus of the tissue atom as shown in Figure 10 (d), afterwards positron will disappear (short-lived) or undergoes annihilation creating two photons of 0.51 MeV energy (Michael et al., 2004). Pair production is predominant when high-energy photons interact with high atomic number materials (Martin, 2002).

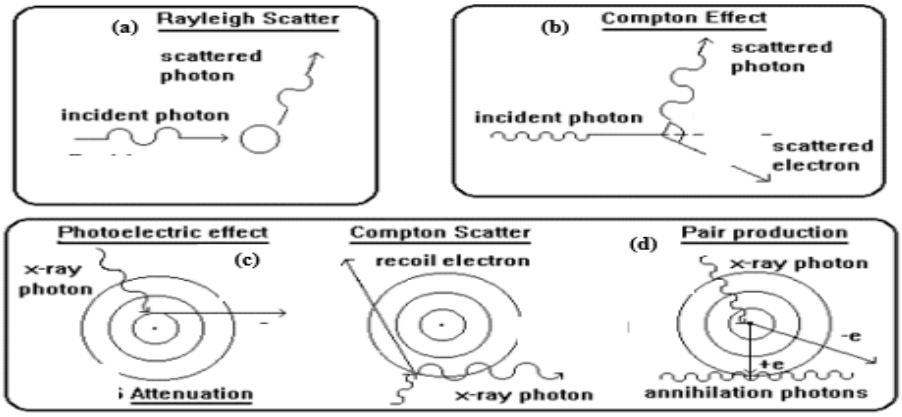

Figure 10: Depiction of X-ray attenuation processes (Seakamela, 2016).

2.7. Principle of X-ray detection

In X-ray radiography, a device that changes X-ray into visible image is known as image receptor (RSNA, 2010). Different image receptors produce different images in terms of visibility or quality (Sprawls, 1985). Image receptors in X-ray radiography used to be the screen-film based (Sprawls, 1985). The X-ray film consist of single or double emulsion of silver bromide (AgBr) fixed on the gelatin. The film is placed between intensifying phosphor screens (Sprawls, 1985); the function of the screen-film was to convert the X-ray beam transmitted through the patient into light which will be further processed to form an image.

The International Commission on Radiological Protection (ICRP), in its publication No. 93 is of view that due to technological advancement, the use of film in X-ray radiography is distinctly outdated over the years, and is replaced by digital detectors (ICRP 93, 2001). Digital radiography has its own advantages over screen-film radiography; some of those advantages entail increased dynamic range and provision of digital images, which allows ease image post-processing, storage and display (Begum, 2001). Generally digital radiography is classified into two categories, computed radiography (CR) and direct digital radiography; these two categories are further discussed below (RSNA, 2010).

2.7.1. Computed radiography

The computed radiography (CR) system uses photostimulable phosphor detector (Whaites & Cawson, 2002). The exposure of computed radiography detector to X-ray radiation in Figure 11 initiates the storage of photon energy within phosphor crystal (RSNA, 2010). The phosphor crystals that are commonly used in computed radiography detectors are fluorohalides crystals that are normally encapsulated in an imaging plate (Whaites & Cawson, 2002). Figure 11 shows that the laser beam is usually used to scan the plate and the stored energy will be released as visible light (Whaites & Cawson, 2002). The detection of emitted light is through a photomultiplier tube (PMT) which further covert the light into electric signals (David et al., 2009). The electrical signals will be further processed and converted into a digital image. In contrary to screen film based radiography, computed radiography images are of good quality (Mayles et al., 2007). The imaging plates can be exposed further to intense visible light to remove the signal stored on them for reuse purposes as illustrated in Figure 11 (Whaites & Cawson, 2002).

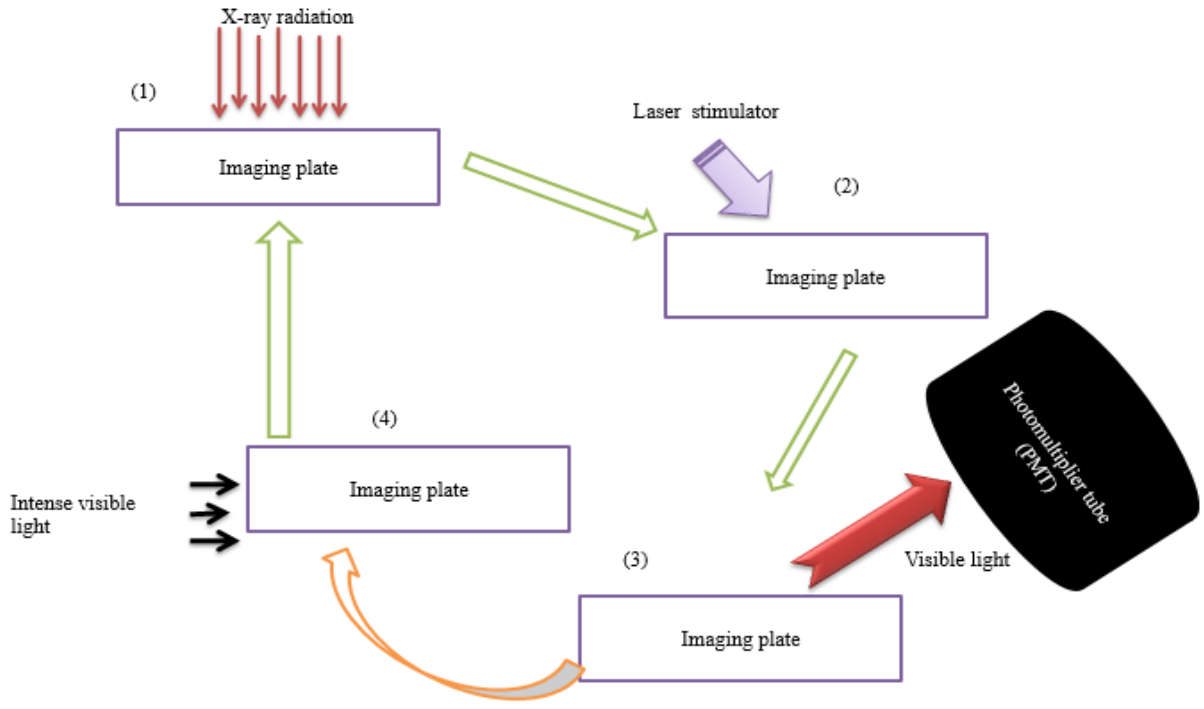

Figure 11: The flow diagram of computed radiography detector process.

2.7.2. Direct digital radiography

Detectors in direct digital radiography are charged coupled devices (CCD) or flat panel detectors (FPD) (Pacella, 2015). There are two types of flat panel detectors, namely, direct conversion detector and indirect conversion detector in Figure 12 below (Pacella, 2015).

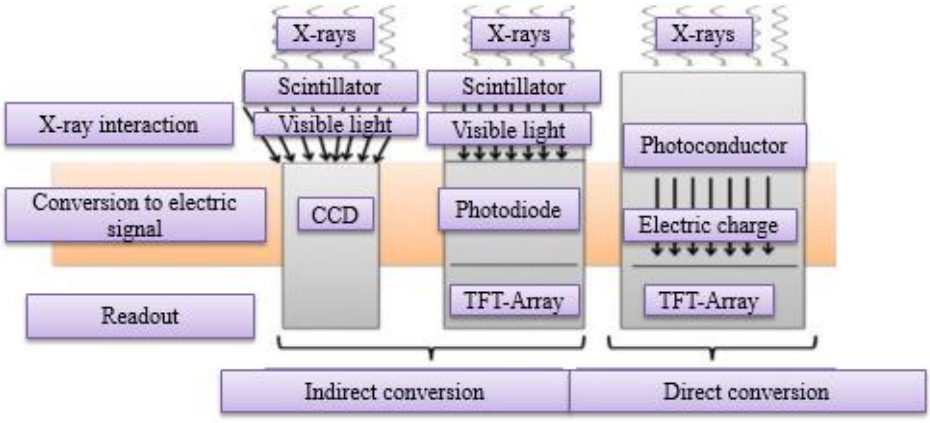

Figure 12: Illustration of typical processes of digital radiography detectors (Pacella, 2015).

The primary aim of these two flat panel detectors is to convert radiation into an electric charge (Gupta et al., 2013). Direct conversion detectors consist of amorphous selenium photoconductor that directly converts X-ray photons into an electric charge (Gupta, et al., 2013). Indirect conversion detectors consist of a scintillator material that converts X-ray photons into visible light, this is indicated in Figure 12 (Gupta et al., 2013). The photodiode will further convert light into an electronic signal. In case where CCDs are employed, the light produced is collected by optical fibres coupled to a CCD before an electronic signal is created (Pacella, 2015). In Figure 12, it is shown that the thin-film transistor (TFT) arrays will further readout an electronic signal using the pixels to produce a digital image. TFTs arrays are used both in direct and indirect conversion detectors to process the electronic signal (Pacella, 2015; Gupta et al., 2013)

Chapter 3: Materials and experimental procedure

The description of methodology and materials used to carry out the experiments of this study will be outlined in this chapter. The description of samples, phantoms and analytical techniques used will also be detailed.

3.1. Materials

3.1.1. The samples used for the X-ray radiography experiment

The actual samples used in this study were body parts of a rat. The rats were terminated and dissected at Wits University; the obtained samples were initially used for another study and thereafter they were acquired for this current study. The samples were the rat's humeri (arm bone), femora (thigh bone), tibias (shinbone) and skulls (complete rat's head). The samples were secured in 10% buffered formalin in plastic containers solution for preservation purpose. The use of musk was strongly recommended when working with the samples as a precautionary measure to reduce inhalation of the formalin solution in areas with poor ventilation. The width of each rat's bone was measured using the Vernier Caliper and it was noted as the thickness in Table 5 below.

Table 5: The measured thickness of the rat samples.

Samples	**Width/Thickness (cm)**
Humeri (arm bone)	0.30
Femora (thigh bone)	0.32
Tibias (shinbone	0.30
Average	0.307
Samples	**Width/Thickness (cm)**
Skull (complete rat's head)	0.45

The samples were gathered together before the experiment and each sample was thoroughly dried using the paper towel prior to scanning. The defined thickness of acrylic glass was used to replace the soft tissue of the rat's limb bones because they were acquired without the original rat tissues. The thickness of acrylic glass was tailored according to the thickness of the actual rat's tissue that was obtained in the literature as 1.01 cm (Osborne, et al., 2012), therefore such

thickness was meant to simulate the thickness of the actual rat's tissue on the limbs. The phantom representing the thickness of the rat limbs was designed using 1 .01 cm thickness of acrylic glass and 0.31 cm thickness of aluminium metal as specified in Table 3. The samples were scanned using the micro-focus X-ray machine for experimental analysis as discussed below.

3.1.2. The phantoms used for the X-ray radiography experiment

Three phantoms of different thicknesses were designed using aluminium metal and acrylic glass in this study. Acrylic glass is a transparent clear thermoplastic with a density 1.18g/cm^3, formula ($C_5H_8O_2$) n and molar mass of 100, 12 g/mol, this material is also known for its good rigidity and stability (Hess & Neitzel, 2012). The different thicknesses of aluminium metal and acrylic glass were representing the average of different thicknesses of rat's limb bones, human palm bones and human limb bones. The aluminium block was embedded inside the acrylic glass. The height of the actual body parts was ignored as the thickness was of main interest in this study, however all the designed phantoms were cylindrical in shape and their height was the height of 40 mm.

The phantoms representing the thicknesses of the human limbs and palm were designed using aluminium and acrylic glass. These materials were tailored according to the measurements of the width, circumference and length of the real human limbs and palm obtained from the following publications: Huang et al., 2012; Singh et al., 2014; Osborne et al., 2012; Garrido Varas & Thompson, 2011; Pan, 1924; Higgins, 1895; Alexander & Viktor, 2010 & Cuk et al., 2012.

The thicknesses of the compact bone and soft tissues of the human palm and three human limbs (upper arm, thigh and shin) was taken into account. The average of the three thicknesses of the compact bone of human limbs and soft tissues was calculated. The resulting thicknesses was taken to be the actual thickness of the human limbs in Table 5; this thickness was used to tailor the thickness of aluminium metal and acrylic glass to design the phantom representing the thickness of the human limbs as indicated in Table 6. The thicknesses of the soft tissues and compact bone of the human palm as obtained from the literature was used to design the phantom representing the human palm thickness using aluminium metal and acrylic glass. Each thickness of the real tissues was multiplied by 2 in Table 7 during the design with aluminium

and acrylic glass to account for the beam path, the X-ray beams will transverse the phantom twice during transmission.

Table 6: The thicknesses of the compact bone and soft tissue of the human limb and palm.

Human limbs thickness		
Body part	**Thickness of the compact the bone (cm)**	**Thickness of soft tissue (cm)**
Thigh (femur)	1.20	4.87
Shin (tibia)	0.70	2.25
Upper arm (humeri)	1.00	0.128
Average	0.967	2.416
Human palm thickness		
Body part	**Thickness of the compact the bone (cm)**	**Thickness of soft tissue (cm)**
Palm (Phalanges and metacarpals)	0.69	1.39

Table 7: The thicknesses of the materials used to simulate the thicknesses of the bone tissue and soft tissue of the human limbs.

Phantoms	**Thickness of Acrylic glass (cm)**	**Thickness of aluminium (cm)**
Human limbs	2.42x2=4.84	0.97x2=1.94~2.00
Rats limbs	1.01x2=2.02	0.31x2=0.61
Human Palm	1.39x2=2.78	0.69x2=1.38

3.1.3. Micro-focus X-ray machine

The micro-focus X-ray machine in Figure 13 was used in this study, this machine is based at Necsa (South African Nuclear Energy Corporation) radiation science unit, the machine is Nikon XTH 225 ST system (Hoffman, 2012). In this study, the X-ray experiments were performed with the micro-focus X-ray machine using the dedicated phantoms and samples. The micro-focus X-ray machine is an imaging modality that allows the acquisition of the interior information of an object non-destructively and non-invasively (Hoffman, 2012).

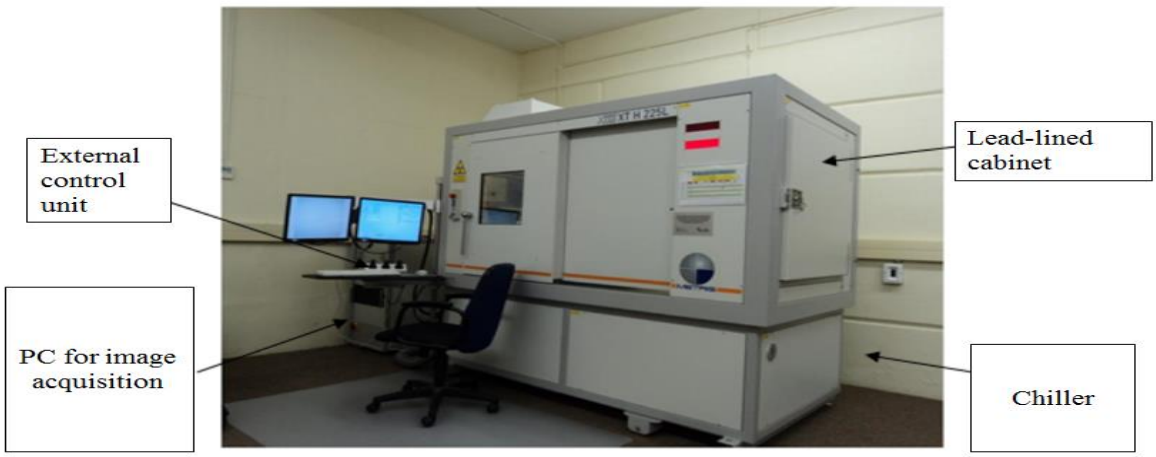

Figure 13: Micro-focus X-ray machine (Hoffman, 2012).

The micro-focus X-ray machine consists of four components as indicated in Figure 13; those components are a lead-lined cabinet, an external control unit, a chiller and personal computer (PC) for image acquisition (Hoffman, 2012). The main components of this system are X-ray tube, a sample holder/stage and 2D high system resolution flat panel detector. The major components of this system are encapsulated within the lead-lined cabinet (Hoffman, 2012). The function of the lead-lined cabinet in the X-ray machine is to maintain the radiation dose limit of not more than 1 micro-Sievert per hour (Hoffman, 2012). The characteristics and the sample stage of the micro-focus X-ray machine are discussed below.

A. The characteristics of micro-Focus X-ray machine

The power rating of micro-focus X-ray machine is approximately, 30W which allows the scanning of quite a variety of samples with different densities. The system consists of a voltage range of $30\ \text{kV} - 225\ \text{kV}$ and a beam current of $0 - 1\ mA$. The focal spot on the anode metal target ranges up to 0.003 mm; hence, the micro-focus machine is mainly characterized as the high-resolution technique that provides the efficient reduction of unsharpness in the image. The flat panel detector installed in the micro-focus X-ray machine consists of a 16-bit dynamic range of up to 65335 pixel value. The flat panel detector of the micro-focus X-ray machine based at Necsa is commonly has a physical size of $400\ \text{mm} \times 400\ \text{mm}$ with pixel size of $200\ \text{micron} \times 200\ \text{micron}$ (Hoffman, 2012).

B. The sample stage of Micro-Focus X-ray machine

Each sample was thoroughly dried before the scan. The samples and phantoms were supported using the polystyrene foam material during the scan as illustrated in Figure 14 below. The mass attenuation coefficient of the Styrofoam material causes negligible X-ray attenuation; hence this material was adopted for support and stabilization of the sample during the scan. Figure 14 shows the polystyrene foam material supporting the samples or phantoms which were positioned properly on the stage inside the micro-focus X-ray machine during the scan. The stage is then tilted prior to scanning using the external control panel of the micro-focus X-ray machine for optimal spatial resolution. This adjustment also ensures that the sample is fully visualized in the 2D radiograph's field of view.

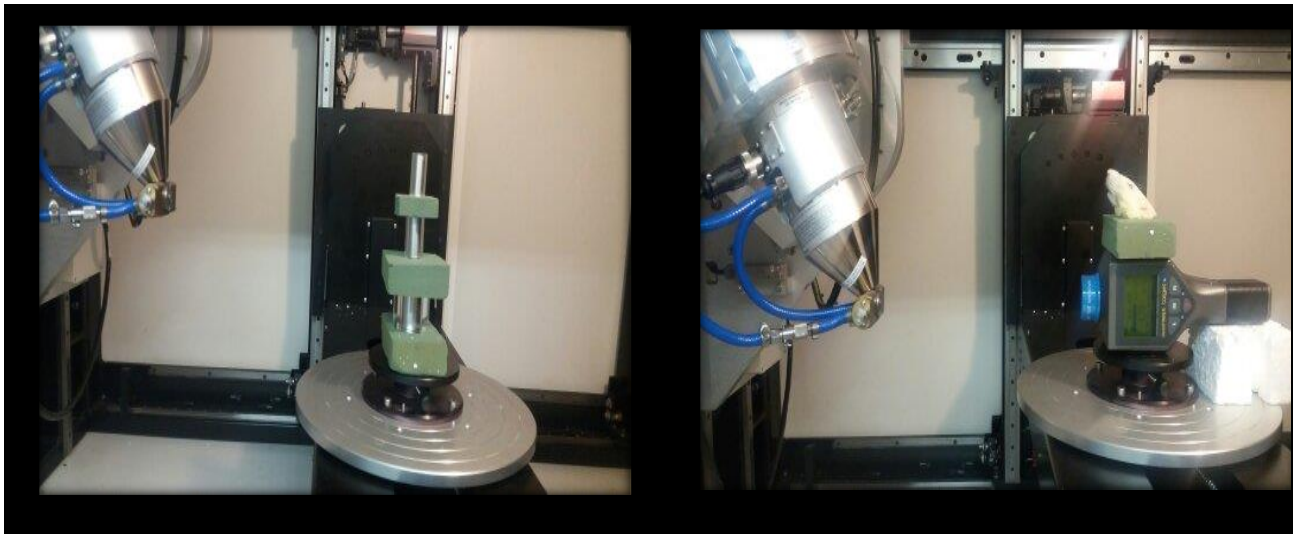

Figure 14: Positioning of the sample and phantoms on the stage during the experiments.

3.1.4. Radiation dose detector

The radiation dose detector that was used for detection of radiation dose in this study is known as Identifinder instrument, this is clearly indicated in Figure 15 below. The Identifinder is a family of digital spectrometers that are able to detect gamma photons (Thermo Fisher Scientific, 2008; ICX Technologies, 2003). Different types of Identifinder detectors have different physical sizes and software. The main use of this radiation detectors is to identify artificial and natural radionuclides by using high sensitivity to wide range of dose rate through the use of it's components (Thermo Fisher Scientific, 2008). The Identifinder is also known for it's precise rapidness to locate and measure radiation dose from gamma radiation sources, the X-ray sources can also be measured with this detector (Thermo Fisher Scientific, 2008).

The display screen of Indentifinder and three button can be operated with ease. The Indetifier package includes a carry bag, wrist band, charging unit, holster and software for analysis. The components of the indentifier are voltage power supply,multi-channel analyzer, amplifier, NaI (Tl) scintillator and a Geiger-Muller tube (GM tube) (ICX Technologies, 2003). The purpose of Geiger-Mueller tube is for the measurements of high dose rate. The wrapped ^{3}He tube with moderator is used in case of neutron detection (ICX Technologies, 2003).

Figure 15: Illustration of measurement of radiation dose with identifier (Thermo Fisher Scientific, 2008).

The Identifinder Ultra was used to measure radiation dose in this study due to its availability and sensitivity to photons (ICX Technologies, 2003). The Identifinder Ultra in Figure 15 has a physical size of $25\ \text{cm} \times 9\ \text{cm} \times 8\ \text{cm}$ and a weight of 1250g. The Identifinder Ultra use a special mode for stabilization and autocalibration, unlike other types of identifinders a radioactive source is not need for stabilization of Identifinder Ultra. The background radiation was measured before the experiment and it was found to be $1.42\ \mu\text{Sv/hr}$ (ICX Technologies, 2003). The detector was positioned along with the samples and phantoms in the stage in relation to the X-ray source at the specified FSD during the measurements as indicated in Figure 14. The X-ray scanning parameters that were used to acquire the radiographs of rat samples and phantoms were also used to measure the radiation dose (Thermo Fisher Scientific, 2008).

3.2. Experimental procedure

The experimental procedure of this study was meant for the investigation of X-ray scanning parameters that gives optimal image quality with minimized initial radiation dose. The initial radiation dose gives an idea in terms of quantity (high or low) of the dose that will be absorbed by the subject. This experimental procedure was divided into three sections of X-ray scanning parameters and each section involved the scanning of phantoms and real samples dedicated for this study. The real samples used in this study were the rat's humeri (arm bone), femora (thigh bone), tibia (shinbone) and skulls (complete rat's head) whereas the three phantoms were simulating the thickness of the human palm, human limbs and the rat's limbs.

The X-ray experiments were performed with micro-focus X-ray machine, in which the acquisition of radiographs of phantoms and real samples was done by varying each X-ray scanning parameter while others were kept constant. The same X-ray scanning settings that were used to acquire the radiographs of phantoms and real samples were used to measure the initial radiation dose with radiation dose detector. The measurements of radiation dose were achieved by placing the radiation dose detector in the sample stage of the X-ray machine and the X-ray scanning parameter of interest was varied (others kept at constant) exactly the same way as it was varied during the acquisition of radiographs. The X-ray scanning parameters that were investigation in this study are the X-ray tube parameters (voltage, current and exposure time), the focal-sample distance and the X-ray filter thicknesses. The investigation of the variation of these X-ray scanning parameters are further discussed below.

3.2.1. Determination of the effect of varying X-ray tube parameters

The acquisition of the radiographs of both samples and phantoms dedicated for this study was performed by varying each X-ray tube parameter through three investigations. The radiation dose was also measured using the radiation dose detector with the same X-ray settings that were used to acquire the radiographs. The varied X-ray tube parameters were voltage, current and exposure time.

3.2.1.1. The varying of the X-ray tube voltage

The acquisition of the radiographs of each rat sample was performed by varying the X-ray tube voltage from 30 kV to 175 kV while X-ray tube exposure time was kept constant at 1 sec, X-ray tube current at 100 µA, FSD of 35 cm without any thickness of X-ray filtration. The

radiation dose detector was placed on the sample stage to measure the radiation dose after the acquisition of all the radiographs, the radiation was measured with the same X-ray settings that were used for acquisition of all the radiographs of the rat samples. The radiographs of the three phantoms were acquired simultaneously with the same X-ray voltage range that was used to scan the rat samples but other X-ray scanning parameter were kept constant at the X-ray tube exposure time of 1 sec, X-ray tube current at 60 µA, FSD of 73 cm without any thickness of X-ray filtration. The radiation dose detector was used exactly the same way as it was used to measure the rat's sample radiation dose but this time with the X-ray settings that were used to acquire the radiographs of the phantoms.

3.2.1.2.The varying of the X-ray tube current

The X-ray tube current was varied from 5µA to 190 µA during the acquisition of the radiographs of each rat samples and phantoms. The X-ray tube exposure time was kept constant at 1 sec, X-ray tube voltage at 100 kV, FSD of 35 cm without any thickness of X-ray filtration during the acquisition of the radiographs of each rat samples. During the acquisition of the radiographs of the phantoms, the X-ray tube exposure time was kept constant at 1 sec, X-ray tube voltage at 100 kV, FSD of 73 cm without any thickness of X-ray filtration. The radiation dose detector was placed on the sample stage to measure the radiation dose after the acquisition of all the radiographs of the rat samples and phantoms. The radiation was measured distinctively for rat samples and phantoms using the same X-ray settings that were used to acquire the radiographs.

3.2.1.3.The varying of the X-ray tube exposure time

The variation of X-ray tube exposure time was between 0.267 second and 4 seconds during the acquisition of the radiographs of each rat samples and three phantoms. The rat samples were scanned with the X-ray tube voltage kept constant at 100 kV, X-ray tube current at 100 µA, FSD of 35 cm without any thickness of X-ray filtration. The three phantoms were scanned simultaneously with the X-ray tube voltage at 100 kV, X-ray tube current at 100 µA, FSD of 73 cm without any thickness of X-ray filtration. The radiation dose was measured for rat samples and phantoms using the X-ray scanning settings that were used to acquire the radiographs.

3.2.2. Determination of the effect of varying focal-sample distance

The focal-sample distance (FSD) was varied during this investigation, this parameter was varied from 15 cm-73 cm and the total distance between the X-ray source and the detector was measured to be 115 cm. The effect of varying the focal-sample distance (FSD) on bone radiography and radiation dose with constant X-ray tube voltage, X-ray tube current and exposure time was established from the known values of the FSD. The values of the FSD were determined by subtracting each value of FSD from the total distance between the X-ray source and the detector. In this regard, the radiographs of the phantoms and samples were acquired for different values of the FSD, the radiation dose was also measured using these values.

3.2.2.1.The varying of the focal-sample distance

The FSD was varied from 15 cm to 73 cm during the acquisition of radiographs of each rat's sample and for all phantoms. The X-ray tube exposure time was kept constant at 1 sec, X-ray tube voltage at 100 kV, X-ray tube current at 100 µA without any thickness of X-ray filtration for acquisition of the radiographs of each rat's sample. The same X-ray settings were used to measure the radiation dose by placing the radiation dose detector in the sample stage. The phantoms were also scanned without any thickness of X-ray filter with X-ray tube exposure time of 1 sec, X-ray tube voltage of 100 kV and X-ray tube current of 100 µA, the radiation dose for phantoms was measured using these scanning parameters with varied sample detector distance.

3.2.3. Determination of the effect of varying different types of X-ray filter thicknesses

This study involved the investigation of four different types of X-ray filtration metals, thickness of these metals were varied during the acquisition of radiographs and measurement of initial radiation dose of both the rat samples and phantoms. The X-ray metal filters that were investigated are copper (Cu) X-ray filter, silver (Ag) X-ray filter, aluminium (Al) X-ray filter and tin (Sn) X-ray filter. During the variation of different thickness of each of these X-ray filters, the X-ray tube exposure time was kept constant at 1 sec, X-ray tube voltage at 100 kV, X-ray tube current at 100 µA and FSD at 65 cm. The investigation of different thickness of these metals are summarized in Table 8 below.

Table 8: Illustration of different thicknesses of different filters that were used in this study.

Cu X-ray filter thickness (mm)	**Al X-ray filter thickness (mm)**	**Sn X-ray filter thickness (mm)**	**Ag X-ray filter thickness (mm)**
0.10	0.10	0.10	0.125
0.25	0.25	0.25	0.25
0.50	0.50	0.50	1.00
1.00	1.00	1.00	
1.50	1.50		
2.00	2.00		
2.50	2.50		

3.3. The analysis of radiographs

The images acquired from X-ray radiography experiments were analysed using ImageJ software. ImageJ is a Java-based image processing program, it is a public domain and easily accessible for usage within the scientific community on the internet (Unruh, 2015). The set of icons in ImageJ interface include tools that allow image manipulations. This software provides processing, analysis and edition of 32-bit, 16-bit and 8-bit images. The software allows the installation of plugins for simulation purposes (Unruh, 2015).

In this study ImageJ software was used to quantify pixel value measurements (minimum and maximum pixel value, mean pixel value and standard deviation) of specific pre-defined regions of interest in the radiographs. The pixel value measurements were obtained for each image stack that was acquired for each X-ray scanning parameter that was explored. The acquired images were transferred to ImageJ for analysis after experiments.

The two regions of interest were selected in each image in the stack for computing pixel value measurements therefore two data sets were acquired for the regions of interest (ROI_1 and ROI_2). The regions of interests were selected on the projected sample or phantom within the radiograph, the first region of interest was marked on the bone tissue and the second region of interest was marked on the soft tissue or acrylic glass in case of rat samples. In case of the phantoms, the first region of interest was marked on the aluminium metal and the second region

of interest was marked on the acrylic glass. The data set of pixel value measurements obtained through ImageJ software was further used to calculate the image quality indicators for each X-ray scanning parameters. The following equations were used to calculate the image quality indicators.

3.3.1. Contrast to noise ratio

The contrast to noise ratio expression is a mathematical expression that depends on mean pixel value and standard deviation, this equation was previously used to analytically measure the image quality in the study conducted by Hess & Neitzel, 2012. The data set obtained from the regions of interests was used to calculate the contrast to noise ratio (CNR) using the equation (3.1)

$$\mathrm{CNR} = \frac{\overline{x_1} - \overline{x_2}}{\sqrt{\frac{1}{2}(\sigma_1)^2 + (\sigma_2)^2}} \qquad (3.1)$$

where x_1 and x_2 are the mean pixel values and σ_1 and σ_2 are the standard deviations of the first region of interest and second region of interest. The selected region of interest was marked in acrylic glass or soft tissues and aluminium metal or bone tissues in rat samples and phantoms.

3.3.2. X-ray penetration

The percentage of X-ray flux that penetrated both the rat samples and phantoms was used as image quality indicator in this study. The ability of an X-ray beam to penetrate the object is dependent on the energy of the X-ray photons (Sprawls, 1994). Some of the X-ray photons undergo absorption and scattering while other photons undergoes complete penetration (Seakamela, 2016). The X-ray photons that were transmitted through the samples and phantoms contributed to the formation of a radiograph in the detector, the quality of this radiographs were dependent on the quantity and quality of X-ray photons transmitted soft tissues or acrylic glass and bone tissue or aluminium metal in rat samples or phantoms.

The percentage X-ray penetration (P) was calculated from mean X-ray values obtained from selected regions of interests in rat's sample and phantoms. The projected bone tissue or aluminium metal was the first region of interest (ROI_1) whereas the soft tissue or acrylic glass

was marked the second region of interest (ROI_2). The percentage X-ray penetration (P) was calculated according to equation (3.2) below

$$\mathrm{P} = \frac{x_1}{x_2} \times 100\% \qquad (3.2)$$

where x_1 and x_2 are the mean pixel values selected at the first region of interest and second region of interest respectfully.

3.3.3. Geometric unsharpness

The geometric unsharpness of the image is caused by characteristics of the geometry of the X-ray source (Sprawls, 1994). The two important factors that should be taken into account when calculating the geometric unsharpness are the focal spot size (f) and the ratio of the distance between the X-ray source and the sample (a) and the distance between the sample and the detector (b). The formula that was used to calculate geometric unsharpness (Ug) in this study was given as equation (3.3) below

$$U_g = f \times \frac{\mathrm{a}}{\mathrm{b}} \qquad (3.3)$$

where f is the size of the focal-spot in the X-ray tube, a is the distance between the X-ray tube and the sample and b is the distance between the sample and the detector.

3.3.4. Resolution

The resolution as previously defined in the literature, is the ability of an imaging system to distinguish structures of the object that are close to one another. Resolution was calculated from pixel size and magnification of digital radiographs obtained from Micro-focus X-ray machine. Magnification is the process of amplifying the small details of an object in the field of view. The small details of the interior objects of samples and phantoms used in this study were magnified by increasing the distance between the sample and the detector. The equation (3.4) below was used to calculate magnification M.

$$M = \frac{a + b}{a} \quad (3.4)$$

where a and b represent the distance between the X-ray tube and the sample and the distance between the sample and the detector.

The pixel size was the horizontal and vertical pixel value measurements of the radiographs. The flat panel detector of the Micro-focus X-ray machine used in this study had a physical size of 400 mm × 400 mm with pixel size of 200 micron × 200 micron. The quotient (equation (3.5)) of pixel size PS and magnification M was used for the calculation of resolution R in this study.

$$R = \frac{PS}{M} \quad (3.5)$$

3.3.5. Application of weight sum technique

The weight sum technique involves the conversion of multi-objective optimization problem (MOOP) into a single objective optimization problem (SOOP). The objectives were classified as maximization of image quality and minimization of radiation dose. The image quality indicators were classified under image quality (IQ) objective and initial radiation dose objective as indicated in Table 9. The weight factors were assigned for each objective according to their order of importance and the sum of those weight factors was 1 in each class.

Table 9: Classification of objectives and their designated weight factors.

Image quality (IQ)	**Weight factors**	**Initial radiation dose**	**Weight factor**
Contrast to noise ratio (CNR)	0.39	Initial radiation dose	1
X-ray penetration (P)	0.11		
Resolution (R)	0.36		
Unsharpness (Ug)	0.14		
Total	**1**	**Total**	**1**

The results of image quality indicators for rat samples and phantoms for the investigation of each X-ray scanning parameters were normalized by dividing each data set by its maximum value so that the highest new value in each data set is on 1. The units of some of the image quality indicators were normalized to unit norm. The equation (3.6) below was summarizes the application of weight sum technique in the results of image quality indicators obtained in this study.

$$F_{IQ}(x) = w_{CNR}f_{CNR}(x) + w_P f_P(x) + w_{U_g}f_{U_g}(x) + w_R f_R(x) \qquad (3.6)$$

where F_{IQ} was the resultant image quality objective, f_{CNR}, f_P , $f_{U_g}$and f_R and w_{CNR}, w_P, w_{U_g} and w_R , were the results of image quality indicators (Contrast to noise ratio, X-ray penetration, geometric unsharpness and resolution) and their assigned weight factors and x was the varied X-ray scanning parameter for each investigation. The results of radiation dose objective for the rat samples and phantoms investigation for each X-ray scanning parameter were measured.

Chapter 4: Results and discussion

The results of the image quality indicators and the measured initial radiation dose against the varying of each X-ray scanning parameter before and after optimization are specified in the figures in this chapter, each figure is distinctively discussed. The equations that were used to calculate the image quality indicators are specified in chapter 3, they are stated as equation (3.1) to (3.5) for contrast to noise ratio, X-ray penetration, unsharpness and resolution.

The data set that was obtained from the images of each rat sample and phantom through ImageJ software was used to calculate the image quality indicators. These data set were the mean X-ray flux and its standard deviation for each selected region of interest in the images of samples and phantoms. For each image of the rat sample, two regions of interest were selected, one was selected on the dark region, which was the projected bone material and another region was based on the grey or white region which was the projected soft tissue. In the images of the phantoms and rat bones that were covered with an acrylic glass, two regions of interest were also selected, one was selected on the projected aluminium metal or bones and another region was selected on the surrounding acrylic glass.

The original size of the images that were acquired in this study is 2048 pixels × 2048 pixels. These images were very big and the typical ones that were selected for depiction in this chapter were reduced to 248 pixels × 248 pixels. In the image acquired using the micro-focus X-ray machine, the high attenuative materials (e.g. bone) are darker than the low attenuative material (e.g. air). Therefore, the region in the radiograph with high beam penetration are brighter than the region with low beam penetration.

The set-up parameters in this study are taken from the X-ray tube, the sample position, and the X-ray filters. The influence of each set-up parameters on image quality was discussed before the optimization using the weight sum technique. The results of analysis and optimization are presented in the following sections.

4.1. Optimization of X-ray tube parameters on image quality indicators and initial radiation dose

In this section, the effect of X-ray tube parameters on image quality indicators and initial radiation dose will be established and presented. Weight sum technique was applied on image

quality indicators for optimization and the ultimate image quality objective was calculated. Each X-ray tube parameter was optimized independently and their results are distinctively presented.

The following sections outlines the process of optimization of X-ray set-up parameters, and the effect of X-ray set-up parameters on the quality of radiography.

4.1.1. Optimization of X-ray tube voltage

The analysis of the X-ray tube voltage on image quality was done by varying the X-ray tube voltage from 30 kV – 175 kV with the increment step of 5 kV. Other X-ray scanning parameters such as X-ray current, X-ray tube exposure time and FSD, were kept constant. A series of small portion of the images that were acquired in this range is shown in Figure 16. This series include the images that were acquired from 90 kV – 145 kV.

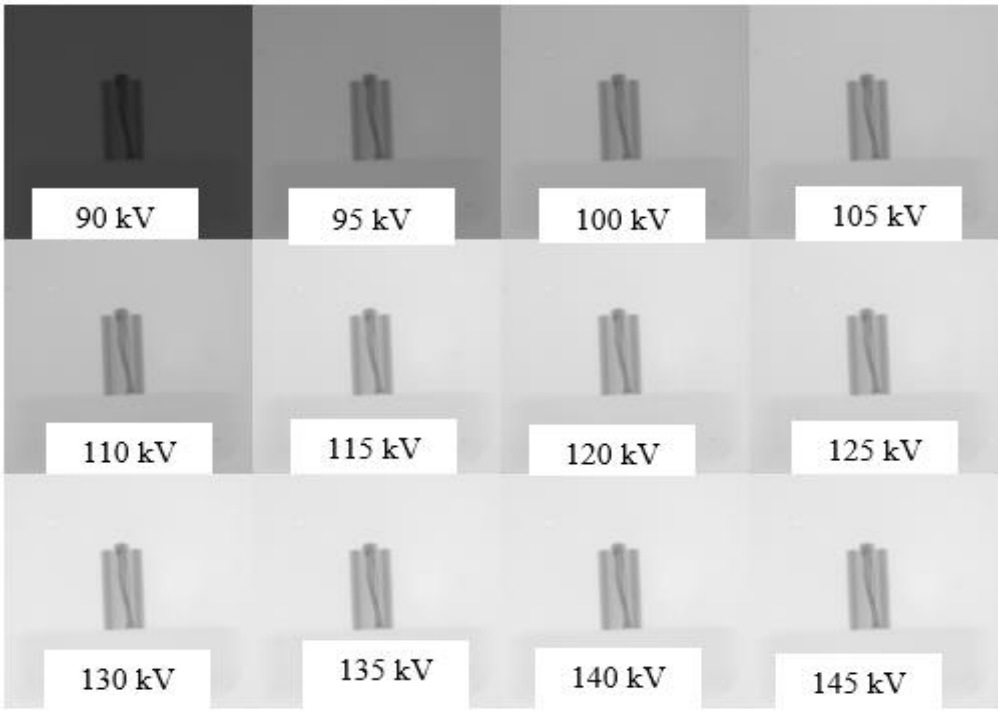

Figure 16: Typical radiographs that were acquired within the X-ray tube voltage range of 90kV-145 kV, X-ray current of 100 µA, FSD of 65 cm and X-ray exposure time of 1 sec.

The effect of X-ray tube voltage on image quality indicators that were used to measure the image quality in this study is thoroughly depicted in Figure 17.

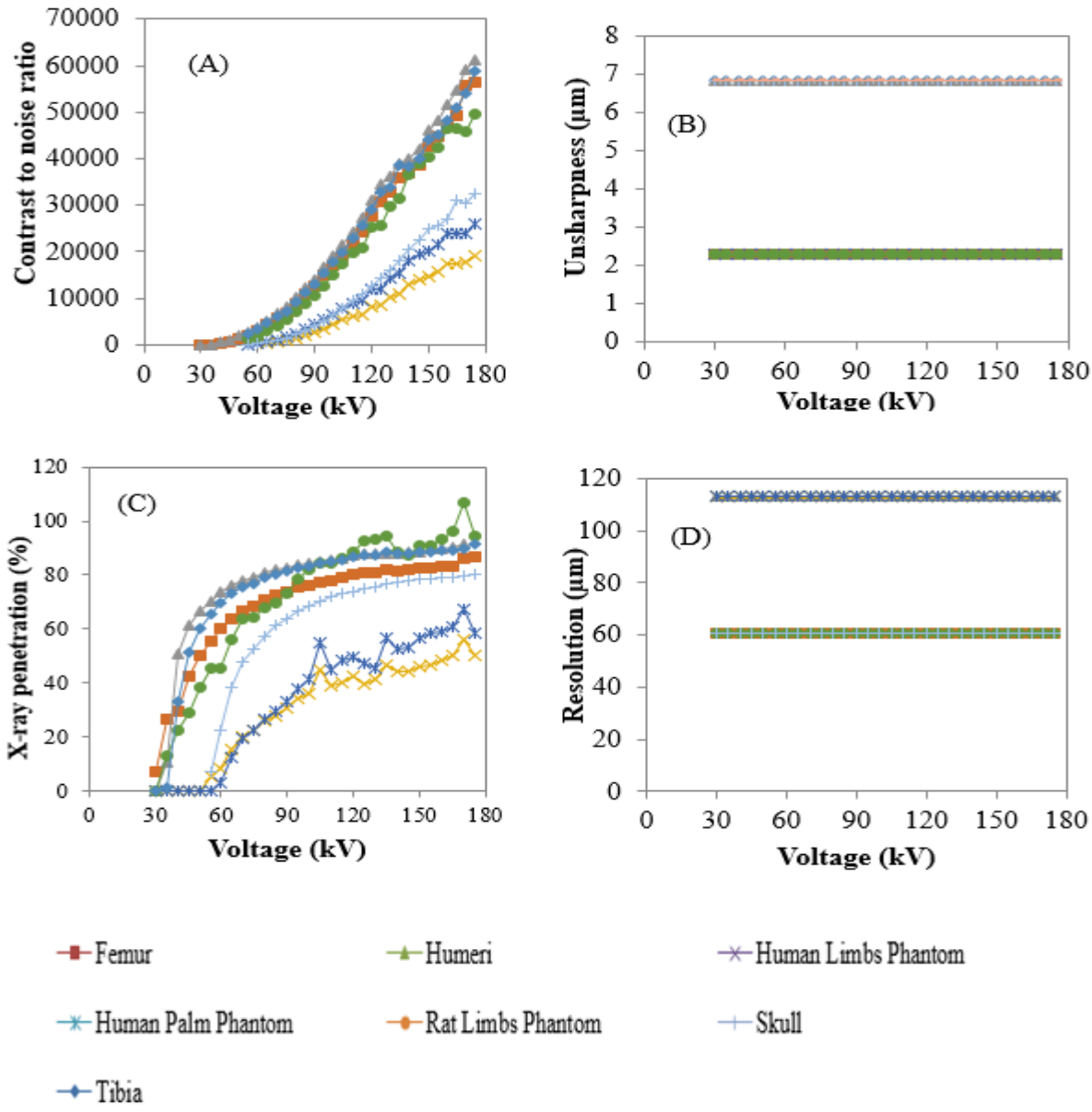

Figure 17: Illustration of the graphs of image quality indicators versus X-ray tube voltage.

There was a change amongst image quality indicators as the X-ray tube voltage increased in Figure 17. At the X-ray tube voltage range of 30 kV – 60 kV, there was a similar trend amongst some of the images of the phantoms and samples in terms of the contrast to noise ratio and X-ray penetration. The contrast to noise ratio and X-ray penetration was very minimal at 30 kV – 60 kV for the radiographs of some phantoms and samples, this incident is due to the occurrence of low energy X-ray photons within that X-ray tube voltage range. Some of these low energy X-ray photons could not penetrate the sample and reach the radiation detector to contribute to image quality formation.

Figure 17 (A) and Figure 17 (C) show that the contrast to noise ratio and the X-ray penetration increased amongst the phantoms and samples as the X-ray tube voltage was increased. Hence, Figure 16, The image that was acquired at 90 kV has poor quality in term of contrast and penetration than the image at 145 kV.

The effect of the X-ray tube voltage on all the image quality indicators was different amongst the samples and phantoms. Figure 17 (A) and Figure 17 (C) shows that the contrast to noise ratio and X-ray penetration of the skull and phantoms simulating the human limbs and palm was the least as compared to all other rat samples and rat limbs phantom above 60 kV. For instance, at 90 kV, the X-ray penetration and contrast to noise ratio of the human limbs phantom was 4266.83 and 30.60% whereas the rat limbs phantoms had 10704.42 and 73.13%.

A linear constant relationship of the unsharpness and resolution was observed in Figure 17 (B) and Figure 17 (D) as the X-ray tube voltage was increased. However, there was a difference between the unsharpness and resolution amongst the images of samples and phantoms in Figure 17 (B) and the positioning of these subjects in relation to the X-ray tube caused Figure 17 (D), this difference. The FSD and other X-ray scanning parameters were kept constant during the X-ray tube voltage experiment. The FSD of the rat samples and phantoms was 65 cm and 73 cm hence the samples had the highest image unsharpness at 6.86 µm and low resolution at 60.90 µm as compared to the images of the phantoms. The effect of X-ray tube voltage on initial radiation dose is illustrated in Figure 18.

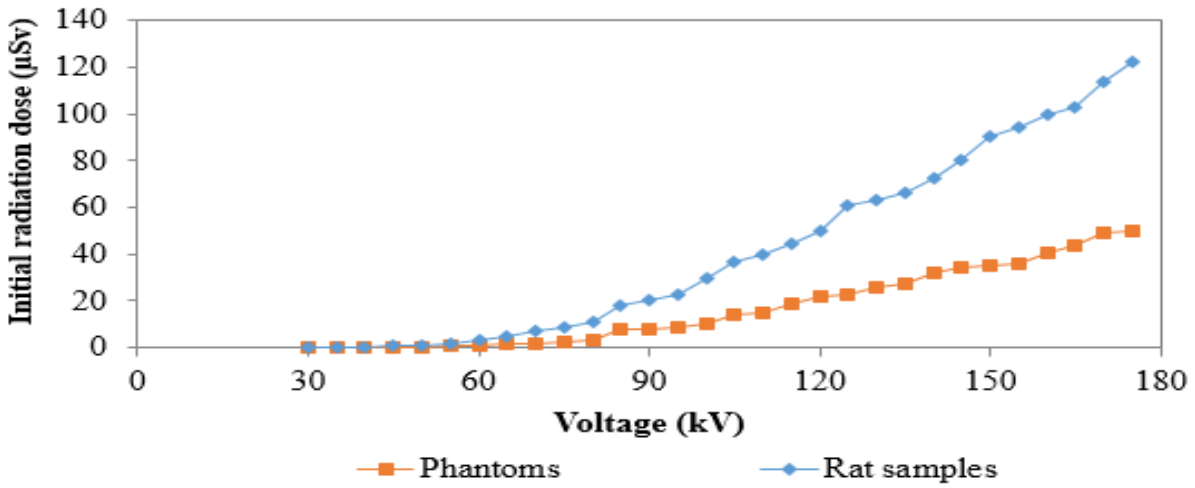

Figure 18: Initial radiation dose versus X-ray tube voltage.

In figure 18, there is a quadratic increase in the measured radiation dose as the X-ray tube voltage was increased for both the phantoms and rat samples. The measured initial radiation dose of the rat samples was high compared to the initial radiation dose of the phantoms, this difference in the measured initial radiation dose is due to the way in which these two subjects were positioned during the acquisition of radiographs. The FSD of the phantoms and rat samples was 73 cm and 65 cm. The rat samples were positioned closer to the X-ray source hence they received high levels of initial radiation dose throughout the varying of the X-ray tube voltage.

The weight sum technique was used to combine the image quality characteristics (contrast, penetration, unsharpness and resolution into a single image quality objective. The effect of X-ray tube voltage on the calculated image quality objective and measured initial radiation dose are presented below

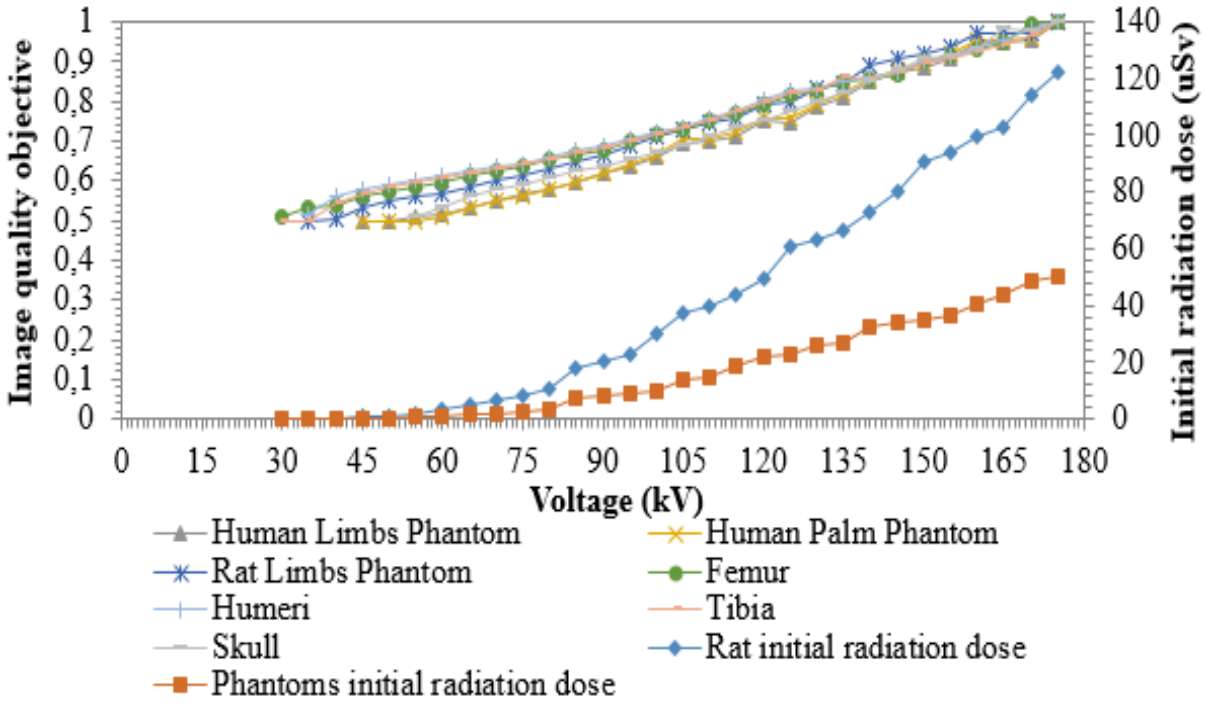

Figure 19: The image quality of the radiographs and initial radiation dose of the rat samples and the phantoms versus X-ray tube voltage investigation.

A linear relationship exists between the image quality and the X-ray tube voltage as seen in Figure 19. The image quality of phantoms simulating the human limbs and rat limbs increased

as there was an increase in the X-ray tube voltage from 30 kV to 175 kV in Figure 19. Furthermore, at X-ray tube voltage of 30 kV, there was no image formation for the rat femur, and again there were no images formed in the X-ray tube voltage range of 30 kV – 50 kV during the imaging of skull. The images of the human palm phantom were also not formed from 30kV to 40kV. Low X-ray energies were attenuated by both samples or phantom, hence they could not be detected below 30kV. The image quality was not evaluated for X-ray tube voltages that did not produce any images. According to the observations made in Figure 19, the phantoms and the rat samples responded similarly to the X-ray exposure, as there was a steady linear increase of image quality both phantoms and samples throughout the increase in X-ray tube voltage.

When the image quality objective is at maximum, the initial radiation dose for both phantoms and rat samples increases. This pattern is observed in Figure 20.

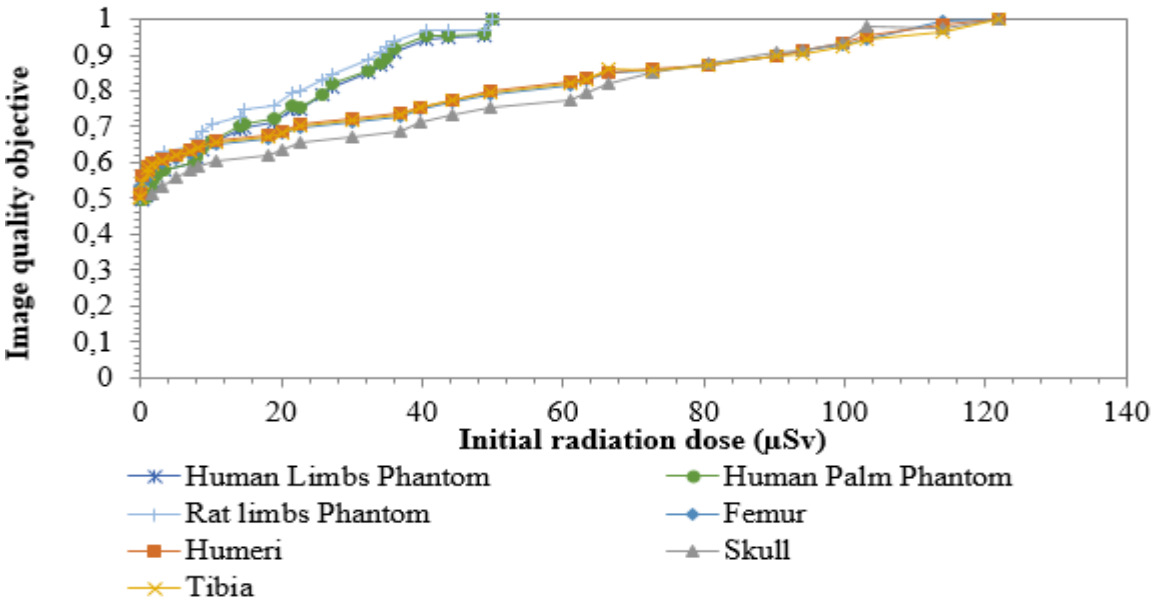

Figure 20: Image quality of the radiographs of the rat samples and phantoms versus initial radiation dose for X-ray tube voltage investigation.

Figure 20 shows that he maximum quality images of the phantoms were acquired with low initial radiation dose, whereas the acquisition of the high quality images of the rat samples were acquired with high initial radiation dose.

The images in Figure 16 were acquired with the initial radiation dose that is above than 20.28 µSv (0.02 mSv), this initial radiation dose correspond to the X-ray tube voltage of 90 kV in Figure 19. However, the most optimal quality images were acquired with the X-ray tube voltage above than 100 kV in Figure 19. The corresponding initial radiation dose at 100 kV in Figure 16 is 29.99 µSv (0.03 mSv). This initial radiation dose is within the limit of radiation reference level that was stipulated by Dianna et al., (2018), in which the radiation reference level that is less than 100 µSv (0.1 mSv) was suggested when acquiring the radiographs of the hand, wrist and the finger. In this regard, the findings of this study suggest that the X-ray tube voltage of 100 kV with X-ray tube current of 100 µA, X-ray exposure time of 1 sec and FSD of 65 cm, can be safely used for optimization of bone images in X-ray radiography.

4.1.2. Optimization of X-ray tube current

During the X-ray tube current investigation, the X-ray tube current was varied from 5 µA to 190 µA with a step increment of 5 µA. Other X-ray scanning parameters such as X-ray tube voltage, X-ray tube exposure time and FSD, were kept constant. The radiographs of the dedicated phantoms and rat samples were acquired, a portion of typical radiographs of the rat tibia are illustrated in Figure 21.

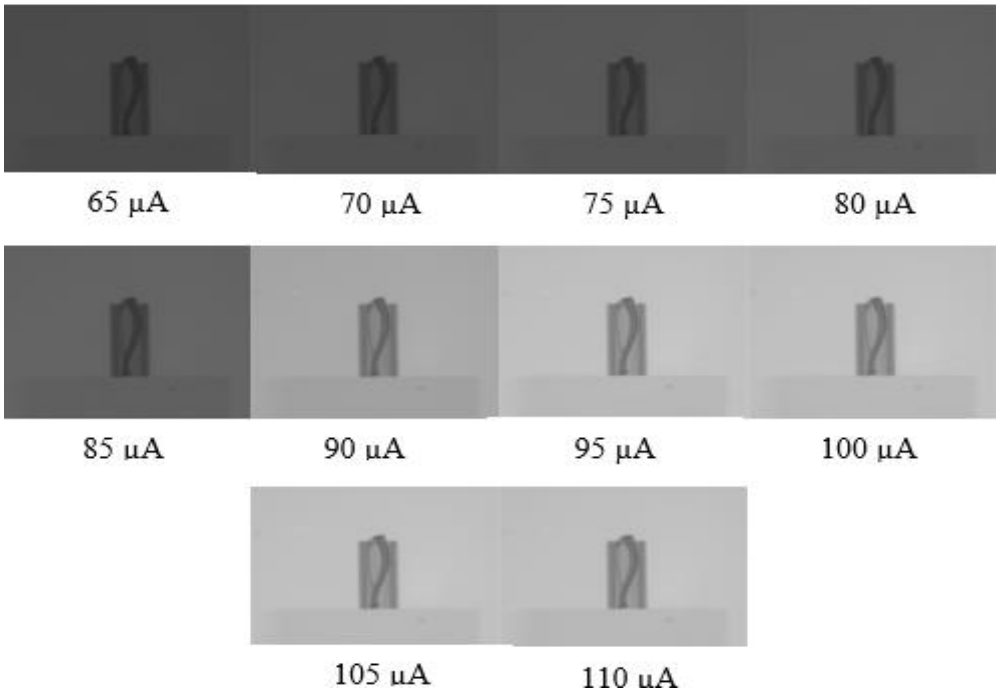

Figure 21: Typical radiographs that were acquired within the X-ray current range of 65 µA - 110 µA, X-ray tube voltage of 100 kV, FSD of 65 cm and X-ray exposure time of 1 sec.

The distinctive effect of X-ray tube current on image quality indicators and initial radiation dose are shown in Figure 22 and 23.

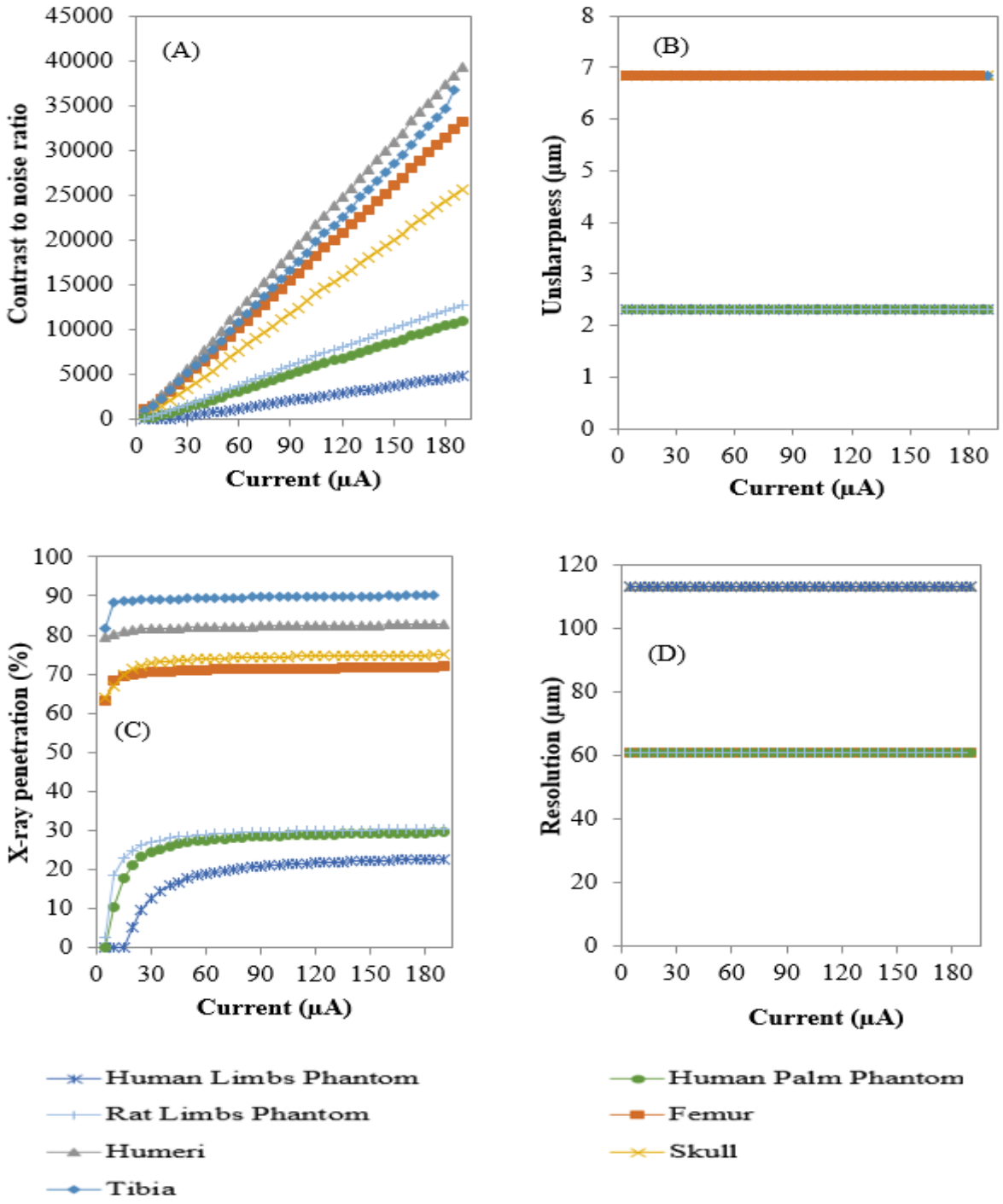

Figure 22: Illustration of the graphs of image quality indicators versus X-ray tube current.

An increase in X-ray tube current had a rapid change in contrast to noise ratio for both the samples and phantoms as shown in Figure 22 (A). A constant linear relationship between the

X-ray tube current and X-ray penetration amongst the phantoms and samples occurred above the X-ray tube current of 60 µA.

Figure 22 (A) and Figure 22 (C) further depicts that the images of the phantoms had the least contrast to noise ratio and X-ray penetration as compared to the rat samples throughout the varying of the X-ray tube current. This might be due to the difference in material thickness between these two subjects, the bone and soft tissue simulating materials in phantoms were thicker than the actual tissues in rat samples. The phantoms had the least X-ray penetration because they attenuated X-rays more during the scan

Figure 22 (C) and Figure (D) portrays the effect of X-ray tube current on the image unsharpness and resolution for both the phantoms and rat samples. These image quality indicators did not change throughout the investigation because the subjects were stationary during the X-ray scans. During the X-ray tube current, the image unsharpness and resolution of the phantoms were constant at 2.31 µm and 113.04 µm, whereas the images of the rat samples were also constant at 6.86 µm and 60.87 µm. The FSD was fixed at 65 cm and 73 cm for samples and phantoms, so there was no change in the image magnification of subjects.

The varying of contrast to noise ratio of the imaged features in Figure 21 occurred as the X-ray tube was varied from 65 µA - 110 µA, the details of the projected rat tibia become more distinguishable above the X-ray tube current of 85 µA. The high attenuating material appeared to be dark whereas the low attenuating material is grey in colour. From Figure 21, it can be concluded that increasing X-ray tube current improves the quality of the image of the desired information as the projected features became more distinguishable and apparent. An increase in the measured initial radiation dose for both phantoms and rat samples as the X-ray tube current was varied is observed in Figure 23.

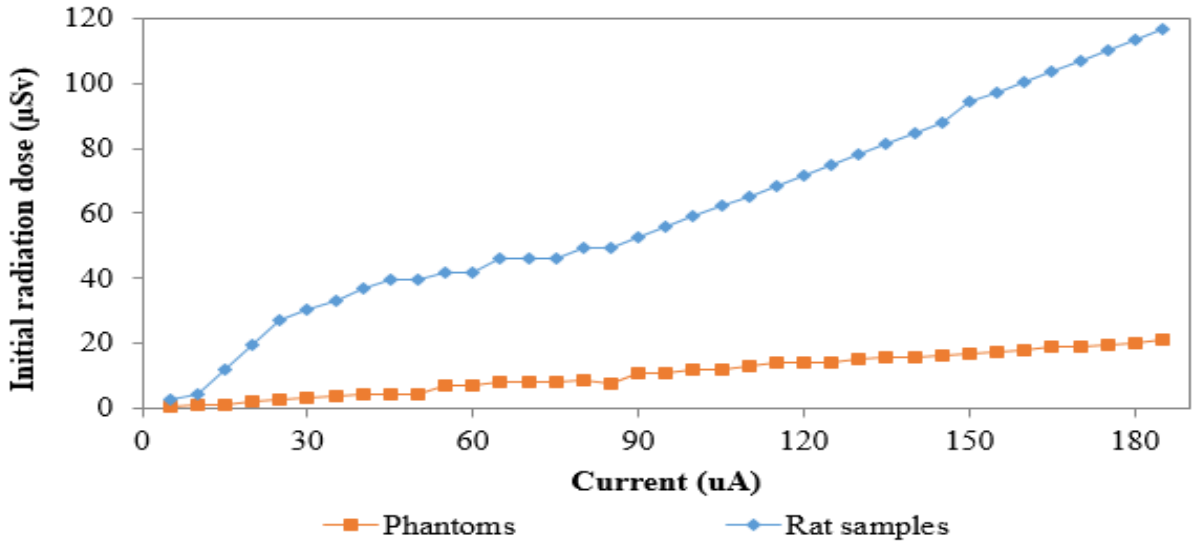

Figure 23: Initial radiation dose versus X-ray tube current.

During the X-ray tube current investigation, the FSD of samples and phantoms was also different during the measuring of the initial radiation dose. The phantoms were positioned at 73 cm from the X-ray source and the rat samples were at 65 cm. According to the inverse square law of radiation, radiation intensity reduces as the subject is moved away from the source, hence the initial radiation dose of the phantoms in Figure 23 is lower than that of the rat samples.

The effect of X-ray tube current on the calculated image quality objective and measured initial radiation dose, was further analysed using the weight sum technique. The effect of X-ray tube current on the calculated image quality objective and measured initial radiation dose are presented in figure 24.

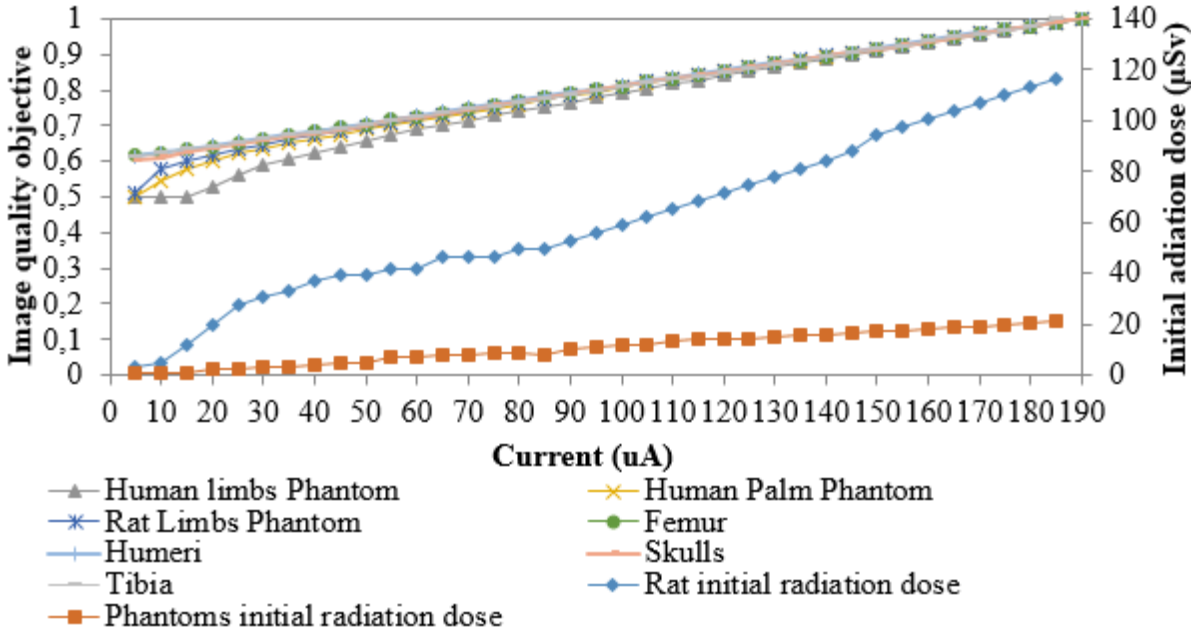

Figure 24: The image quality of the radiographs and initial radiation dose of the rat samples and phantoms versus X-ray tube current investigation.

In figure 24, the increase in X-ray tube current result in the increase of image quality and the initial radiation dose. The value of the X-ray tube current that balances the image quality and the initial radiation dose, need to be found. The initial radiation dose was very minimal below the X-ray tube current of 70µA, this region constitute low quality images as observed in the radiographs in Figure 21, whereas the region above the X-ray tube current of 70 µA revealed high quality images.

The choice of the best value for the X-ray tube current that balance the need for a high quality image obtained a lower radiation dose, is made by plotting the graph of image quality objectives and the radiation dose as shown in the figure below: The radiographs in figure 21 were acquired by increasing the X-ray tube current from 5 µA to 190 µA with the X-ray tube voltage of 100 kV, X-ray tube exposure time of 1 second, FSD of 65 cm and no X-ray filtration. Typical images that were acquired with some of these X-ray settings are depicted in Figure 21.

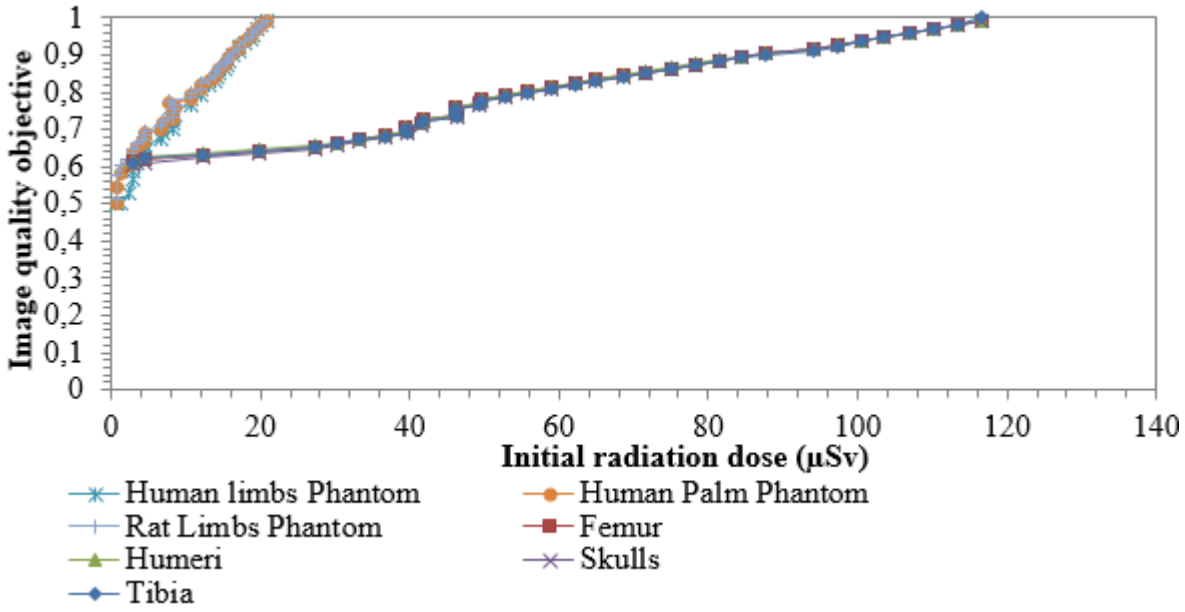

Figure 25: The image quality of the radiographs of rat samples and phantoms versus initial radiation dose for X-ray tube current investigation.

Figure 24 and figure 25 show that optimum quality images can be acquired with the X-ray tube current of 100 µA. The constraint thereof is the initial radiation dose, for instance the radiation dose of 3000 µSv-5000 µSv (3 mSv-5 mSv) is a designated diagnostic reference when acquiring the radiographs of the human skull (Vano et al., 2002). The initial radiation dose that occurred during the acquisition at the X-ray tube current of 100 µA is less than diagnostic reference dose that was postulated by Vano et al., (2002) at 11.99 µSv and 59.11 µSv (0.01 mSv and 0.06 mSv). Therefore, this X-ray tube current (100 µA) with the X-ray tube voltage of 100 kV, X-ray exposure time of 1 sec and no filtration can be used for optimization in X-ray radiography without harming the well-being of the patient.

4.1.3. Optimization of X-ray tube exposure time

The effect of X-ray tube exposure time on image quality was also established. The exposure time was varied from 0.27 to 4.00 seconds. The radiographs of the rat tibia that were acquired within this exposure time range are depicted in Figure 26, where the effect of this X-ray tube parameter on image equality can be clearly observed.

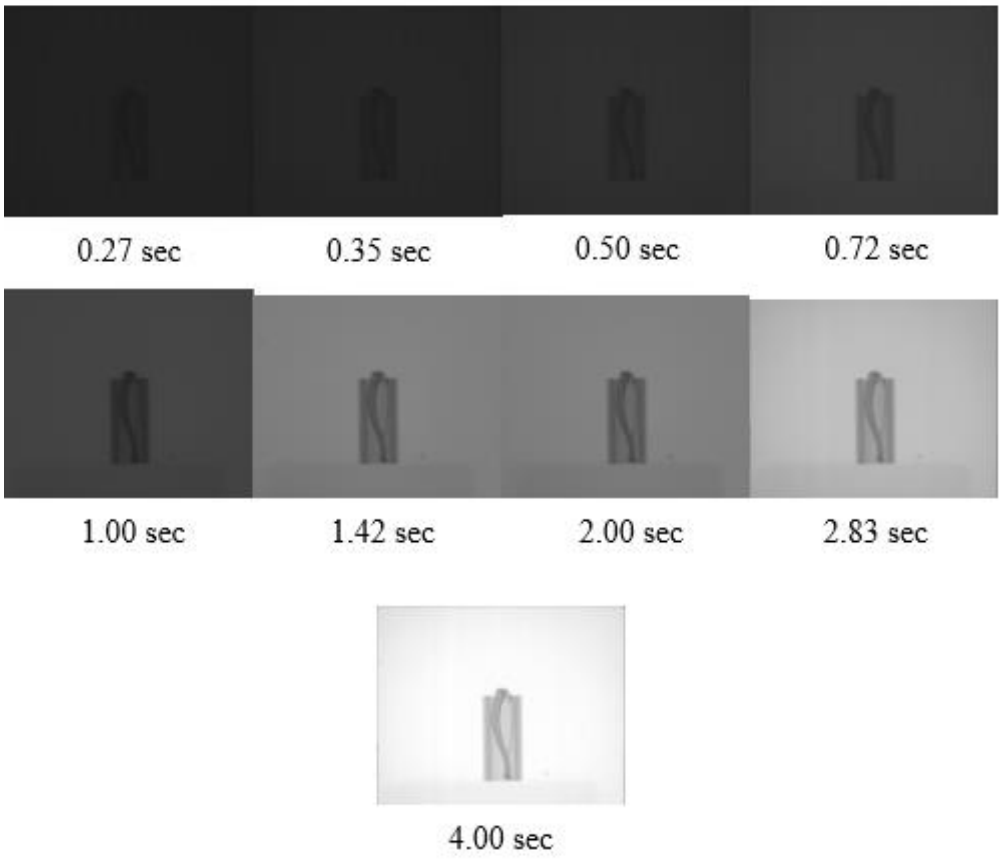

Figure 26: Typical radiographs that were acquired within the X-ray exposure time range of 0.27 sec-4.00 sec, X-ray current of 100 µA, X-ray tube voltage of 100 kV and FSD of 65 cm.

Figure 27 shows the correlation between the X-ray tube exposure time and image quality indicators before optimization. Figure 27 shows that the increase in exposure time results in the increase of image quality in terms of contrast and penetration.

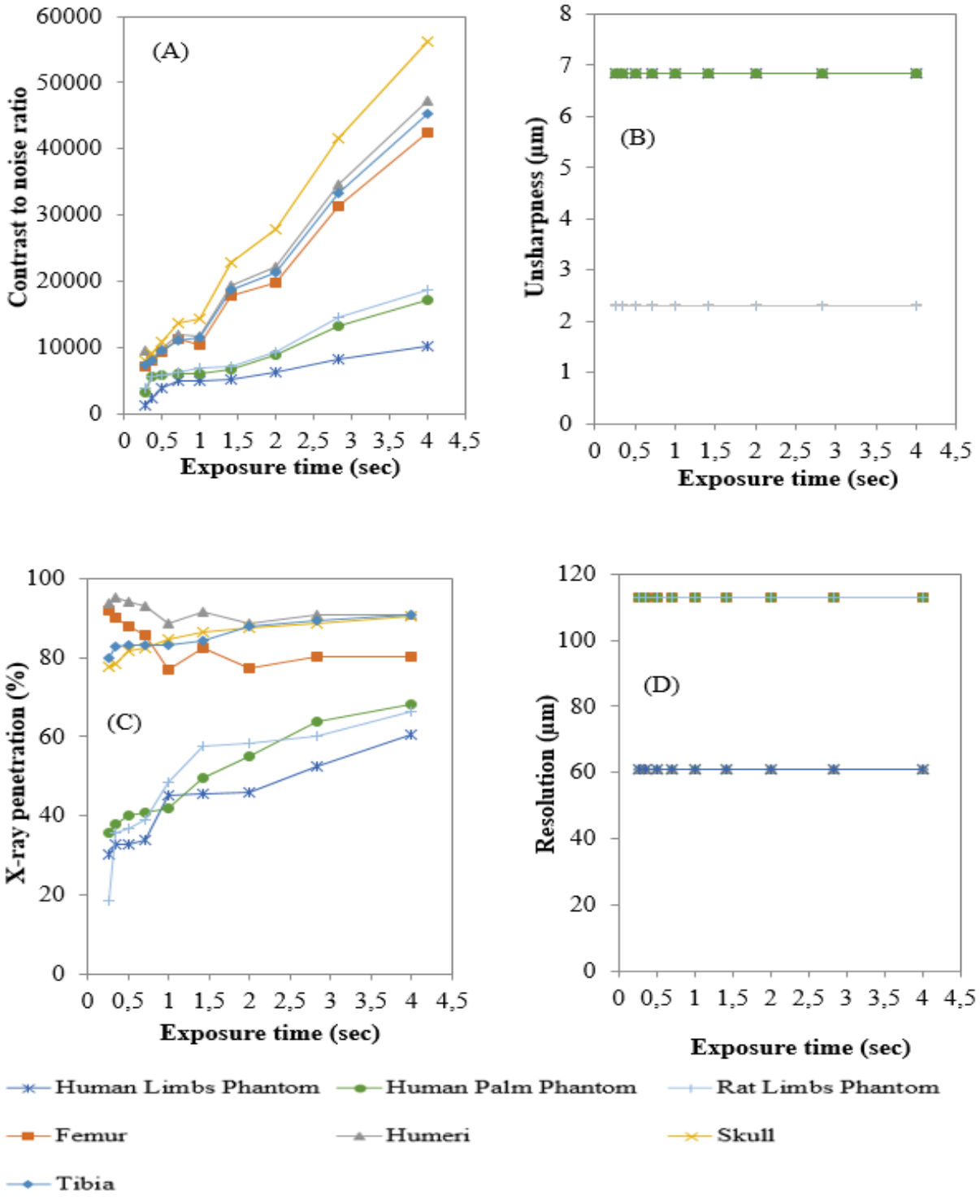

Figure 27: Illustration of the graphs of image quality indicators versus X-ray tube exposure time.

The unsharpness of the images of the phantoms and rat samples was constant at 2.31 µm and 6.86 µm, whereas the resolution of the images of the phantoms and rat samples was constant

at 113.04 µm and 60.87 µm respectively. The effect of X-ray exposure time on the measured initial radiation dose is shown in Figure 28. The initial radiation dose was measured at different position for phantoms and rat samples.

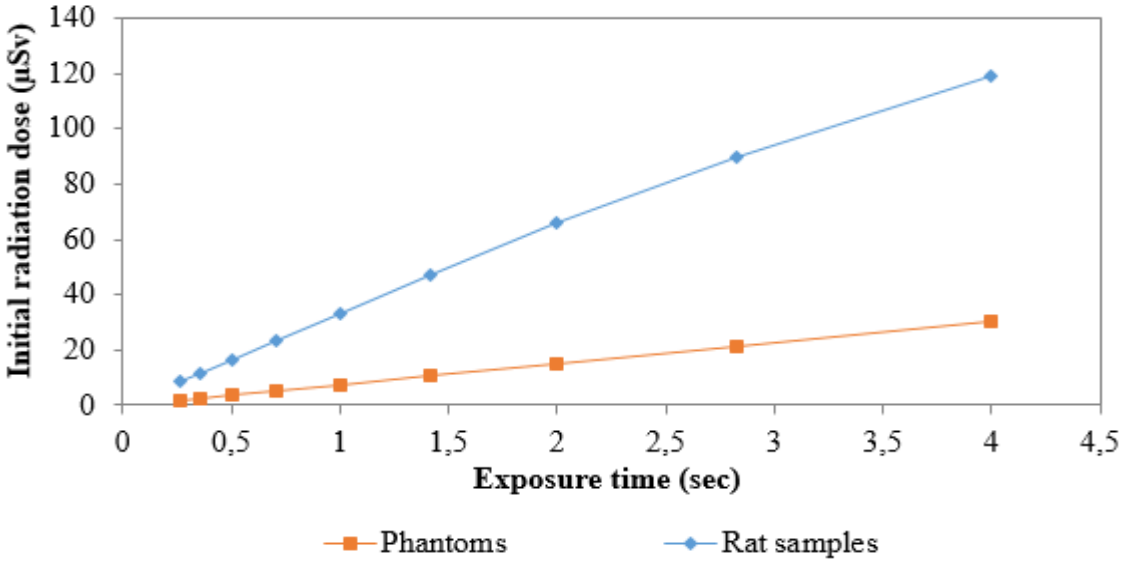

Figure 28: Initial radiation dose versus X-ray tube exposure time.

Figure 28 shows that the measured initial radiation dose of both the rat samples and phantoms increased rapidly with steep linear relationship as X-ray tube exposure time was increased. The initial radiation dose of the phantom was minimum compared to the initial radiation dose of the rat samples, the occurrence of this phenomenon is induced by the FSD. The FSD of the samples and phantoms was 65 cm and 73 cm hence there is a difference in the measured initial radiation dose between imaged subjects in Figure 28. The weight sum technique was used to analyse the effect of the X-ray tube exposure time on all the image quality objectives combined together with the initial radiation dose. The results are shown in figure 29.

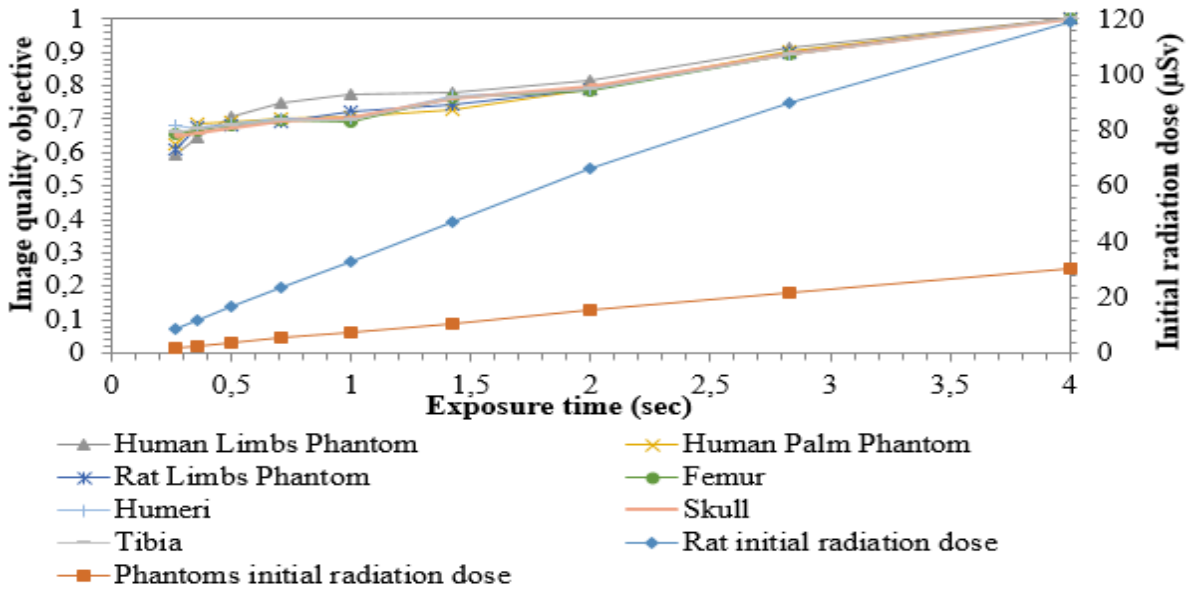

Figure 29: The image quality of the radiographs and the initial radiation dose of the rat samples and phantoms versus investigation of X-ray tube exposure time.

The results in figure 29 shows that the quality of the images of both the rat samples and phantoms was increasing when the X-ray tube exposure time was increased from 0.267 to 4.000 seconds. There is a linear relationship between the image quality objective, initial radiation dose and X-ray tube exposure time. Figure 29 shows that the image acquired at the X-ray tube exposure time of 4 secs is more optimal than other images. This is also observed in the radiograph in Figure 26, however, the selection of optimal image cannot be only based on the nature quality of that particular image. The health hazard that might be impinged on the subject exposed must be taken into account. Therefore, the image acquired with X-ray exposure time of 4 secs in Figure 26 can only be selected as the optimized image in X-ray radiography if it is acquired with the principle of ALARA. The X-ray exposure time quantifies the period at which a certain number of X-ray photons will produced and exposed to the subjects during image acquisition, thus the varying of the exposure time can affect the quality of the subject's image during X-ray examination.

The X-ray exposure time that balances the need for image quality while respecting the principle of ALARA was found by analyzing the results in figure 30.

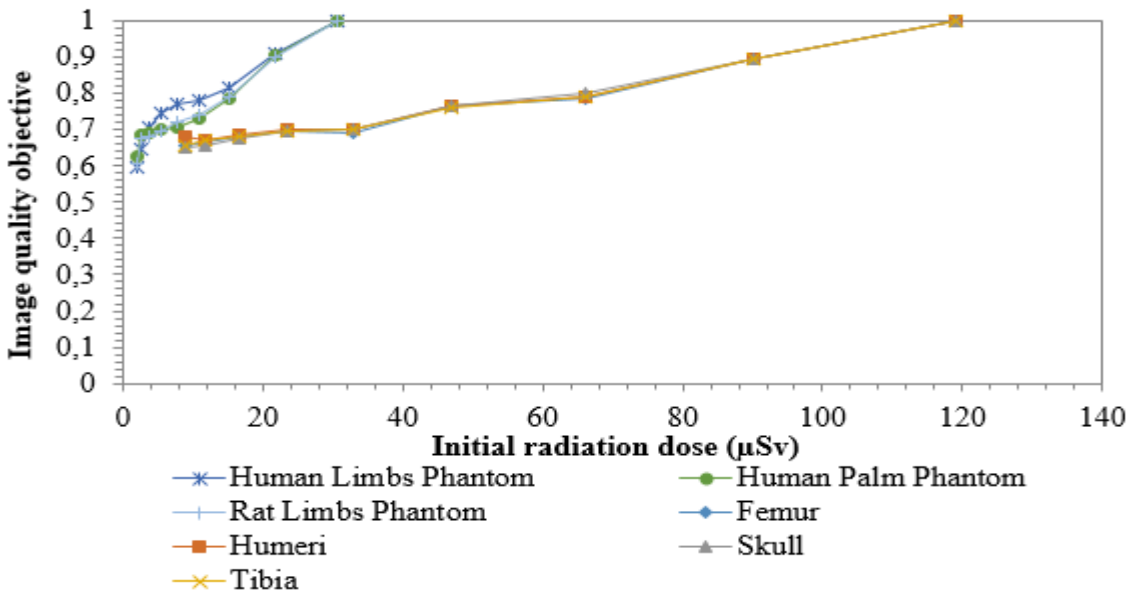

Figure 30: Image quality of the radiographs of the rat samples and phantoms versus initial radiation dose for X-ray tube exposure time investigation.

The most optimal images in Figure 30 were acquired between the initial radiation dose of 94.00 µSv and 132.00 µSv, this initial radiation dose correspond to X-ray exposure time between 2.83 seconds and 4 seconds in Figure 29. Figure 30 shows that the images that were obtained at the X-ray exposure time of 4 seconds are more optimal than the images that were acquired at lower X-ray tube exposure time for both phantoms and samples. The initial radiation dose of 31.00 µSv (0.03 mSv) and 132.00 µSv (0.13 mSv) was for the phantoms and rat samples when the maximum quality images were acquired at the X-ray exposure time of 4 seconds. At the X-ray exposure time of 2.83 seconds, the initial radiation dose of both the phantoms and rat samples was 22.00 µSv (0.02 mSv) and 90.00 µSv (0.09 mSv). The images that were acquired at the X-ray tube exposure time of 2.83 seconds are indicated in Figure 26.

The radiation reference level less than 100 µSv (0.1 mSv) is specified by the American college of radiology practice., (2010) for X-ray examinations of the hand, thumb, knee and the wrist. According to the findings of this thesis, the acquisition of optimized bone radiographs can be achieved by using the X-ray exposure time of 2.83 seconds, X-ray voltage and current of 100 kV and 100 µA, FSD of 65 cm with no X-ray filter. In this regard, the resultant initial radiation dose, which was 22.00 µSv (0.02 mSv) and 90.00 µSv (0.09 mSv) for both phantoms and

samples at the exposure time of 2.83 seconds, will be consistent with the dose limit set by American college of radiology practice., (2010).

4.2. The optimization of focal-sample distance on image quality indicators and initial radiation dose

The distance between the focal spot and the detector of the micro-focus X-ray machine that was used in this study is $115\ cm$, the evaluation of image quality and radiation exposure was achieved through varying the sample-detector distance (SDD). The main goal of varying the SDD in this study was to understand the effect of this parameter on image quality and initial radiation dose. Figure 31 shows some of the typical images that were acquired as the distance between the sample stage and the X-ray source was increased, thus increasing the FSD.

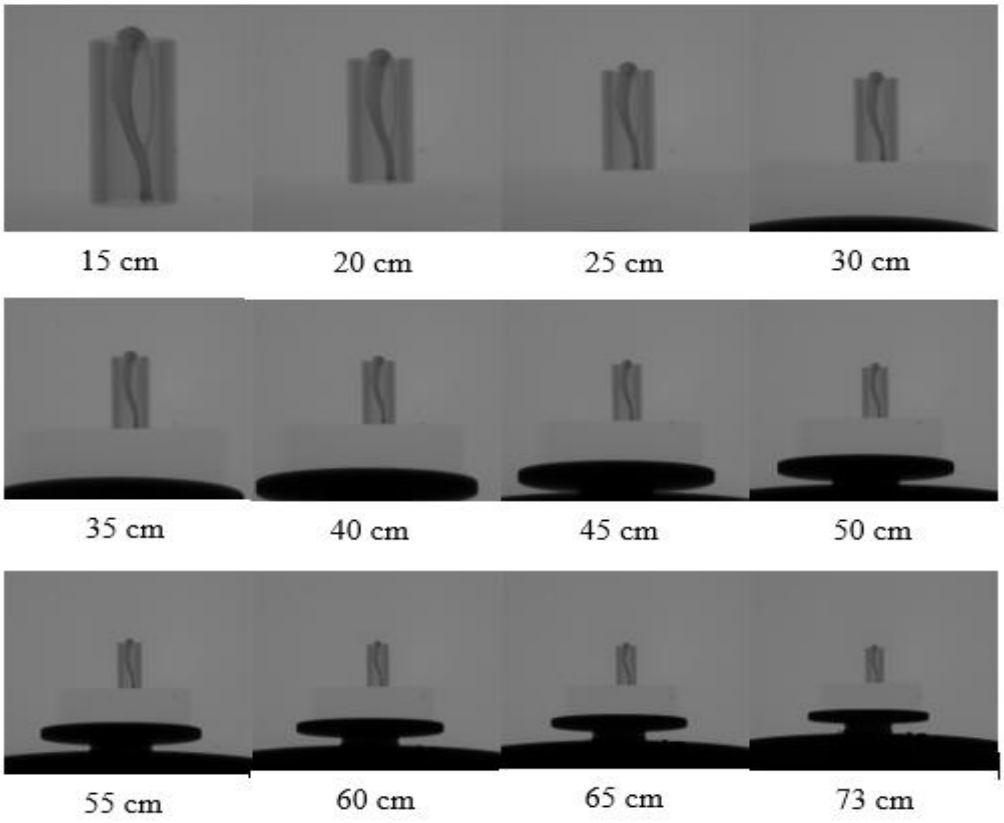

Figure 31: Typical radiographs that were acquired with the FSD range of 15 cm -73 cm, X-ray current of 100 µA, X-ray tube voltage of 100 kV and X-ray exposure time of 1 sec.

The images in Figure 31 were acquired within the FSD range of 15 cm-73 cm. Due to magnification; the small details of the projected information (tibia) in Figure 31 were becoming more distinguishable and visible, as the sample was closer to the source and away from the

detector. The effect of varying the FSD on the individual image quality indicators (Unsharpness, resolution, Contrast to noise ratio (CNR) and X-ray penetration) is shown in Figure 32.

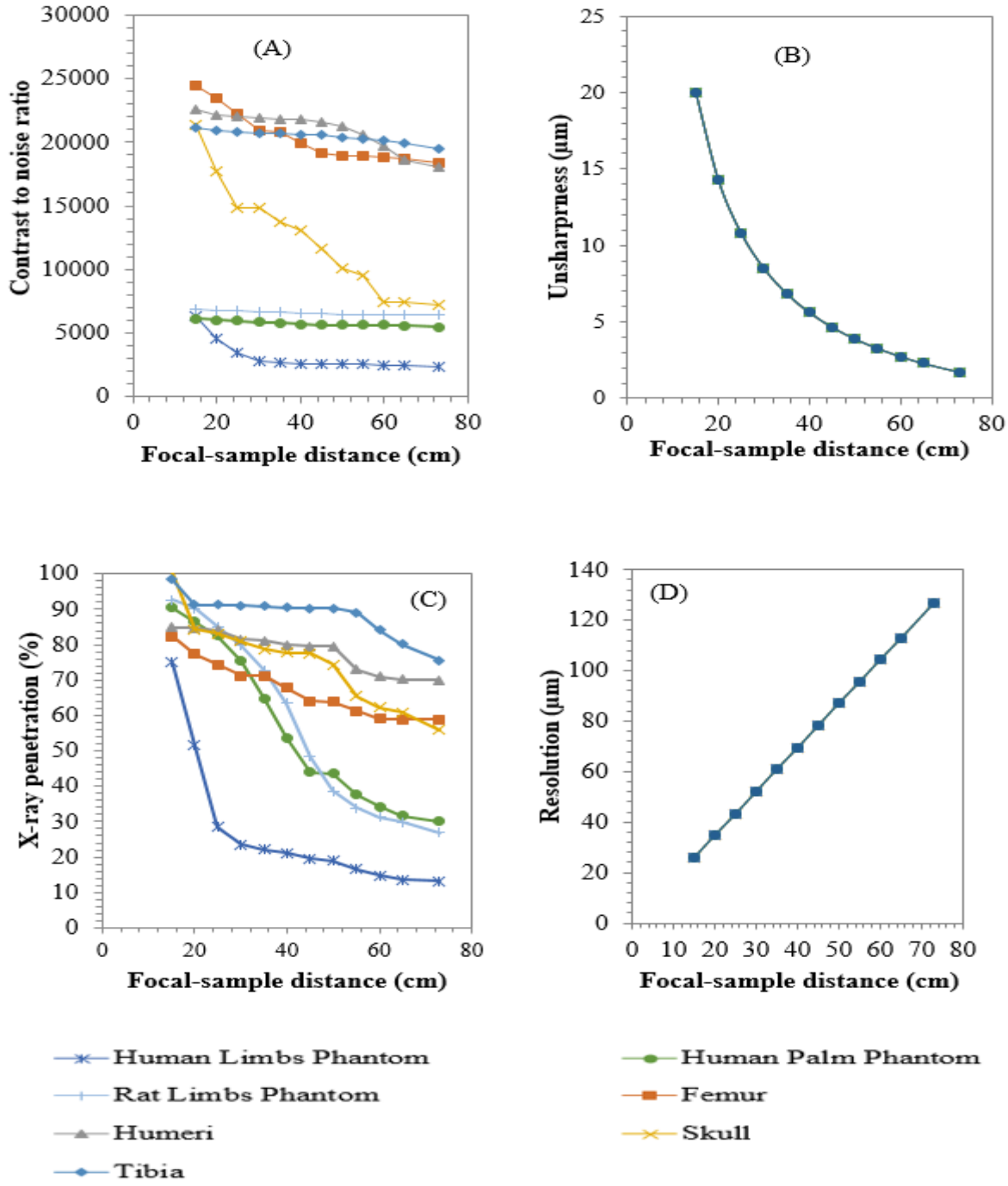

Figure 32: Illustration of the graphs of image quality indicators versus Focal-sample distance.

Figure 32 shows clearly that the unsharpness in the images diminished when the sample moves away from the X-ray source. However, the resolution in the image deteriorates as well, high

values of resolution means the image quality is poor. The images of the samples and phantoms were magnified as they were brought closer to the X-ray source as seen in the radiographs of figure 31. There are no major changes in the contrast to noise ratio and penetration throughout the change in FSD. The relationship between the initial radiation dose and FSD for both phantoms and rat samples in indicated in Figure 33.

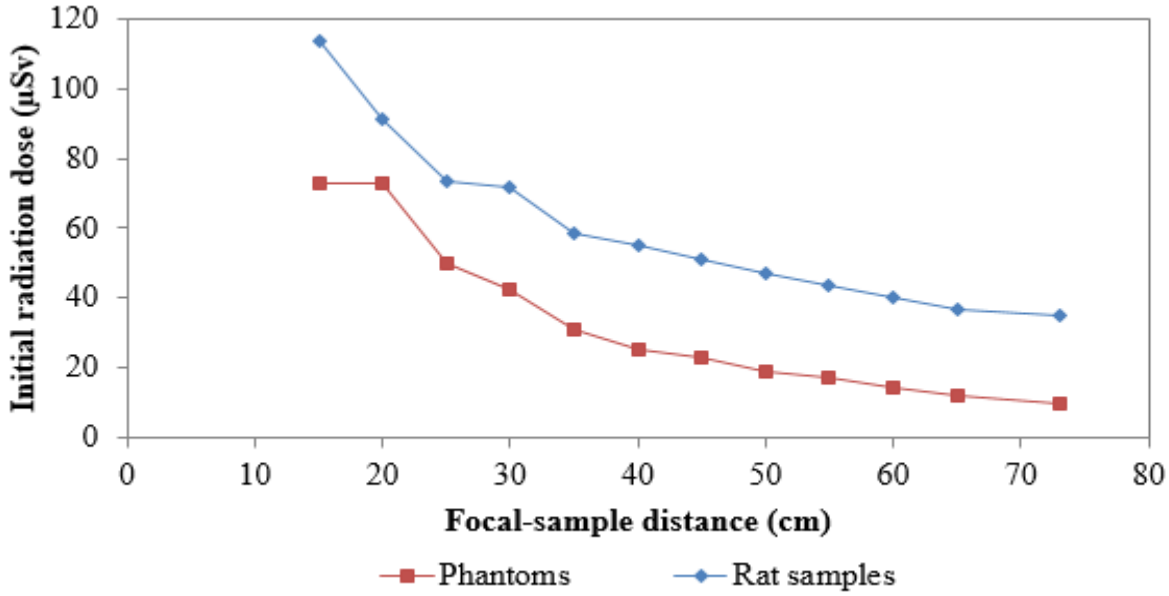

Figure 33: Initial radiation dose versus focal-sample distance.

Figure 33 shows that the initial radiation dose decreased as the samples and the phantoms were moved away from the X-ray source. This phenomenon can be sustained by the inverse square law of radiation, which states that the radiation intensity passing through the area of the object/sample decreases as the square of the distance of that object's area from the X-ray source increases (Whaites & Cawson, 2002).

The results of image quality indicators in relation to the FSD were used to calculate the overall image quality objective through the weight sum technique as outlined previously in chapter 3. The overall image quality objective was related to the measured initial radiation dose while the FSD was varied, this relationship is illustrated in Figure 34, in which X-axis is the varying values of the FSD, image quality objective and initial radiation dose were plotted in the primary and secondary Y-axis.

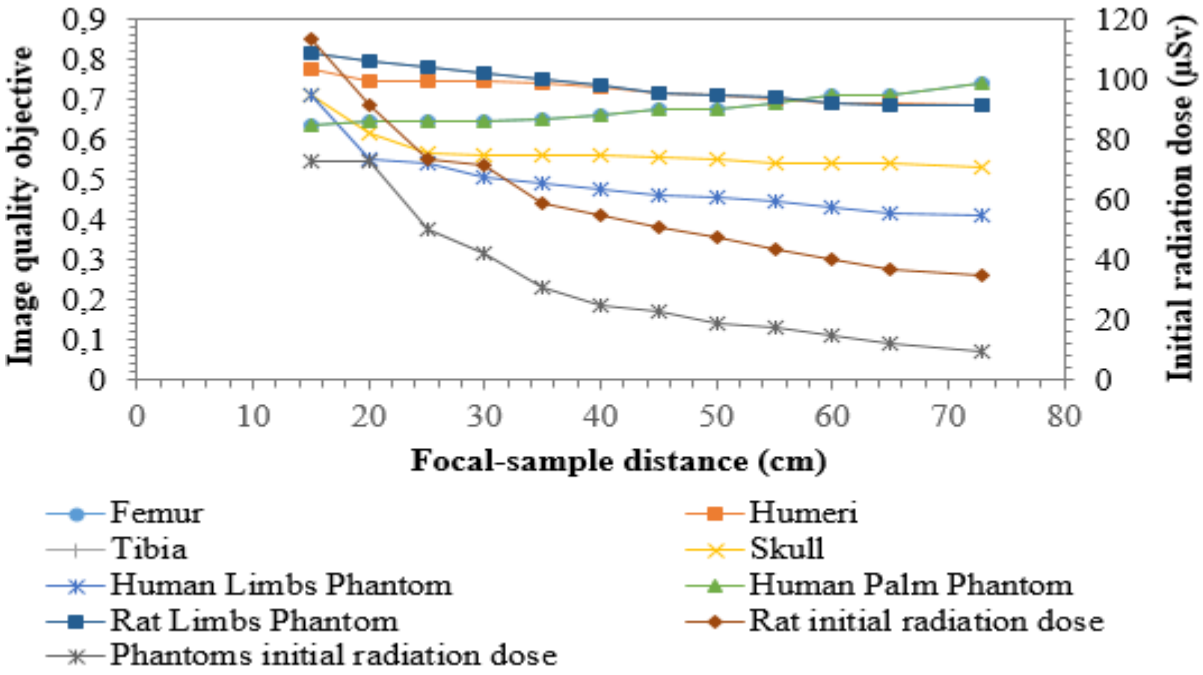

Figure 34: The image quality objective and the initial radiation dose of the rat samples and phantoms versus the investigation of focal-sample distance.

Figure 34 shows that there is no significant change in image quality objective when the sample is moved away from the X-ray source. However, there is a significant reduction in initial radiation dose. There is no clear conflict between these two objectives (image quality and initial radiation dose) as the FSD changes. Therefore, in order to achieve optimization of X-ray radiography through the ALARA principle, low image unsharpness is desired with low initial radiation dose. According to observations made in Figure 33 and Figure 34, high FSD yields low initial radiation dose and low image unsharpness. Therefore, to reduce image unsharpness and the radiation dose, the sample must be positioned away from the X-ray source and brought closer to the detector. Figure 35 shows that the image quality objective remain constant from most of the values of the FSD range as the initial radiation dose increased for both phantoms and rat samples.

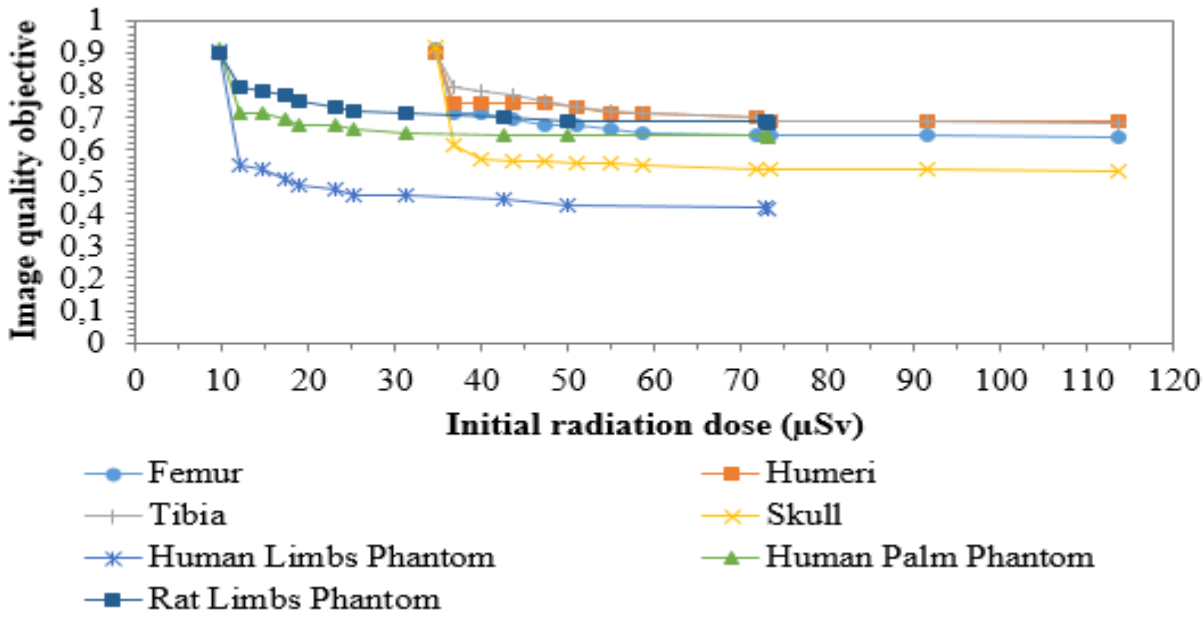

Figure 35: Image quality of the radiographs of the rat samples and phantoms versus initial radiation dose for focal-sample distance investigation.

The maximum image quality for both phantoms and samples occurred at the lowest initial radiation dose, this phenomenon corresponds to the maximum FSD (73 cm) that was investigated in Figure 34. The specification stated in the report compiled by Busch et al., (2004), suggested that in conventional X-ray radiography, the images of the shoulders, upper arm and lower leg should be obtained with the distance of 100 cm to 150 cm between the patient and the X-ray source. This report further states that this FSD must be used with X-ray tube voltage that is in between 60 kV and 75 kV, the X-ray exposure time less than 100 ms and aluminium X-ray filter greater than 2.5 mm. In this study, no X-ray filtration was used when the X-ray tube greater than 75 kV was used to acquire the images with the FSD that is less than 150 cm. However, the radiation reference level less than 100 µSv (0.1 mSv) was specified by the report compiled by Dianna et al., (2018) for X-ray examinations of the human limbs. The measured initial radiation dose in this study was less than this radiation reference level at the highest FSD that was investigated (73 cm) and the image quality of most of the phantoms and the rat samples was optimal at this FSD.

4.3. The optimization of thicknesses of X-ray filters on image quality indicators and initial radiation dose

The results of the effect of varying the thicknesses of X-ray filters are established below. The weight sum technique was applied to these results for optimization and the image quality objective was calculated. The results of the image quality objective presented herein were related to the measured initial radiation dose. Image quality objective was not evaluated for the thicknesses of the X-ray filters that did not form any images.

4.3.1. Optimization of the thickness of copper X-ray filter

The images of the rat tibia in Figure 36 were acquired using different thickness of X-ray filter made of copper. The brightness of the radiographs in figure 36 diminished as the thickness of copper filter was increased.

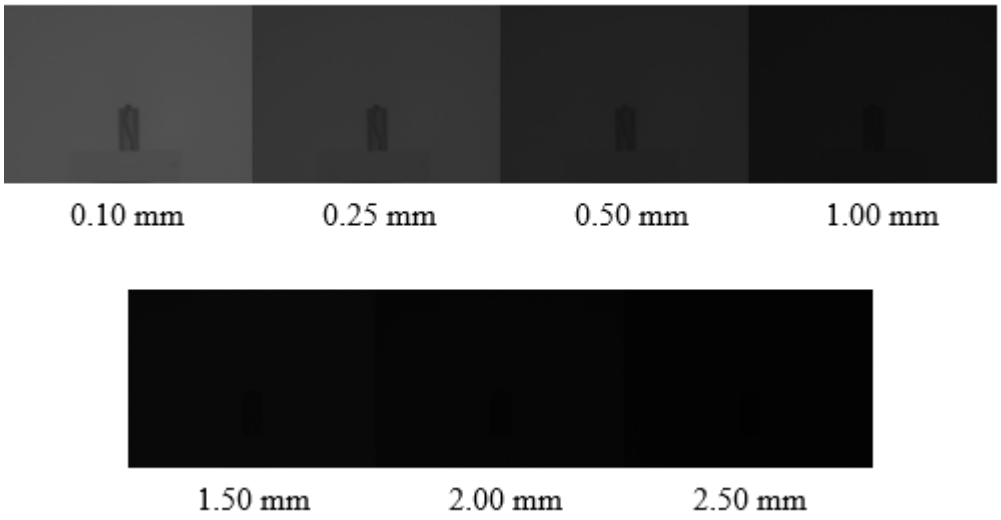

Figure 36: Typical radiographs that were acquired within the copper filter thickness range of 0.1 mm – 2.5 mm, X-ray current of 100 µA, X-ray tube voltage of 100 kV, FSD of 65 cm and X-ray exposure time of 1 sec.

The illustration of the effect of the different thicknesses of copper filtration on image quality indicators is further illustrated in form of graphs in Figure 37. Figure 37 shows that the contrast to noise ratio and X-ray penetration decreased as the thickness of copper filtration was increased. Figure 37 (A) shows that contrast to noise ratio and X-ray penetration of the humeri,

tibia and femur samples were higher than that of the phantoms throughout the increase in the thickness of copper filtration

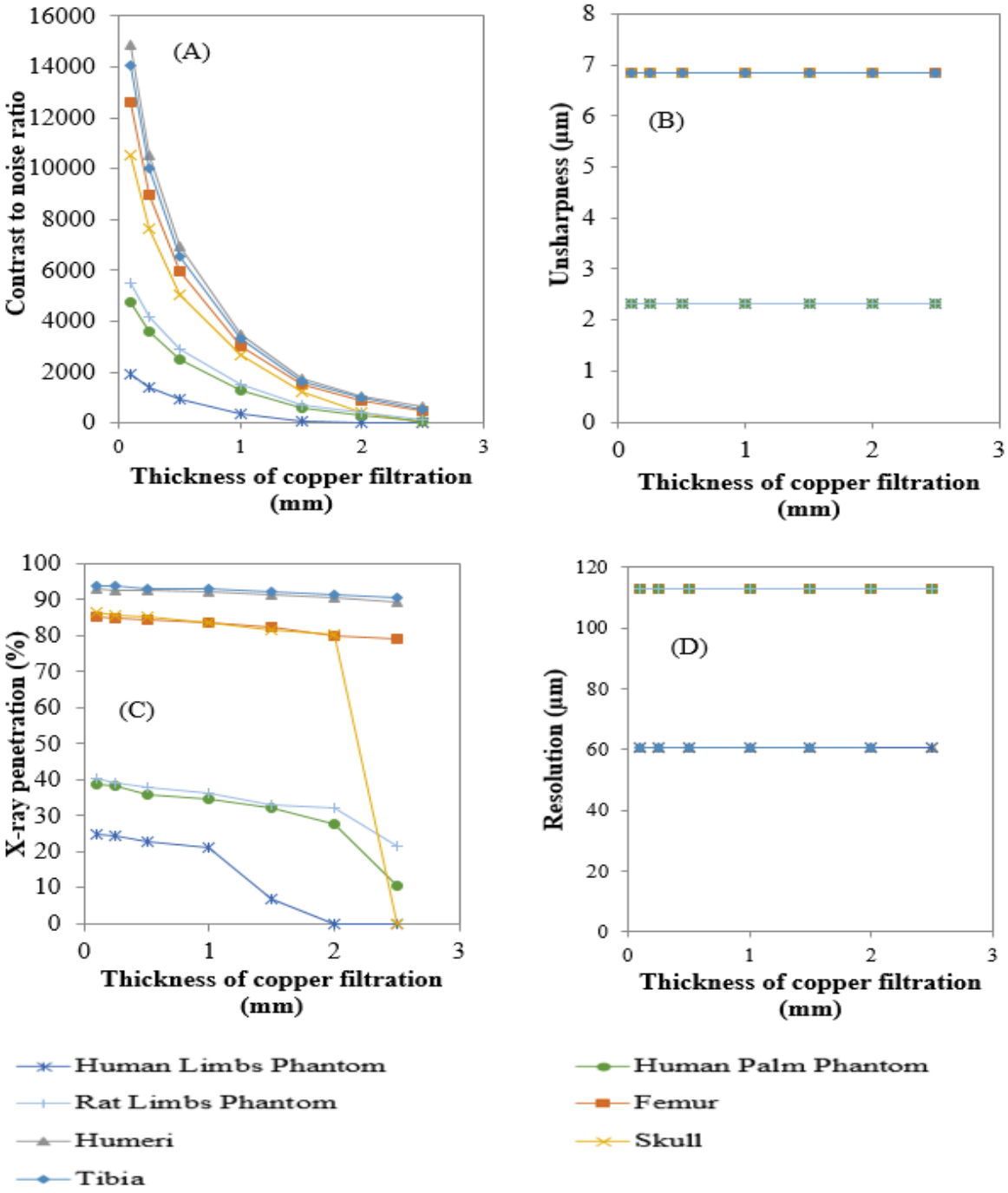

Figure 37: Illustration of the graphs of image quality indicators versus different thicknesses of copper X-ray filtration.

The human limbs phantom was not penetrated by X-ray radiation at copper thickness of 2 mm, whereas the rat skull also had no penetration at 2.5 mm in Figure 37 (C). This phenomenon led

to these two subjects to have zero contrast to noise ratio for copper thickness of 2 mm and 2.5 mm respectively. The image quality at the thickness of 0.10 mm was far better than the image at 2.5 mm. Increasing the thickness of copper X-ray filter reduces the visibility of the projected information as shown in Figure 36, the distinguishability of this information from the background reduces as the thickness increases. Small thicknesses of copper filtration produce better image quality than big thicknesses as indicated in Figure 36, the image quality is very poor above the thickness of 0.5 mm. Figure 36 also shows that the brightness of the image diminished rapidly from 0.5 mm to 2.50 mm. A quadratic decrease between initial radiation dose and thicknesses of copper X-ray filtration is observed in Figure 38.

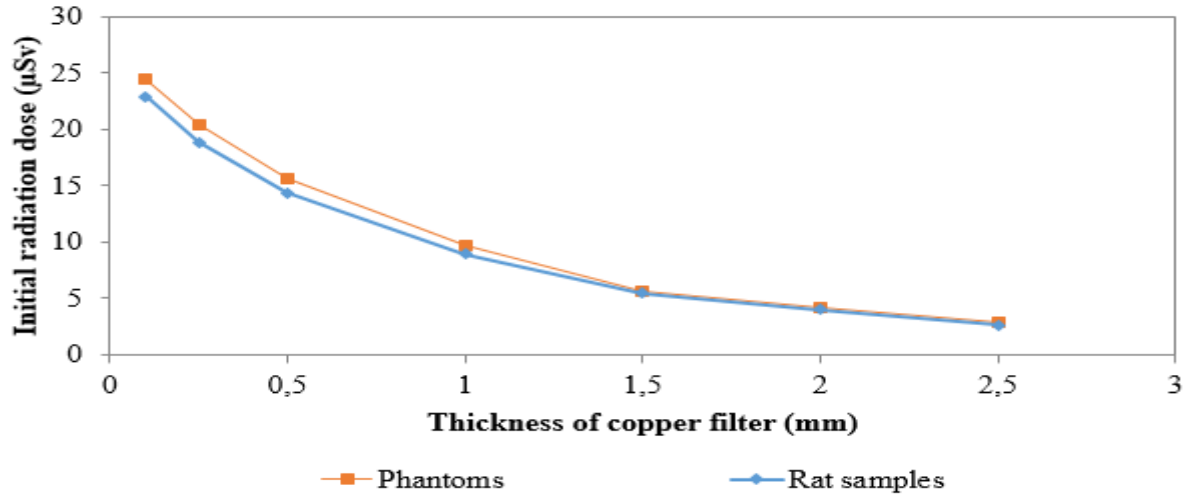

Figure 38: Initial radiation dose versus different thicknesses of copper X-ray filtration.

The quality of the images deteriorated, and the measured initial radiation dose decrease for both the rat samples and phantoms as the thickness of the copper was increased from 0.1 mm to 2.5 mm as shown in Figure 39. The high quality images were acquired at the copper thickness of 0.1 mm whereas the low quality images were acquired with the thickness of 2.5 mm in Figure 39.

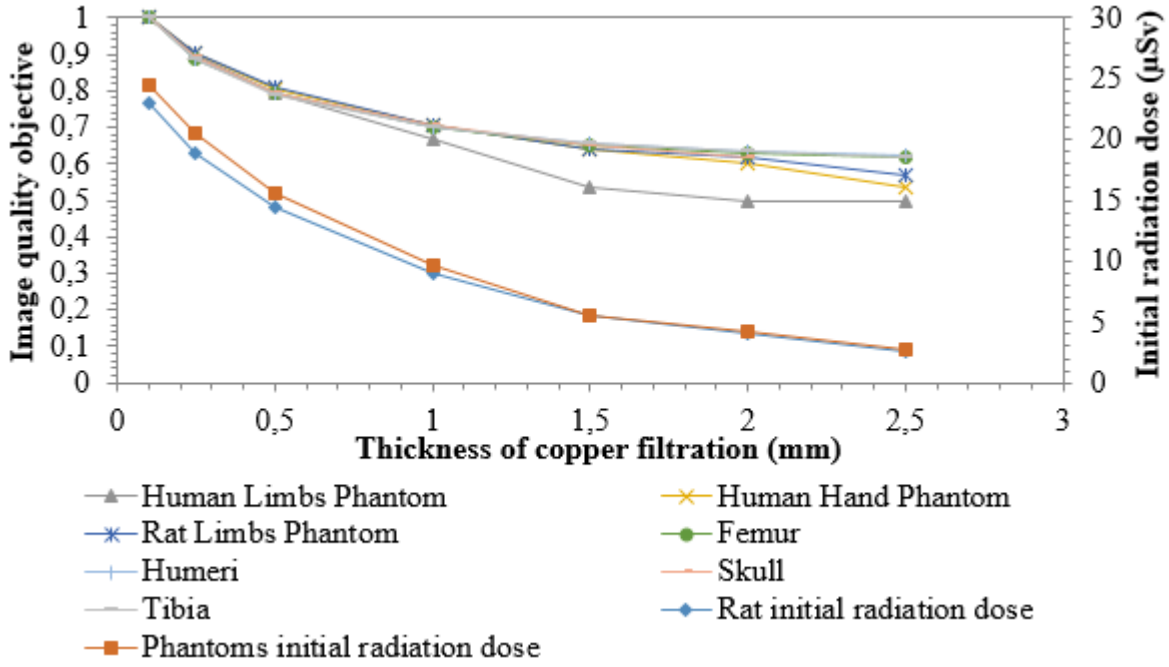

Figure 39: The image quality of the radiographs and initial radiation dose of rat samples and phantoms versus different thicknesses of copper X-ray filter.

The quality of all the radiographs of both the phantoms and rat samples were minimal at the highest thickness of copper filter. The initial radiation dose also decreased as the thickness of copper filtration was increased from 0.1 mm to 2.5 mm. The highest amount of initial radiation dose was measured at the smallest thickness that was investigated (0.1 mm), whereas the low initial radiation dose occurred at the highest thickness of copper that was investigated (2.5 mm). The difference in initial radiation dose between the phantoms and rat samples in this study is mainly due to the positioning of these materials from the X-ray tube, rat samples were positioned at the FSD of 65 cm and the phantoms were at 73 cm. There is a need to balance the quality of the image and the radiation dose when X-ray filtration is used. The graphs in Figure 40 provide information that can be used by a decision maker to decide on the best thickness of the X-ray filter to use.

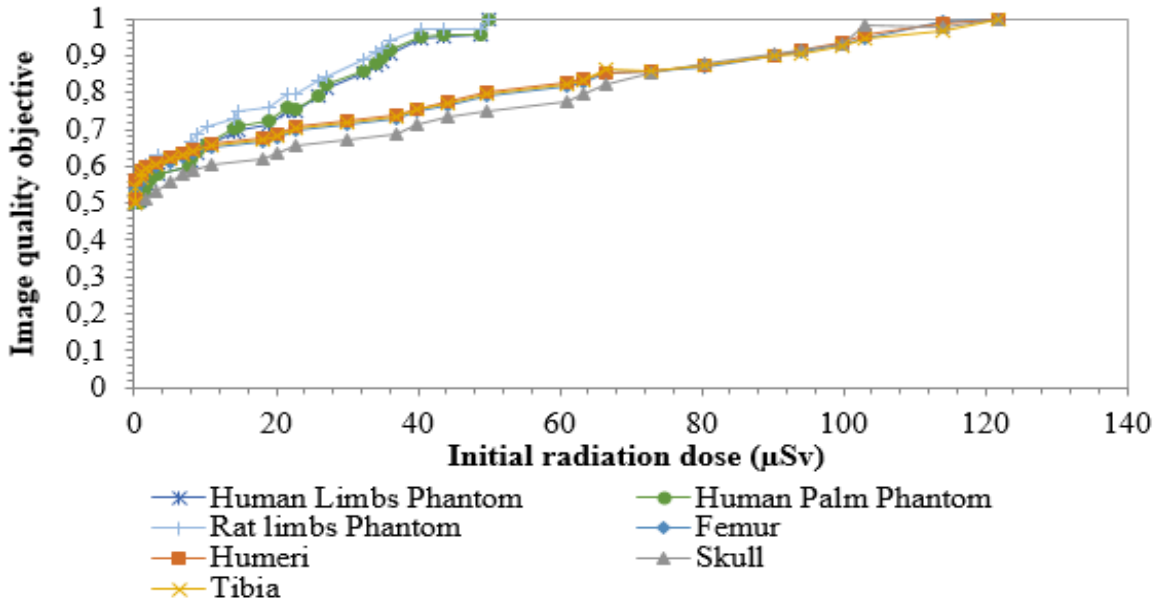

Figure 40: Image quality of the radiographs of the rat samples and phantoms versus initial radiation dose for investigation of different thicknesses of copper filtration.

Figure 40 shows that high thicknesses of copper filters are good absorbers of low energy X-ray energy but they contribute to poor image quality formation as observed in the radiographs in Figure 36. Small thicknesses of copper filtration result in high quality images with high initial radiation dose.

The study conducted by Zainon et al., (2014) and Ernest et al., (2014) suggested that 0.2 mm and 0.3 mm thicknesses of copper filters with X-ray voltage of 100 kVp and 120 kVp is appropriate for optimization in X-ray radiography. In this study, the copper thickness investigation was performed with X-ray tube voltage of 100 kV, X-ray tube current of 100 µA, X-ray exposure time of 1 second and FSD of 65 cm. The maximum quality radiographs were acquired at the copper thickness of 0.1 mm with initial radiation dose range of 22.92 µSv (0.023 mSv) – 24.53 µSv (0.025 mSv).

According to the suggestions of American college of radiology practice., (2010) on appropriates criteria, the radiation dose of 24.53 µSv (0.025 mSv) is less than the radiation reference level (0.1 mSv) which is recommended for acquisition of the radiographs of the human limbs. The copper thickness of 0.1 mm with X-ray tube voltage of 100 kV, X-ray tube current of 100 µA, X-ray exposure time of 1 seconds and FSD of 65 cm, is therefore justified

for acquisition of optimized radiographs with minimized initial radiation dose that will not impinge on the health of the patient.

The high quality images were acquired at the copper thickness of 0.1 mm whereas the low quality images were acquired with the thickness of 2.5 mm in Figure 39. The quality of all the radiographs of both the phantoms and rat samples were minimal at the highest thickness of copper filter. Figure 39 shows that the small variation of image quality was observed between the images of some of the rat samples and phantoms at the copper thickness greater than 1 mm, this could mean that some of the high-energy photons that initially contributed to image quality formation at the thickness less than 1 mm were highly attenuated at higher thicknesses. The qualities of the acquired images were equally optimal at the thickness of 0.1 mm in Figure 39, this means that the phantoms used in this study behaved similarly as actual samples at this copper thickness.

The initial radiation dose also decreased as the thickness of copper filtration was increased from 0.1 mm to 2.5 mm. The highest amount of initial radiation dose was measured at the smallest thickness that was investigated (0.1 mm), whereas the low initial radiation dose occurred at the highest thickness of copper that was investigated (2.5 mm). The initial radiation dose of the phantoms was slightly higher than that of the samples between thicknesses of 0.1 mm and 1 mm as indicated in Figure 39. In some cases, this may due to high atomic number material in bone tissues (Calcium-20) absorbing more radiation than low atomic number material in the designed phantoms (Aluminium-13). High atomic number materials are also considered to be heavier or denser than low atomic materials, therefore these materials resist radiation penetration better mainly because of the greater absorption radiation energy. However, the difference in initial radiation dose between the phantoms and rat samples in this study is mainly due to the positioning of these materials from the X-ray tube, rat samples were positioned at the FSD of 65 cm and the phantoms were at 73 cm. The variations in initial radiation dose in Figure 39, might also be due to the absorption of the same amount of low energy X-ray energy photons by a certain thickness of copper filtration during the recording of the dose of phantoms and rat samples.

4.3.2. Optimization of the thickness of silver X-ray filter

The images in Figure 41 were acquired with the variation of silver X-ray filtration, while other X-ray scanning parameters were kept constant, Figure 41 shows that little brightness occurred in the image that was acquired at the thickness of 0.125 mm, but this image cannot be considered for diagnosis because its details were very obscure. The images that were acquired above this silver metal thickness (0.25 mm – 1.00 mm) were very dark and projected information were not visible at all.

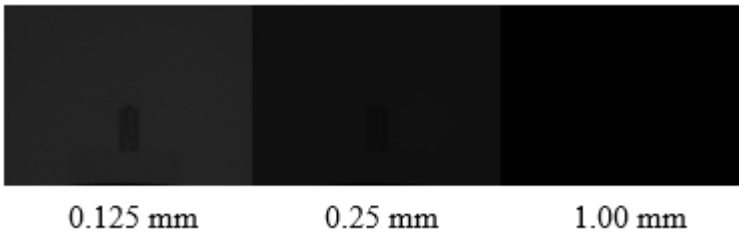

Figure 41: Typical radiographs that were acquired within the silver filter thickness of 0.125 mm to 1.000 mm, X-ray current of 100 µA, X-ray tube voltage of 100 kV, FSD of 65 cm and X-ray exposure time of 1 sec.

At equal thickness of 0.25 mm of copper and silver filtration, the image that was acquired with copper filtration in Figure 36 appeared to be of better image quality that the image that was acquired with silver filtration in Figure 41. This is entirely due to the efficiency of this metals to absorb low energy photons, silver metal with atomic number of 47 absorbs more photons than copper metal with an atomic number of 29. However, at the thickness 1.00 mm, these two filters produced images of poor quality in Figure 36 and 41. These images are very dark and no information of the imaged sample can be seen. This could actually insinuate that at bigger thicknesses there two filters absorb large amount of X-ray photons that could actually contribute to the formation of better image quality. The effect of silver filtration on the individual image quality indicators is illustrated in Figure 42.

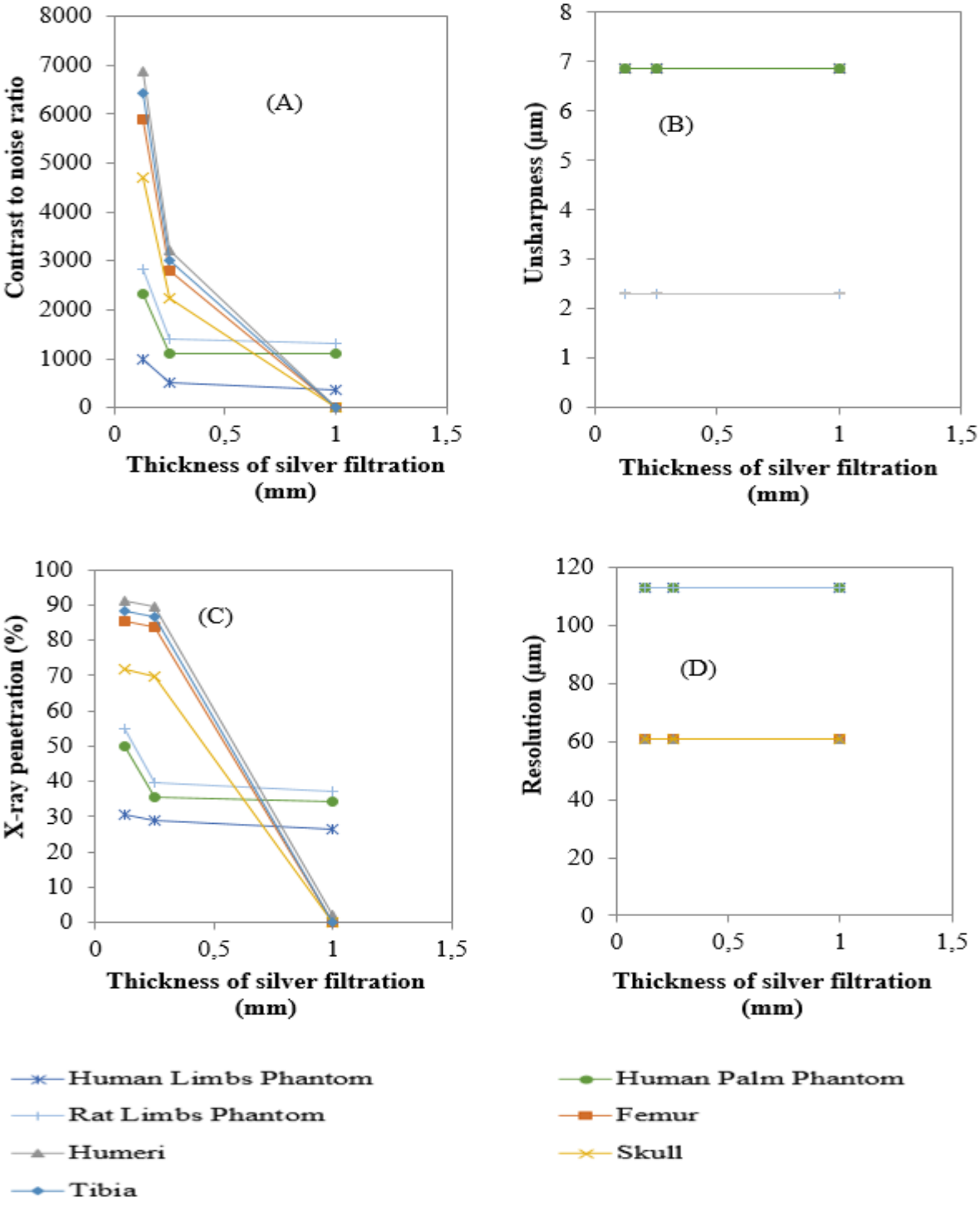

Figure 42: Illustration of the graphs of image quality indicators versus different thicknesses of silver X-ray filtration.

Figure 42 (A) and Figure 42 (C) indicate that both the contrast to noise ratio and X-ray penetration decreased sharply as the thickness of silver filtration was increased. Furthermore, Figure 42 (A) and Figure 42 (C) shows that at the silver thickness of 1.00 mm, there was no X-

ray penetration of the rat samples, hence this subject had zero contrast to noise ratio at this silver metal thickness. The thickness of 1.00 mm was highest silver thickness that was investigated and high quantity of low energy photons was filtered at this thickness. The remained X-ray photons after filtration with the silver thickness of 1.00 mm yielded the limited number of X-ray photons with insufficient energy to induce penetrate in rat samples. However, the phantoms were penetrated by the X-ray photons at the silver thickness of 1.00 mm, for instance the phantom simulating the human limbs had the X-ray penetration of 26.35% and the contrast to noise ratio of 366.90 at this silver thickness.

The image unsharpness and resolution of the phantoms and rat samples was constant throughout the increase in the thickness of silver filtration in Figure 42 (B) and Figure 42 (D). These two subjects were not moved during the acquisition of images, the rat samples were positioned at the FSD of 65 cm and the phantoms were at the distance 73 cm from the X-ray source. The image unsharpness of the phantoms and samples was constant at 2.31 µm and 6.86 µm, whereas the resolution was also constant at 113.04 µm and 60.87 µm. Contrary to the rat samples, the phantoms had low unsharpness and high resolution because they were positioned a bit further from the X-ray source during the image acquisitions are indicated in Figure 41. This X-ray filtration proved to be bad for image quality optimization in this study, because all the images that were acquired with the thicknesses of this filter were of poor quality. A decrease in the measured initial radiation dose as the thickness of silver filtration increases is observed in Figure 43.

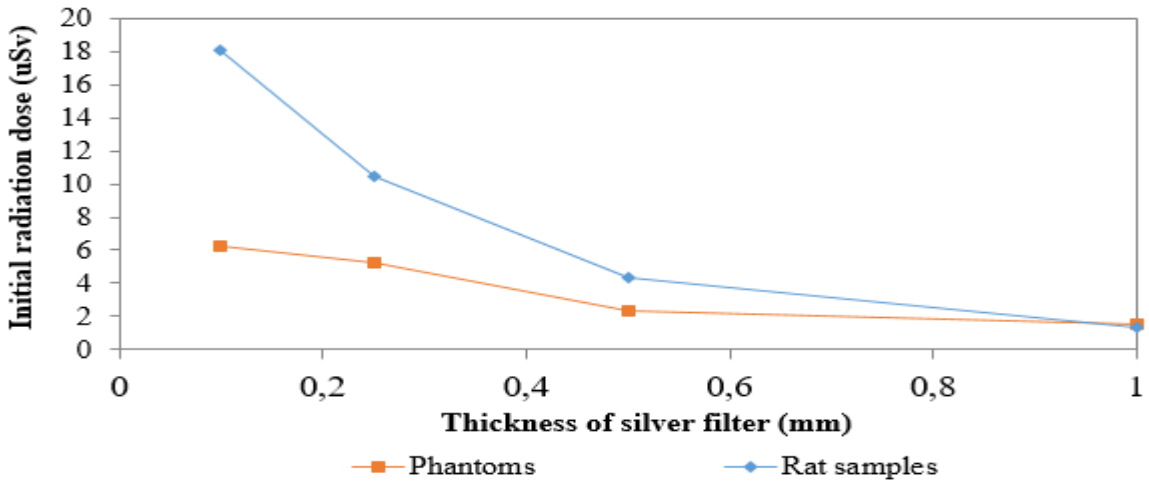

Figure 43: Initial radiation dose versus different thicknesses of silver X-ray filtration.

Rat samples were positioned closer to the X-ray source at the FSD of 65 cm whereas the FSD of the phantoms was 73 cm. The inverse square law state that radiation intensity from the X-ray source decreases as the FSD of the subject is increased, hence the phantoms had the minimum initial radiation dose compared to rat samples throughout the increase of the thickness of silver filtration.

The quality of the images of the rat samples and phantoms decreased gradually as the thickness of the silver thickness was increased from 0.125 mm to 1 mm. The image quality was equally maximum at the silver thickness of 0.125 mm in Figure 42, and 1 mm thickness yielded different low quality images amongst the samples and phantoms used in this study. The image quality parameters were combined under a single image quality objective by applying the weight sum technique. The effect of silver filtration on the image quality objectives and the radiation dose are shown in figure 43.

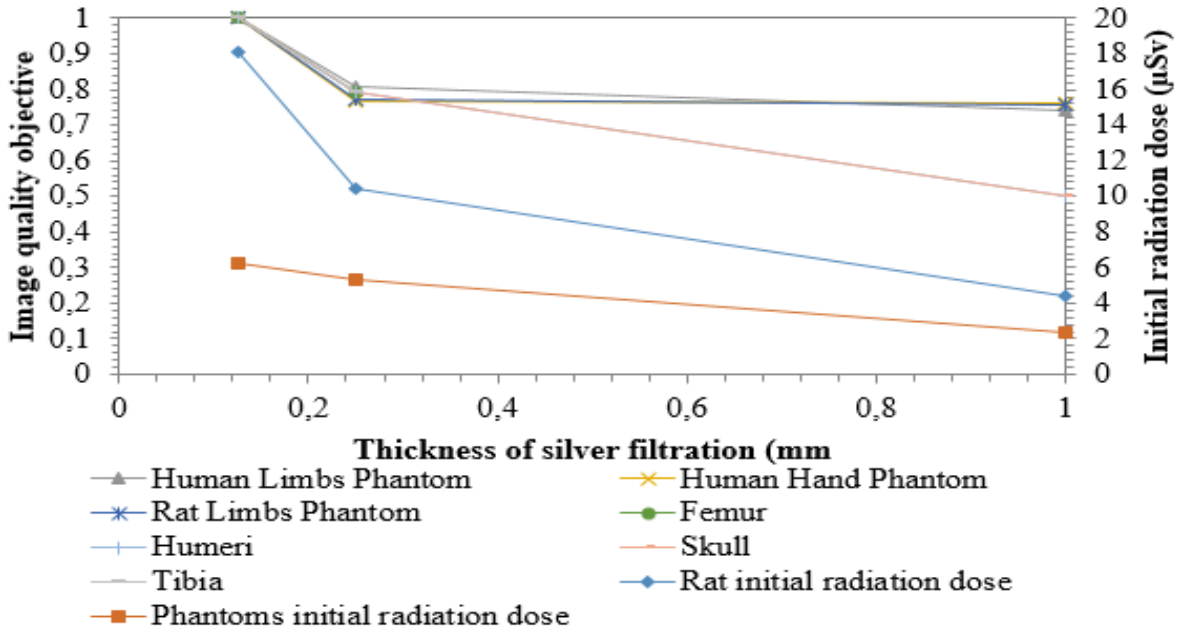

Figure 43: The image quality of the radiographs and initial radiation dose of the rat samples and phantoms versus different thicknesses of silver X-ray filter.

Figure 43 shows that the image quality for all the sample diminished as the thickness of the silver filter was increased. The initial radiation dose decreases with the increase in thickness of silver filter. The difference in the measured initial radiation dose between phantoms and rat samples is due to the FSD of these materials during the experiment, the FSD of the samples

was 65 cm and that of the phantoms was 73 cm. All the radiographs obtained during the investigation of silver metal thickness investigation were of poor quality when compared to the radiographs acquired during the investigation of copper thickness The thickness of copper is the preferred filter for absorbing lower energy photons in most of the diagnostic X-ray beams (Zainon, et al., 2014).

4.3.3. Optimization of the thickness of aluminium X-ray filter

During the varying of the thickness of aluminium X-ray filter, the images of the rat tibia in Figure 45 were acquired.

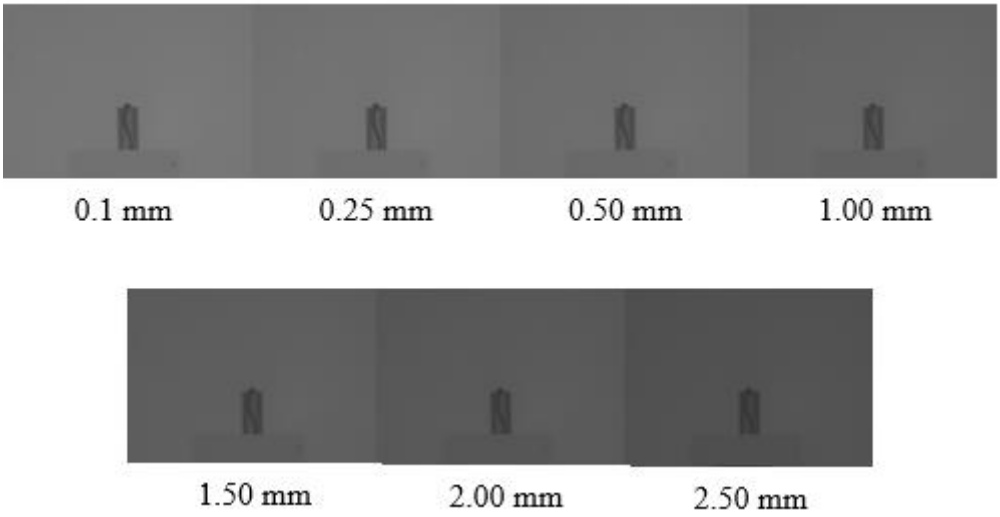

Figure 45: Typical radiographs that were acquired within the aluminium filter thickness range of 0.1 mm – 2.50 mm, X-ray current of 100 µA, X-ray tube voltage of 100 kV, FSD 65 cm and X-ray exposure time of 1 sec.

Aluminium has the atomic number of 13, hence the images that were acquired with this filter are of brighter than both copper and silver filtration in Figure 36 and 41. Equal thicknesses of aluminium and copper filtration were investigated, but aluminium metal produced better brightness across all the thicknesses. Unlike high atomic number filters, low atomic number filters absorb the limited number of X-ray photons, meaning more photons remains to participate in image quality improvement. The effect of aluminium on the individual image quality indicators is further illustrated in Figure 46.

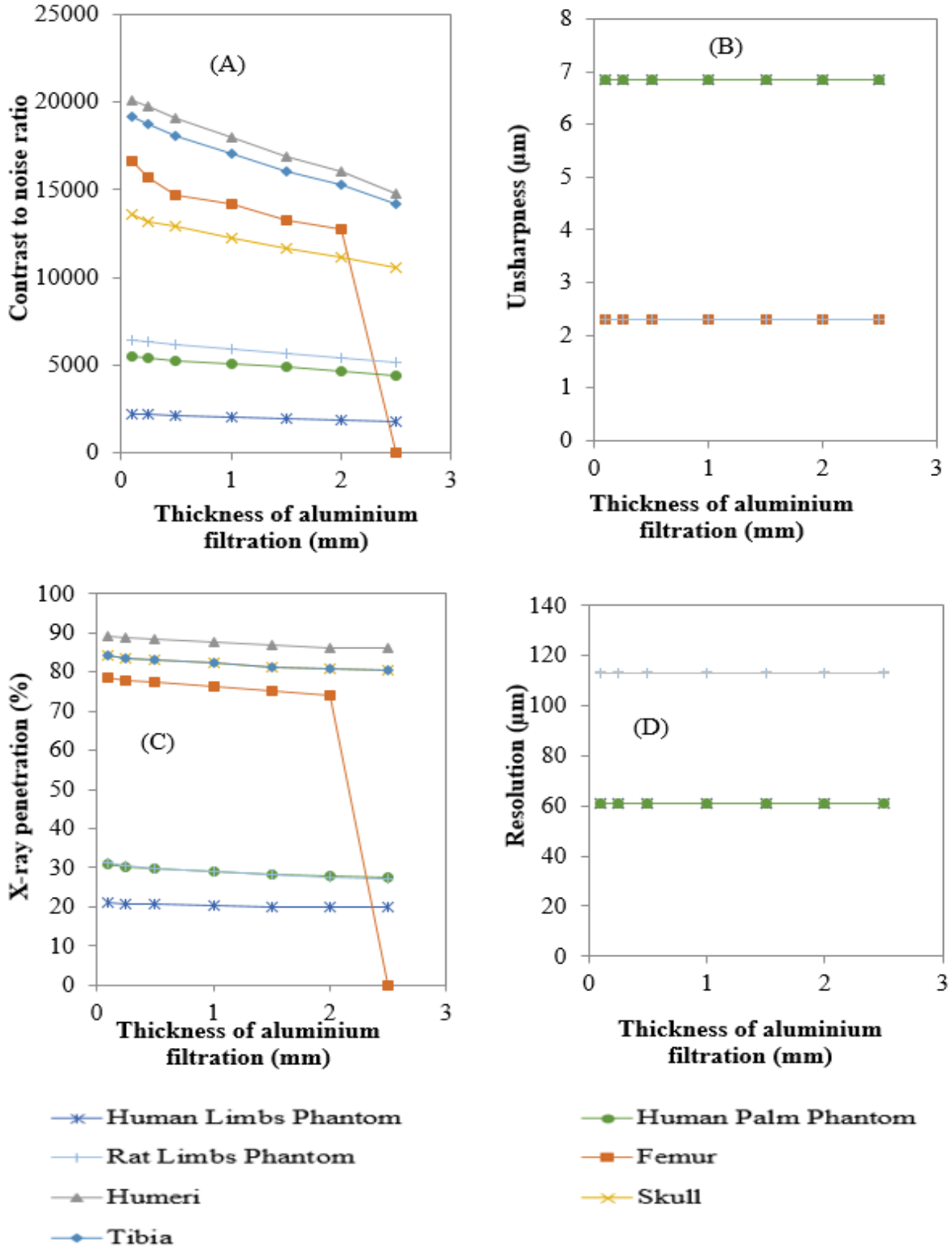

Figure 46: Illustration of the graphs of image quality indicators versus different thicknesses of aluminium X-ray filtration.

The contrast to noise ratio in Figure 46 (A) decreased as the thickness of aluminium was increased. The images of the rat samples had the highest contrast to noise ratio as compared to

the images of the phantoms throughout the varying of the thickness of aluminium filtration. Figure 46 (B) also shows that the X-ray penetration slightly decreased for both phantoms and rat samples as the aluminium thickness was increased; although the rat samples were highly penetrated by the X-ray radiation than the phantoms. At the aluminium thickness of 2.5 mm, rat femur was not penetrated by the X-ray radiation and this led to poor contrast to noise ratio of this sample at the similar aluminium thickness in Figure 46 (A). Some rat samples (tibia and skull) and phantoms resembling the human palm and rat limbs were almost equally penetrated by X-ray radiation throughout the varying of aluminium thickness in Figure 46 (C), hence the contrast to noise ratio of these subjects was slightly different in Figure 46 (A). The thickness of rat samples was smaller than the thickness of the phantoms, hence the phantoms reduced X-ray radiation more than the rat samples in Figure 46 (C) thus the image quality in terms of contrast to noise ratio was also affected similarly in Figure 46 (A).

During the image acquisition with different thicknesses of aluminium, the phantoms and rat samples were fixated at different positions. The phantoms were positioned at the FSD of 73 cm where the rat samples were at 65 cm. This led to constant and different image unsharpness and resolution between the phantoms and samples in Figure 46 (B) and Figure 46 (D). The images of the phantoms and samples had the constant image unsharpness of 2.31 µm and 6.86 µm, whereas the resolution was also constant at 113.04 µm and 60.87 µm.

The effect on aluminium X-ray filter on radiation dose is shown in Figure 47. Unlike during the experiment of varying the thicknesses of silver and copper X-ray filtration, there was a slightly decrease in the measured initial radiation dose during the varying of the thicknesses of aluminium X-ray filtration. Silver and copper X-ray filtration reduced the initial radiation dose more for both phantoms and rat samples than aluminium X-ray filtration.

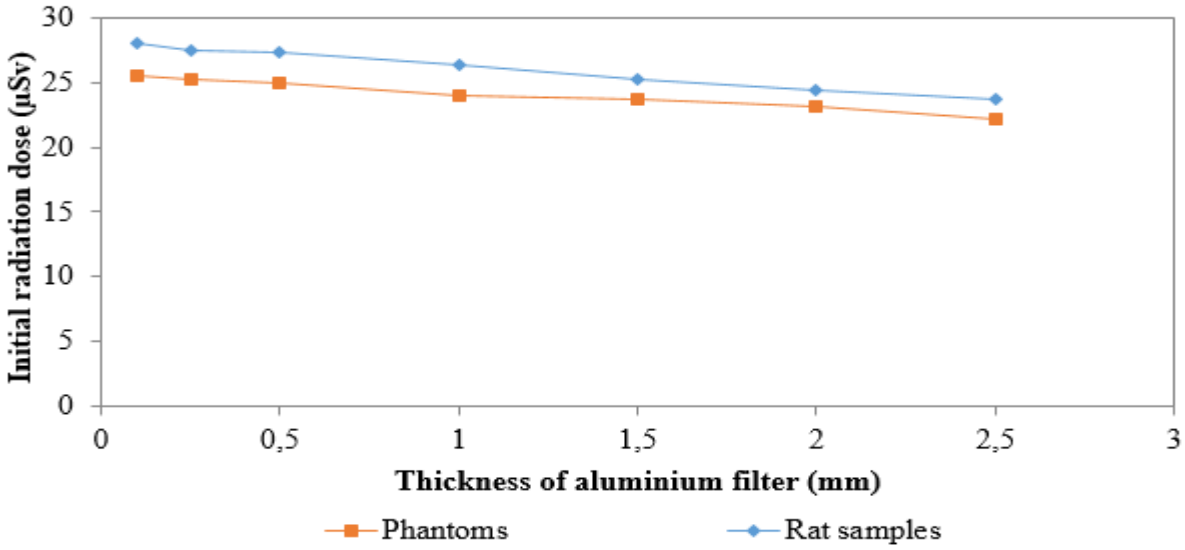

Figure 47: Initial radiation dose versus different thicknesses of aluminium X-ray filtration.

The measured initial radiation dose of the phantoms was lower than that of the rat samples as the aluminium thickness was increased in Figure 47. This distinction in initial radiation dose between phantoms and rat samples is due to the manner in which these two subjects were positioned during the experiment, the phantoms were placed further from the X-ray source than rat samples at the FSD of 73 cm and 65 cm.

Unlike during the experiment of varying the thicknesses of silver and copper X-ray filtration, the measured initial radiation dose during the varying of the thicknesses of aluminium X-ray filtration was higher. Silver and copper X-ray filtration reduced the initial radiation dose more for both phantoms and rat samples than aluminium X-ray filtration. The maximum initial radiation dose during the investigation of copper filtration was below 25 µSv in Figure 36, whereas the initial radiation dose was below 18 µSv during the silver filtration in Figure 41. Furthermore, during the aluminium investigation, the maximum initial radiation dose was above 25 µSv in Figure 45. However, similarly to both the investigation of copper and silver filtration, a clear distinction between the initial radiation dose of the phantoms and samples was observed in Figure 47. The measured initial radiation dose of the phantoms was lower than that of the rat samples as the aluminium thickness was increased in Figure 47. This distinction in initial radiation dose between phantoms and rat samples is due to the manner in which these two subjects were positioned during the experiment, the phantoms were placed further from the X-ray source than rat samples at the FSD of 73 cm and 65 cm.

The quality of the images acquired during the increase of aluminum thickness was significantly higher than those that were acquired with copper and silver thicknesses. This is due to low atomic number in aluminum (13) metal as compared to atomic numbers of copper and silver metals. Nonetheless, the quality of the images of the rat samples and phantoms was also decreasing when aluminum thickness was increasing as indicated in Figure 48. In that regard Figure 48 shows that high initial radiation dose and maximum image quality occurred at the lowest thickness of aluminum (0.1 mm) that was investigated.

Using the weight sum technique, the effects of the aluminum filter's thickness were assessed in term of image quality and radiation dose. The results are shown in Figure 48.

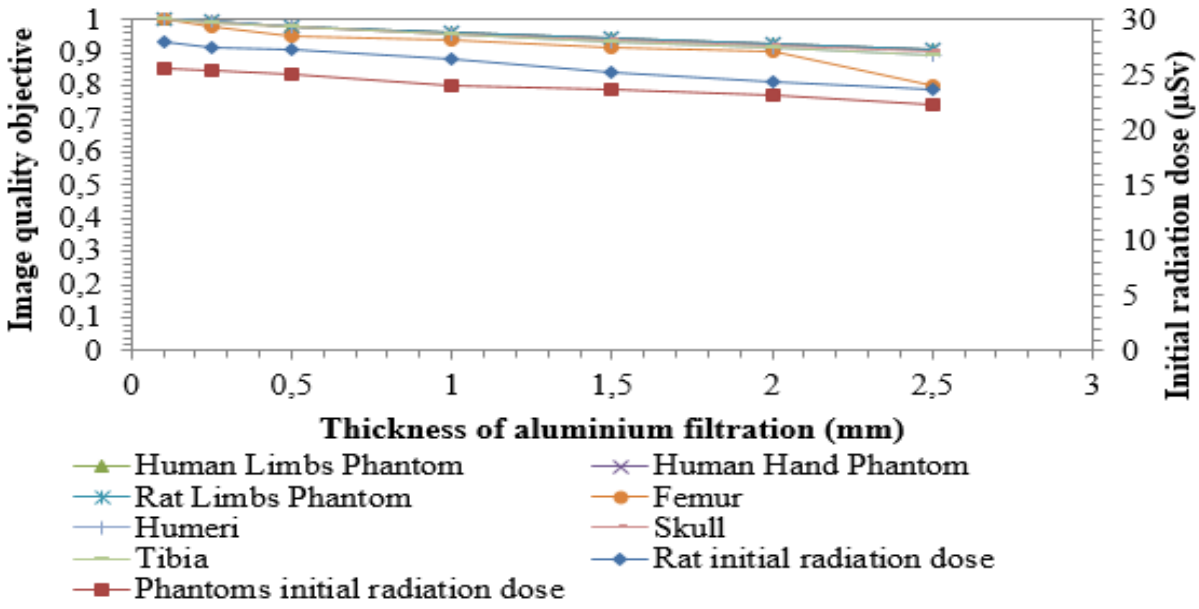

Figure 48: The image quality of the radiographs and initial radiation dose of the rat samples and phantoms versus different thicknesses of aluminium X-ray filter.

Unlike the both copper and silver filtration, Figure 48 shows that there was no significant change on image quality as the thickness of aluminium filtration was increased as observed in Figure 45. The quality of the images in Figure 45 was almost constant throughout the increase in aluminium thickness. Figure 48 also shows that the measure initial radiation dose for both samples and phantoms was lower than image quality throughout the change in aluminium thickness. The initial radiation dose of the phantoms simulating the thickness of the limbs of the rats, the limbs and the palm of the human had less initial radiation dose than the actual samples across all the aluminium thicknesses that were investigated. The initial radiation dose

decreased insignificantly when the thickness of the aluminium metal was increased from 0.1 mm to 2.5 mm in Figure 48, however high levels initial radiation dose still occurred at the highest thickness of aluminium that was investigated (2.5 mm).

Some of the radiographs that were acquired with the small thickness of aluminium (0.1 mm) that was investigated are indicated in Figure 45, are better than the quality of the images that were acquired with low thicknesses of copper (0.1 mm) and silver (0.125 mm) in Figure 36 and Figure 41. However, the challenge is that high levels of measured initial radiation dose occurred during the aluminium X-ray filter investigation as compared to other X-ray filters. Even though the image quality of rat femur was slightly different at the initial radiation dose of 22 µSv (0.028 mSv) as indicated in Figure 48, the quality of the radiographs of other rat samples and phantoms was maximum between the initial radiation dose of 23 µSv (0.023 mSv) and 28 µSv (0.028 mSv). The image quality was maximal throughout this specified initial radiation dose, (23 µSv (0.023 mSv) and 28 µSv (0.028 mSv). The samples were positioned at the FSD of 65 cm whereas the phantoms were at 73 cm during the investigation, this difference in FSD is responsible for the variation in the measured initial radiation dose for the samples and phantoms. The graphs in Figure 49 confirms that the image quality objective and the radiation dose do not change significantly with the increase of the thickness of aluminium filtration.

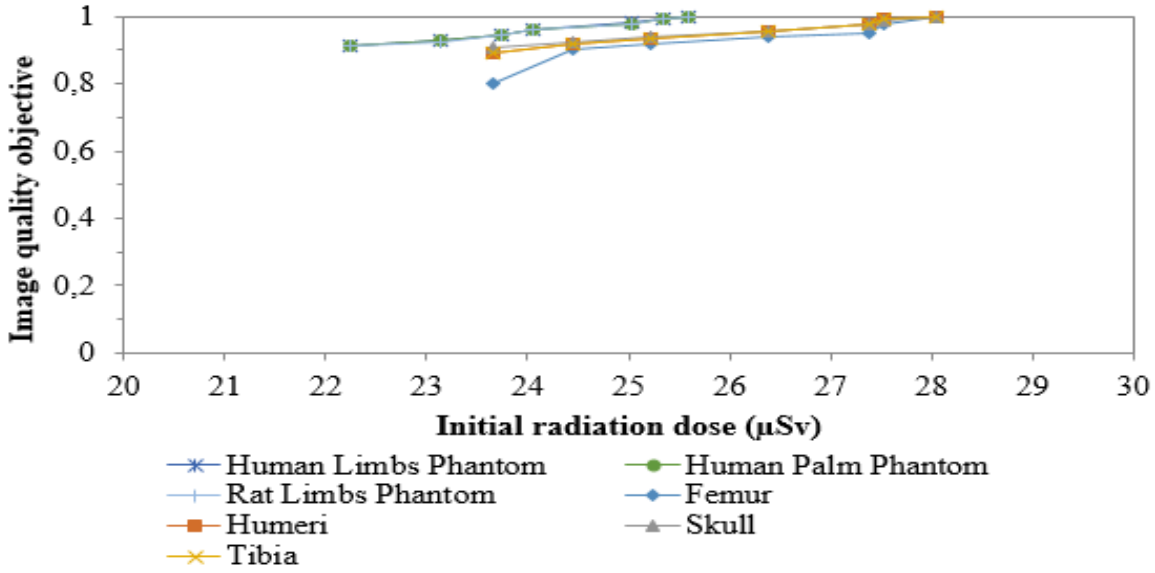

Figure 49: The image quality of the radiographs of rat samples and phantoms versus initial radiation dose for investigation of different thicknesses of aluminium metal X-ray filter.

The fact that images had maximum quality with high initial radiation dose at the aluminium thickness of 2.5 mm in Figure 48 and Figure 49, sustains the recommendations of the European commission that aluminium thickness greater than 2.5 mm must be used especially when acquiring the radiographs of the human limbs. Further investigation of aluminium thickness can still be achieved above the thickness of 2.5 mm, initial radiation dose will be reduced further because the thickness of the metal will be increased and thus more energy of the photons will be absorbed. In that regard, the findings of this study suggests that 2.5 mm thickness of aluminium filter should be used to optimize the images of the human limbs, provided the X-ray tube voltage and current are kept constant at 100 kV and 100 µA, X-ray exposure time at 1 second and the FSD of 65 cm.

4.3.4. Optimization of the thickness of tin X-ray filter

In this study, the images that were acquired during the varying of the thicknesses of the tin X-ray filter are indicated in Figure 50. The thickness of the tin metal was varied between 0.125mm to 1.000 mm.

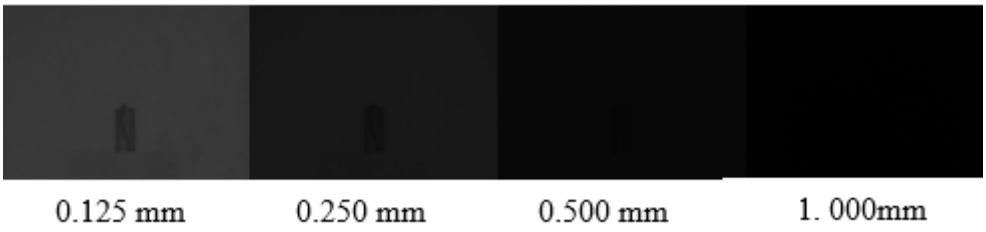

Figure 50: Typical radiographs that were acquired within the tin filter thickness range of 0.1 mm – 2.50 mm, X-ray current of 100 µA, X-ray tube voltage of 100 kV, FSD of 65 cm and X-ray exposure time of 1 sec.

The images were dark at bigger thicknesses of tin metal. Compared to other X-ray filters, all the images that were acquired during the investigation of tin metal are of poor quality. The effect of tin metal filter on the individual image quality indictors are shown in Figure 51. Similar to Figure 37, 42 and 46, Figure 51 (C) also shows that the X-ray penetration of rat samples and phantoms decreased quadratically as the thickness of X-ray filtration was increased. Figure 51 (C) also shows that the X-ray penetration of the rat samples was higher than that of the phantoms as the thickness of tin X-ray filtration was increased. The contrast to noise ratio of both the phantoms and rat samples in Figure 51 (A) followed the same trend but

with an exponential curve. The images of both the rat samples and phantoms were very poor at 1.00 mm thickness of tin metal because they had zero contrast to noise ratio at this thickness.

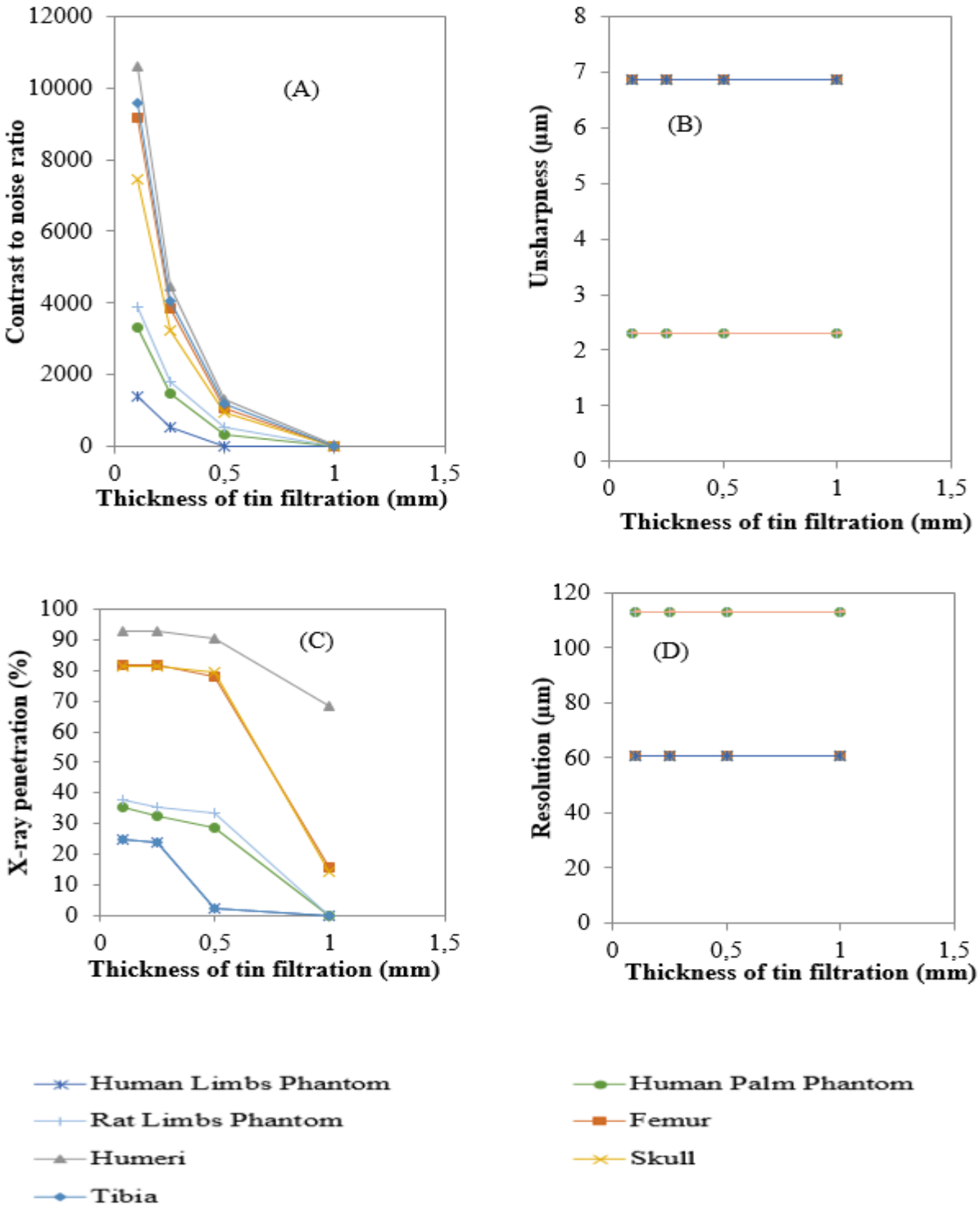

Figure 51: Illustration of the graphs of image quality indicators versus different thicknesses of tin X-ray filtration.

The FSD is responsible for the difference image unsharpness and resolution of rat samples and phantoms in Figure 51 (B) and Figure 51 (D). The FSD of the phantoms and rat samples was 73 cm and 65 cm. These two image quality indicators were constantly different throughout the image acquisition with the varying of tin metal thickness, the image unsharpness was constant at 2.31 µm and 6.86 µm and the resolution was also constant at 113.04 µm and 60.87 µm for both the phantoms and rat samples

Figure 52 indicate the effects of varying of tin metal thickness on the initial radiation dose for both the rat samples and phantoms. Unlike other X-ray filter that were investigated in this study, the maximum measured initial radiation dose during the tin filter investigation was below 14 µSv in Figure 52.

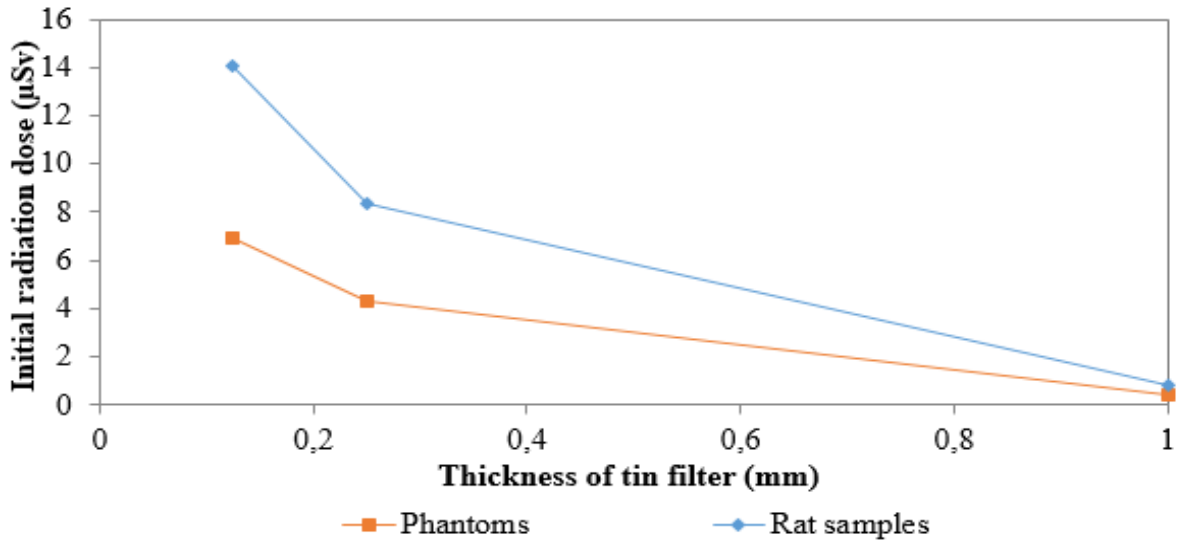

Figure 52: Initial radiation dose versus different thicknesses of tin X-ray filtration.

Figure 52 also shows that the initial radiation dose for the phantoms was very minimal during the varying of tin filter, this initial radiation dose was below 10 µSv. The difference in the measured initial radiation dose for both the phantoms and the rat samples is mainly due to the way in which these subjects were positioned during the image acquisition. The phantoms were a bit further from the X-ray source at the FSD of 73 cm, whereas the rat samples were placed at 65 cm.

Tin and silver metals have the atomic numbers of 50.00 and 49.00 hence they reduced initial radiation dose more than other metal filters. The maximum initial radiation dose that was obtained with the tin and silver filters is 14.00 µSv and 18.00 µSv, whereas the maximum

initial radiation dose that was obtained with the coper and aluminium filters is 24.53 µSv and 28.06 µSv µSv. The atomic number of coper and aluminium metals is 29 and 13 respectively.

The tin metal with atomic number 50 had low image quality radiographs than other X-ray filters that were investigated in this study. When the weight sum technique is uside, Figure 53 showed that the image quality of the rat's bones and phantoms decreased as the thickness of tin metal was increased, thus images of better quality occurred at 0.1 mm thickness of tin metal.

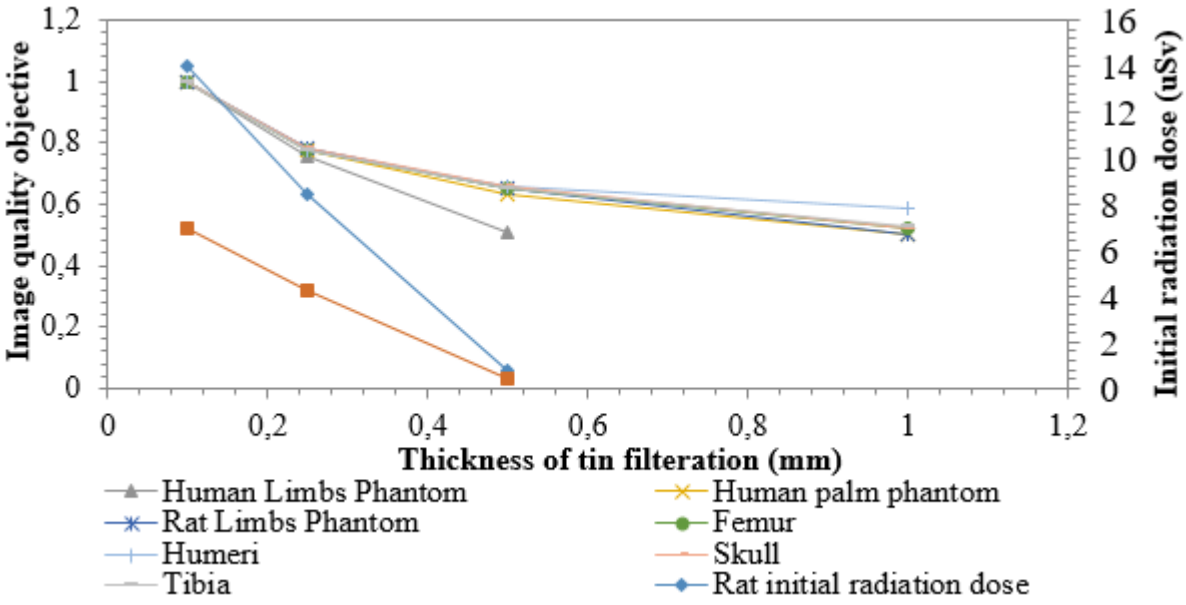

Figure 53: The image quality of the radiographs of the rat samples and phantoms versus different thicknesses of tin metal X-ray filter.

The quality of the images was better at low thickness of tin metal, whereas the quality of images was very poor at the highest thickness of tin metal as shown in Figure 50. The radiograph of the human limbs phantoms was not formed at the 0.1 mm thickness; furthermore, this sample had the least image quality at 0.5 mm thickness as indicated in Figure 53.

The decrease in initial radiation dose for both the samples and phantoms as the tin metal thickness was increased was also observed in Figure 54. The overall initial radiation dose occurred during the tin metal thickness investigation is less than the initial radiation dose that occurred during the investigation of other metal thicknesses. However, the trend observed in

Figure 54 was also observed with other X-ray filters. The highest initial radiation dose was encountered at the lowest thickness of tin metal (1 mm) that was investigated.

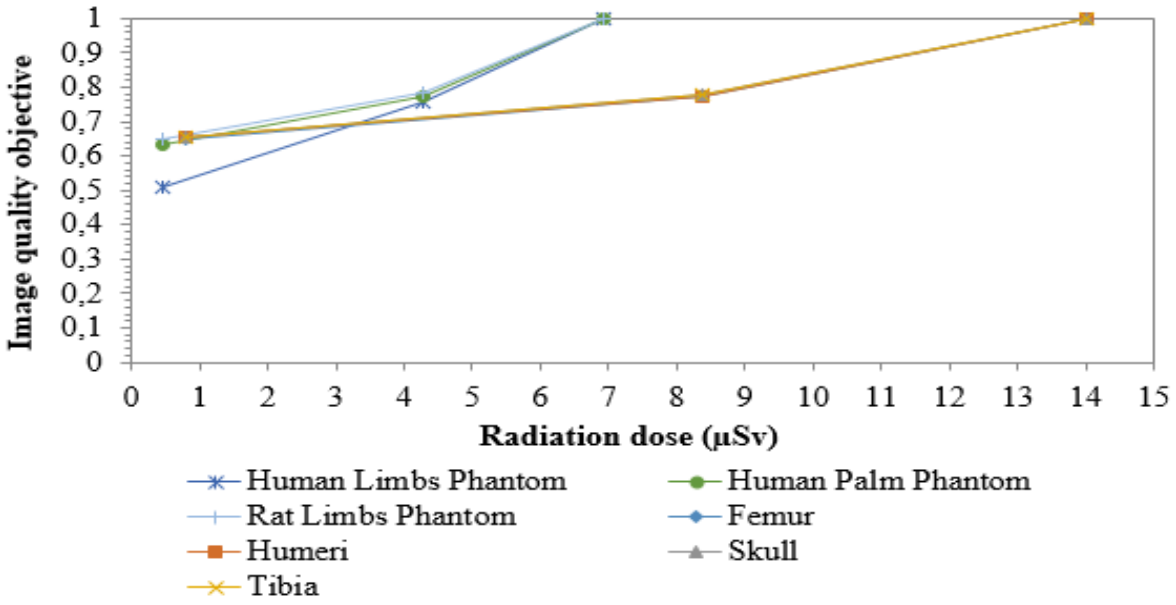

Figure 54: The image quality of the radiographs of the rat samples and phantoms versus initial radiation dose for different thicknesses of tin X-ray filter.

Figure 54 shows that the image quality of all rat bones and phantoms was better at the initial radiation dose of 6 µSv (0.006 mSv) and 14 µSv (0.014 mSv). This initial radiation dose resulted in low image quality although it is within the radiation reference level suggested by American college of radiology., (2010) for X-ray examinations of the human limbs. Figure 54 shows that the measured initial radiation dose was less for the phantoms than for the actual rat samples as the image quality was increased. The acquisition of radiographs using the X-ray filter thickness of tin metal (0.1 mm - 1 mm) results in poor image quality as compared to other X-ray filters that were investigated in this study. The tin metal thickness less than 0.1 mm could result in optimized quality images and minimized initial radiation dose, because this metal has high atomic number which makes it efficient to absorb more X-ray photons even at lower thicknesses. In that regard, the combination of less than 0.1 mm thickness tin metal thickness with X-ray tube voltage of 100 kV, X-ray tube current of 100 µA, X-ray exposure time of 1 second and the FSD of 65 cm, is recommended for optimization of radiographs and initial radiation dose in X-ray radiography.

Chapter 5: Conclusion and recommendations

The optimization of bone X-ray radiography was achieved through the establishment of the relationship between X-ray scanning parameters on image quality indicators and initial radiation dose. Increasing the X-ray tube parameters (voltage, current and exposure time) maximized X-ray penetration and contrast to noise ratio. Image unsharpness and resolution were constant for each subject throughout the varying of X-ray tube parameters, however these two image quality indicators were changed during the varying of FSD. This phenomenon indicated that the reduction of image unsharpness can be achieved by increasing FSD and resolution was also maximized in this regard. However, a balance is required between the unsharpness and resolution, because high values of these two image quality indicators signifies poor image quality where small details of the projected information becomes obscure. X-ray penetration and contrast to noise ratio were also affected by varying of the FSD, a slight decrease in these two image quality indicators was observed when the distance between the X-ray source and the subject was increased. The measured initial radiation dose was also affected by changing the X-ray tube parameters and FSD. Increasing the X-ray tube parameters increased the measured initial radiation dose of the subjects, the subject that was positioned closer to the X-ray source had high levels of the initial radiation dose than the one that was positioned further from the source. The measured initial radiation dose decreased as the FSD was increased.

After the application of weight sum technique, the best compromise between maximum image quality and minimized initial radiation dose was found and the corresponding X-ray scanning parameters were selected for optimization of bone X-ray radiography. The selected X-ray scanning parameters were established through the investigations of the effect of X-ray tube voltage, X-ray current, X-ray exposure time and FSD. The increase of the X-ray tube parameters increases both the image quality objective and the initial radiation dose. The slight increase in image quality objective can be achieved by the increase in the FSD while considering the rapid accumulation of initial radiation dose. The X-ray scanning parameters such as the X-ray tube voltage of 100 kV, X-ray tube current of 100 µA, X-ray exposure time of 2.83 sec and the FSD of 73 cm were selected for optimization of X-ray radiography through reduction of initial radiation dose. The initial radiation dose produced with these parameters

was less than 1.00 mSv, this initial radiation dose is within the acceptable diagnostic reference dose and radiation dose levels as suggested by Dianna., (2018), American college of radiology practice., (2010) and Brennan & Seeram. (2006).

The increase of the thicknesses of X-ray filters of different atomic numbers causes a decline in both the bone image quality and initial radiation dose during the investigation of the effect of X-ray filters. High atomic number X-ray filters are good absorbers of a large quantity of X-ray photons even at low thicknesses, thus providing the possibility of further improvement and optimization of image quality with low initial radiation dose even at low thicknesses. In this study, high atomic number X-ray filters that were investigated, tin (Z: 50) and silver (Z: 47), reduced initial radiation dose efficiently but the corresponding image quality was very poor throughout all their thicknesses. The small thicknesses of tin and silver that are smaller than those that were investigated in this study, are recommended for optimization in X-ray radiograph while other X-ray scanning parameters are kept constant at the X-ray tube voltage of 100 kV, X-ray tube current of 100 µA, X-ray exposure time of 1 sec and FSD of 65 cm.

Aluminium and copper X-ray filters are commonly used for X-ray filtration in diagnostic radiology (Bushberg, et al., 2002). In this study, copper X-ray filter yielded the significant decrease of the measured initial radiation dose as compared to aluminium X-ray filter. Copper X-ray filtration would be preferred for optimization over aluminium because at equal thicknesses (0.1 mm - 2.5 mm), aluminium would always yield insignificant reduction of initial radiation dose due to the inability of this metal to absorb high quantity of low energy X-ray photons. These low energy X-ray photons play a major contribution in the accumulation of initial radiation dose than in image quality improvement. The inability of aluminium (Z: 13) to absorb an adequate quantity of low energy X-ray photons is due to low atomic number as compared to copper metal (Z: 29). In this study, the X-ray settings that constituted the parameters of 0.1 mm thickness of copper, X-ray tube voltage of 100 kV, X-ray tube current of 100 µA, X-ray exposure time of 1 second and the FSD of 65 cm yielded the most significant reduction of initial radiation dose with the adequate image quality. Therefore, it can be concluded that optimization of image quality and minimization of initial radiation dose in bone X-ray radiography can be achieved successfully and efficiently with the combination of these X-ray scanning parameters.

References

Abimbola, J. M., 2013. A nonlinear weights selection in weighted sum for convex multiobjective optimization, Ile-Ife, Nigeria: ajubril@oauife.edu.ng.

Akmal, S. & ZhonghµA, S., 2013. Radiation dose measurements in coronary CT angiography. World J Cardiol, 5(12), pp. 459-464.

Andiscoa, D., Blancob, S. & Buzzia, A., 2014. Dosimetry in radiology. Radioprotection / Update in radiology, pp. 1-4.

Bacher, K., 2006. Evaluation of image quality and patient radiation dose in radiology, Ghent, Belgium: University of Medicine and Health Sciences Universitiet Gent.

Begum, Z., 2001. Entrance surface dose measurement for some of the radiological patients in Bangladesh. Málaga, IAEA in Austria, pp. 9-12.

Blancob, S. Andiscoa, D., & Buzzia, A. E., 2014. Dosimetry in radiology. Rev. Argent. Radiol, 78(2), pp. 114-117.

Bushberg, J. T., Anthony Seibert, J., Edwin Leidhold, M. J. & Boone, J. M., 2002. Radiation detection and measurements. In: R. Joyce, ed. The essential physics of medical imaging. 2nd ed. Phidelphia: Lippincott Williams & Wilkins, pp. 628-668.

Carl A. C., & Gudrun Alm, C., 1996. Basic physics of X-ray imaging, Sweden: Faculty of Health Sciences Linköping University.

Chougule, A., 2005. Reference Doses in Radiological Imag. 11(2), pp. 1425-4689.

CIRS, 2017. ATOM Dosimetry Verification Phantoms model 701-706, Norfolk: Computerized Imaging Reference Systems, Inc.

Dianna, C., Jordan, D. W., Murray Becker, M. & Brady, S., 2018. Radiation Dose Assessment Introduction: ACR Appropriateness Criteria

Dance, D. R., Evans, S. H., Skinner, C. L. & Bradley, A. G., 2012. Diagnostic Radiology with X-Rays. In: M. A. Flower, ed. Webb's Physics of Medical Imaging. 2nd ed. Boca Raton: Taylor & Francis Group, pp. 14-91.

David, E. H., William, E. M. & Winslow, J., 2009. Physical phantoms for experimental radiation dosimetry. In: X. Xie George & E. Keith F, eds. Handbook of Anatomical Models for Radiation Dosimetry. 1st ed. London: CRC Press Taylor and Francis group, pp. 389-407.

Dendy, P. & Heaton, B., 1999. Physics for Diagnostic Radiology. 2 ed. Phidelphia, PA: Institute of Physics Publishing.

Denis, G. & Pelli, B., 2013. Measuring contrast sensitivity. Vision Research, 90(15), pp. 10-14.

Desouky, O., Ding, N. & Zhou, G., 2015. Targeted and non-targeted effects of ionizing. Journal of Radiation Research and Applied, 8(2), pp. 247-254.

Dlamini, T., 2014. Radionuclides and toxic elements transfer from the Princes dump to the surrounding vegetation in Roodepoort South Africa: Potential radiological and toxicological impact on humans. 1 ed. Mafikeng: North West University

Dumela, K. E., 2010. Optimizing patient protection during diagnostic procedures - developing diagnostic reference levels at the Dr George Mukhari Hospital, Polokwane, SA: Faculty of medicine.

Ervin, B. & Podgorsak, E., 2005. External Photon Beams: Physical Aspects. In: Radiation Oncology Physics: A Handbook for Teachers and Students. Vienna, Australia: International Atomic Energy Agency, pp. 3-162.

Faiz, M. K., 2003. Measurement of absorbed dose. In: J. Pine, M. Standen & L. R. Kairis, eds. The physics of radiation therapy. 3rd edition ed. Minneapolis, Minnesota: Lippincott Williams & Wilkins, pp. 106-154.

Farah, A., 2016. Weighted Scalarization versus Compromise Solution in Multi-Objective Economic Dispatch for Microgrids, Montreal: McGill University.

Garret, N., 2007. Multidiscipline Design and Optimization, Colorado Springs, CO: John Wiley & Sons, Ltd.

Garrett, W. R., Splettstosser, H. R. & Titus, D. E., 1980. Radiography in Morden Industry. Rochester, New York: Eastman Kodak Company.

Gupta, A. K., Veena, C. & Niranjan, K., 2013. Diagnostic Radiology: Recent Advances and Applied Physics in Imaging. 2nd ed. New Delhi: Jaypee Brother Medical Publishers.

Harbison, S. & Martin, A., 2006. An Introduction to Radiation Protection, London: Hodder.

Hendee, W. R. & Ritenour, E. R., 2002. Analytical description of image quality. In: B. Hillary, ed. Medical imaging physics. 4th Edition ed. New York: Wiley-Liss, Inc, pp. 281-287.

Hess, R. & Neitzel, U., 2012. Optimizing image quality and dose for digital radiography of distal pediatric extremities using the contrast-to-noise ratio. Fortschr Röntgenstr, 184(2012), pp. 643–649.

Hirotaka, N., 2005. Multi-objective optimization and its engineering applications, Konan: Konan University.

Hoffman, J. W., 2012. Characteristics of the Micro-Focus X-ray Tomography Facility (MIXRAD) at Necsa in South Africa. Durban, South African Nuclear Energy Corporation (Necsa), pp. 1-12.

ICRP, 2007. The 2007 Recommendations of the International Commission of Radiological Protection. Annals of ICRP Publication, 103(12), pp. 1-35.

ICX Technologies, 2003. Unique hand-held radionuclide, Virginia: Available online radiation.icxt.com.

Institute of Physics and Engineering in Medicine, 2002. A good practice guide on all aspects of ionizing radiation protection in the clinical environment, New York, UK: IPEM Publications Committee.

ICRP, 93. 2001. Managing patient dose in digital radiology, Netherlands: Elsevier.

Jacob, W. & Blume, C., 2014. Pareto Optimization or Cascaded Weighted Sum: A Comparison of Concepts. Algorithms, 7(1), pp. 50-65.

Kristopher, S., 2013. Learn ImageJ, Los Angeles: Bryan W. Jones.

Ladia, A. P., Skiadopoulos, S. G., Kalogeropoulou, C. P., Zampakis, P. E & Dimitriou, G. G. & Panayiotakis, G. S., 2016. Radiation Dose and Image Quality Evaluation in Paediatric Radiography. International Journal of New Technology and Research (IJNTR), 2(3), pp.09-14.

Leea, S. C., Wanga, J., Liuc, S. C. & Jiang, S. H., 2007. Evaluation of dose–image-quality optimization in digital chest radiography. Nuclear Instruments and Methods in Physics Research, Volume 580, pp. 544–547.

Martin, C., 2002. Interactions of ionising radiations with matter. In: D. Sutton, ed. Practical Radiation Protection in Health Care. Oxford, UK: Oxford University Press, pp. 13-26.

Mayles, P., Nahum, A. & Rosenwald, J. C., 2007. Handbook of radiotheraphy physics-theory and practice. Revised ed. New York: Taylor & Francis Group, LLC.

McGraw-Hill Concise Encyclopedia of Physics, 2000. Parallel-plate ionization chamber, Columbia: The McGraw-Hill Companies, Inc.

Michael, Y. M., Thomas, P. L. & David, O. J., 2004. Basic radiology. North Carolina, Raleigh: The McGraw-Hill.

Nyathi, T., 2012. Dose Optimization in Diagnostic Radiology, Johannesburg: University of the Witwatersrand.

Olubamiji, A., 2011. The influence of filtration, tube current and number of projections on CBCT image quality, Finland: Medical Imaging Centre.

Osborne, Dustin R., Yan, Shikui., Stuckey, Alan., Pryer, Lindy., Richey, Tina & Wall, Jonathan S.,2012. Characterization of X-ray Dose in Murine Animals Using microCT, a New Low-Dose Detector and Nano Dot Dosimeters. Plosone, 7(11), pp. 1-9.

Pacella, D., 2015. Energy-resolved X-ray detectors: the future of diagnostic imaging. Reports in Medical Imaging, 8(10), pp. 1-13 available online https://doi.org/10.2147/RMI.S50045.

Palomo, J., Rao, P. & Hans, M., 2008. Influence of CBCT exposure conditions on radiation dose. Oral Surg Oral Med Oral Pathol Oral Radiol Endod, 105(6), pp. 773-78.

Parkinson, A. R., Balling, R. J. & Hedengren, J. D., 2013. Optimization methods for engineering design, Provo, Utah: Addison-Wesley Publishing Company.

Paulo, R. C., 2014. Computer tomography phantom applications. In: A. Larry & M. K. DeWerd, eds. The Phantoms of Medical and Health Physics: Devices for Research and Development. 1st ed. Madison: Springer Science & Business Media, pp. 123-137.

Radiology Key, 2016. The X-ray Beam. General radiology, 1(5), pp. 2 available online https://radiologykey.com/the-x-ray-beam/.

Milch, 2008. Coolidge side-window tube (scheme), Augsburg: Roentgen-Roehre.svg available online at http://de.wikipedia.org/w/index.php?title=Datei:RoentgenRoehre.svg.

RSNA, 2010. X-ray radiography, Bone, Jorie Boulevard, Oak Brook: Radiological Society of North America (RSNA).

RSNA, 2018. Radiationinfor.org, North America: Radiological Society of North America, Inc. available online at https://www.radiologyinfo.org/en/info.cfm?pg=safety-hiw_09.

Ruiz, F., Ruiz-Cruces, R., Pearez-Martianez, M., Loa pez, J., Tort Ausina, I & Diaez De Los Riaos, A.,2000. Patient dose from barium procedures. The British Journal of Radiology, 73(871), pp. 752-761.

Seakamela, T., 2016. A Study of Cracks using Micro-Focus X-ray Computed Tomography and Fractal Geometry., Johannesburg: Faculty of Science.

Shrimpton, P., Wall, B. & Fisher, E., 1981. The tissue equivalence of Alderson Rando anthropomosphic phantom for X-rays of diagnostic qualities. Phys Med Biol, 1(26), pp. 9-133.

Sprawls, P., 1985. The Physical Principles of Medical Imagings. 2nd Edition ed. Madison, Wisconsin: Medical Physics Publishing available online at http://www.sprawls.org/resource.

Sprawls, P., 1994. The Physical Principles of Medical Imaging. Atlanta, GA, USA: A Wiley Company.

Thermo Fisher Scientific, 2008. Radiation Detection & Measurement, Massachusetts: available online at www.thermo.com/rmp.

Timothy Marler, R. & Jasbir Arora, S., 2009. The weighted sum method for multi-objective optimization: new insights. Struct Multidisc Optim 41(6) pp.853-862.

Tootell, A., Szczepura, K. & Hogg, P., 2014. An overview of measuring and modelling and modelling dose and risk from ionising radiation for medical exposures. Radiography, 20(4), pp. 323-332.

Uffmann, M. & Schaefer-Prokop, C., 2009. Digital radiography: The balance between image quality and required. European Journal of Radiology, Volume 72, pp. 202-208.

Ullman, G., 1977. Quantifying Image quality in diagnostic radiology using simulation of the imaging system and model observers. Linköping University Medical Dissertations No. 1050, pp. 1-85.

Umadevi, N. & Geethalakshmi, S., 2011. A brief study on human bone anatomy and bone. IJCES International Journal of Computer Engineering Science, pp. 93-104.

Unruh, J., 2015. Stowers Institute ImageJ Plugins Page, Kansas City: Stowers Institute for Medical Research.

Vano, E., Fernandez, J.M., Ten, J. I.; Gulbelalde, E., Gonzalez, L & Pedrosa, C.S.A.,2002. Real-time Measurement and Audit of Patient Undergoing Computed Radiography. Radiology, 225(1), pp. 283-285.

Weck, O. & Kim, I. Y., 2004. Adaptive Weighted Sum Method for Bi-objective Optimization, California: Massachusetts Institute of Technology.

Whaites, E., 2002. The biological effects and risks associated with X-rays. In: Essentials of dental radiography and radiobiology. 3rd ed. London, UK: Churchill Livingstone, pp. 29-32.

Whaites, E. & Cawson, R. A., 2002. Essentials of Dental Radiography and Radiology. 3rd ed. London: Churchill Livingstone.

William, R. H. & Ritenour, E. R., 2002. Experimental radiobiology. In: Medical Imaging Physics. 4 ed. New York: Wiley-Liss, pp. 403-411.